

Search for Weak Scale Supersymmetric Particles in Compressed Scenarios

©2023

Justin Anguiano

B.S. Engineering Physics, University of Kansas, 2015

M.S. Computational Physics and Astronomy, University of Kansas, 2017

Submitted to the graduate degree program in the Department of Physics and Astronomy
and the Graduate Faculty of the University of Kansas in partial fulfillment of the
requirements for the degree of Doctor of Philosophy.

Graham Wilson, Chairperson

Alice Bean

Committee members

Christopher Rogan

Ian Lewis

Zsolt Talata, External Reviewer

Date defended: May 04, 2023

The Dissertation Committee for Justin Anguiano certifies
that this is the approved version of the following dissertation :

Search for Weak Scale Supersymmetric Particles in Compressed Scenarios

Graham Wilson, Chairperson

Date approved: _____ May 12, 2023 _____

Abstract

A generic search for supersymmetric particles with an emphasis on compressed scenarios is performed with $\sqrt{s} = 13$ TeV proton-proton collisions at the CMS detector using a data sample with integrated luminosity of 138 fb^{-1} . Potential supersymmetric events with initial-state-radiation recoiling against a massive invisible sparticle system are organized using the Recursive Jigsaw Reconstruction method. Events are further categorized by physics object counts such as jet multiplicity, lepton multiplicity, b-tags, and kinematic variables that are sensitive to generic compressed sparticle topologies. This work focuses on the following pieces of a larger analysis: the selection of leptons, their efficiency measurement and calibration, and the implementation and optimization of the data-driven fit. Finally, expected limits with a 95% C.L. are placed on processes that include the production of electroweakinos, sleptons, and stops.

Acknowledgements

First I would like to acknowledge the collaborative effort and work done by my research group. This work would not be possible without the extensive work of my advisors and peers which has been included alongside my own for completeness. Much of the content is based on, or modeled after, our internal Analysis Note [1], so thanks to everyone that has contributed to this massive analysis. I am also extremely grateful to my supervisor, Professor Graham Wilson, for his invaluable mentorship and patience that has pushed me to be the best version of myself. I'm also grateful for everyone in my research group and their excellent advice and support, with a special thanks to the students who are always happy to team up and solve problems. I would be much worse off without the community we've developed. Finally, I would like to express my gratitude to my parents which have been essential in helping me survive the final stretch of grad school.

Contents

1	The Standard Model and Supersymmetry	1
1.1	Introduction	1
1.2	The Standard Model	2
1.3	Supersymmetry	3
2	Motivating the Search for SUSY	11
2.1	Introduction	11
2.2	Stabilizing the Higgs mass	12
2.3	The Muon Anomalous Magnetic Moment	13
2.4	The W boson mass	15
2.5	The current status of SUSY	16
3	The CMS experiment	24
3.1	Introduction	24
3.2	The Large Hadron Collider	24
3.3	The CMS Detector	25
4	Compressed SUSY Search	29
4.1	Data and Simulation	29
4.2	Compressed Signal Overview	31
4.3	RJR Methodology	33
4.4	Compressed Kinematics	36
5	Analysis Description	41

5.1	Introduction and Strategy	41
5.2	Event Selection and Physics Objects	41
5.3	Categorization	44
6	Lepton Selection and Efficiency Measurement	51
6.1	Lepton Object Definitions	51
6.2	Tag-and-Probe Methodology	55
6.3	The Electron Tag-and-Probe	57
6.4	The Muon Tag-and-Probe	62
6.5	Lepton Systematics and Scale Factors	69
7	Data Driven Fit and Fit Evaluation	72
7.1	Introduction	72
7.2	Fit Strategy and Fit Region Definitions	72
7.3	Fit Implementation and Model Definition	73
7.4	Definitions of Modeling Systematics	77
7.5	Development of Modeling Systematics	81
7.6	Control Region and Validation Region Fit Results	86
7.7	Bias tests	86
8	Results	94
8.1	Asymptotic Limits	94
8.2	Model Dependent Interpretation	97
9	Summary	101

List of Figures

1.1	The elementary particles of the standard model which includes the color coded categories of fermions and bosons as well as their nominal mass (or mass upper limit), charge, and spin [2].	4
1.2	The elementary particles of the standard model with their supersymmetric partners.	5
1.3	Left: Wino-like LSP from PMSSM model point 18898934. Right: Higgsino-like LSP from PMSSM model 6755879 [3]. Both models have a somewhat similar relative mass structure but order of magnitude differences in the Higgs, squark, and slepton sectors.	7
1.4	Comparison of the Wino LSP and Higgsino LSP models from Figure 1.3 sparticle pair production cross sections.	8
1.5	Example average neutralino branching fractions for the combined set of pMSSM model points from [3] for $\Delta m < 50$ GeV. The LSP content for each figure is Wino-like top-left, Bino-like top-right, and Higgsino-like bottom. Branching fractions are shown as a function of the mass splitting $\Delta m = m_{\tilde{\chi}_2^0} - m_{\tilde{\chi}_1^0}$. The model with Wino LSP is subject to a W channel enhancement while Z is suppressed. In the Bino case the W channel is suppressed and the Z is enhanced. The Higgsino LSP models can be dominated by either the W or Z channel depending on the mass splitting.	9
1.6	Example reweighting of simplified model from an ATLAS search which covers the different dilepton mass line shapes in the same-sign and opposite-sign eigenstate cases [4].	10

2.1	Diagrams which contribute to $(g - 2)_\mu$. Left is the single photon Schwinger loop that contributes the largest deviation from two. The middle diagrams are electroweak contributions and the far right diagram is the hadronic vacuum polarization the involves a loop with hadrons [5].	14
2.2	Example muon diagrams which include sparticle loops that would contribute to $(g - 2)_\mu$ [6]	15
2.3	The mass of the W boson as a function of top quark mass which displays the CDF II measurement with 68% C.I. compared to the SM prediction and LEP2/Tevatron measurement with 68% C.I [7].	17
2.4	Illustration of various color coded model points which correspond to different scenarios and electroweakino model types that favor the measured $(g - 2)_\mu$ and W mass that exceeds the SM prediction. The grey band represents the SM prediction, the green line combines all the experimental results for the W mass, and the blue line indicates the combined $(g - 2)_\mu$ experimental results [8].	18
2.5	The CMS (left) and ATLAS (right) gluino limits from multiple competing channels and models [9][10].	18
2.6	The CMS (left) and ATLAS (right) squark limits from multiple competing channels and models [9][10].	19
2.7	The CMS (top) and ATLAS (bottom) limits on stop production [9][10]. . . .	20
2.8	The mass limits on chargino pair production with degenerate masses $m_{\tilde{\chi}_2^0} = m_{\tilde{\chi}_1^\pm}$ for CMS (top) and ATLAS (bottom). There are no published limits on compressed chargino pairs in CMS [9][10].	22
2.9	The slepton mass limits for CMS (top) and ATLAS (bottom) which assume the same masses for L and R sleptons and combine smuon and selectron production [9][10].	23

3.1	Layout of the LHC with the red clockwise beam and blue counter clockwise beam. The beams collide at the interaction regions of the four experiments: CMS, ATLAS, ALICE, and LHCb. [11]	25
3.2	Cross-sectional view of the CMS detector and main detector components [12]	26
3.3	A Transverse slice of the CMS detector that illustrates the components that specialize in detecting specific particles [13].	28
4.1	Mass grids and associated numbers of events per grid point for each the SUSY processes T2tt, T2bW, TChiWZ, TChipmWW, and TSlepSlep [1].	30
4.2	Feynman diagrams for SUSY pair produced processes. Top row involves stop pairs where the intermediate state on the top left (T2tt) undergoes stop to top decay and the top right (T2bW) instead undergoes a stop to chargino decay. The middle left diagram (TChipmWW) shows chargino pairs decaying to two W boson and the middle right (TChiWZ) is a neutralino and chargino pair which decay into a W and Z boson final state. The bottom diagram (TSlepSlep) shows di-slepton production with sleptons decaying directly to SM leptons.	32
4.3	Illustration of a visible ISR system recoiling against a sparticle system (S) which can be decomposed into soft visible subsystem (V) and massive invisible subsystem (I) [1].	33
4.4	A depiction of the three reference frames used in this RJR analysis. The top left shows the lab frame which is composed of the visible and invisible systems. The top right shows the CM frame in which the visible objects are divided into either ISR or visible objects associated with the sparticle system. The bottom figure further breaks down the sparticle system into a system composed of sparticle pairs of which both have their own visible and invisible subsystem [1].	34

4.5	R_{ISR} shapes with a basic 1 lepton selection for stop pairs on the left comparing a range of mass splittings. The right distribution is the R_{ISR} shape for the components of the full SM background with the same basic 1 lepton selection [1].	37
4.6	M_\perp shapes with no leptons for di-stop pairs on the left comparing a range of mass splittings. The right distribution is the M_\perp shape for the components of the full SM background with the same lepton multiplicity [1].	38
4.7	2D distributions of R_{ISR} and M_\perp with a basic 2 lepton selection for neutralino-chargino pairs, with LSP and NLSP mass splitting of 10 GeV on the left and tt+jets background on the right. The bump from the left distribution develops a more resolved peak and better signal to background at its center in cases with increasing compression [1].	39
4.8	2D distributions with R_{ISR} versus p_T^{ISR} with a 2 lepton selection and compressed di-stop model with a 20 GeV mass splitting on the left and W+jets background on the right [1].	39
4.9	Distributions of γ_\perp for neutralino and chargino pairs over a range of mass splittings on the left and the comparison of SM background components on the right [1].	40
5.1	Example MET trigger efficiency comparison for Single Muon triggers between data and MC [1].	42
5.2	Cleaning cuts designed to veto events in the red regions with significantly large data to MC R_{ISR} ratios. The accepted region corresponds to events passing the last two criteria of Table 5.1 [1].	43
5.3	Example of relative background presence for tt+jets (left) and W+jets (right) with b-tag counting.	45

5.4	The dotted lines show example 2D R_{ISR} and M_{\perp} binning for each lepton multiplicity with the full SM MC background. The bin edges for each figure are based on the contour of the total background and the number of edges reflect the amount of background [1].	47
5.5	Example internal sensitivity optimization plots. The y-axis is the median asymptotic limit with smaller values indicating stronger expected exclusion of the signal grid points on the x-axis. The x-axis label conventions are $m_{NLSP} - m_{LSP}$ ($m_{NLSP} - m_{LSP}$). The top distribution shows tests performed on TChiWZ with bin consolidation and jet multiplicity consolidation. The bottom distribution tests b-tag counting and γ_T bin optimization on T2tt. . .	50
6.1	Gold (Top-Left), Silver (Top-Right) and Bronze (Bottom) MC truth matching in $t\bar{t}$ sample for 2017. Each figure demonstrates the MC truth composition of each electron quality where a reconstructed electron is ΔR matched to a either a signal electron from a prompt W boson decay, a leptonic tau decay, b-quark jet, c-quark jet, or light quark jet [1].	54
6.2	Gold, Silver, and Bronze efficiency on truth matched prompt signal leptons from W bosons in $t\bar{t}$ +jets. The fake efficiencies are also shown for each lepton quality with leptons truth matched to any other source [1].	55
6.3	Example Tag-and-Probe Z di-muon fits for passing,failing, and all probes with the Medium Id, $ \eta < 1.2$, and $p_T < 20$ GeV	57
6.4	The 2017 individually measured electron efficiencies for Very Loose, ID, Isolation, and Impact parameter in bins of p_T and $ \eta $	60
6.5	The 2017 combined electron efficiencies for Gold, Silver, and Bronze. . . .	61

6.6	Tag-and-Probe efficiencies for the muon Very Loose, Id, Isolation, and SIP3D in 2017. The $p_T < 20$ GeV isolation bins incorporate the efficiency shape fit from Figure 6.7 to extrapolate isolation and SIP3D to low p_T . The Id $p_T < 20$ GeV bins include the J/ψ contribution below 20 GeV. Low p_T binning does not reflect actual bin granularity, bins are merged for readability.	66
6.7	The fitted muon isolation and SIP3D efficiencies for 2017. Both distributions compare data and MC separated between barrel and end-cap.	67
6.8	The combined efficiency components from equations 6.6 and 6.7 and Very Loose for 2017. The low- p_T region (< 20 GeV) includes the contributions from J/ψ as well as the isolation and SIP3D extrapolations. Propagated errors are treated as uncorrelated.	68
6.9	Tag-and-Probe di-muon mass distributions for both passing and failing probes. The top set of plots consist of probes below 20 GeV and the bottom set are above 20 GeV.	69
6.10	Example systematic spread from various fit models and binnings for muons. Includes the four combinations of regions either low or high p_T and central and forward $ \eta $. The starred points are the nominal pdfs, the '*' points use nominal pdfs with variations on the number of fit bins and fit window. The other points use the nominal number of fit bins and window with different signal models such as: Voigtian, Gaussian, Crystalball or a Chebyshev background model.	70
7.1	Distributions that show the relative sensitivity of compressed stop processes in R_{ISR} and M_\perp bins. The top distribution shows 0 lepton and 4 S-jets with color-coded b-tag counting categories. The k^+ denotes high p_T^{ISR} and high γ_\perp categories. The bottom distribution shows 1 gold lepton and 0 S-jets with color-coded lepton flavor categories. The X in both distribution indicates the integration over all sub-categories not explicitly listed.	74

7.2	A comparison of three different signal processes with a 2 lepton selection for R_{ISR} and M_{\perp} bins. The top plot shows gold regions with 0 S-jets which are split by sign or include SVs. The bottom plot shows bronze regions with 1 S-jet split by flavor combinations. Bronze categories are still sensitive at high R_{ISR} despite being considered background rich regions. The X in both distributions indicates integration of all categories not shown.	75
7.3	Pair of k-nary trees illustrating the hierarchical organization of background rates for W+jets and tt+jets.	82
7.4	Comparison of Run II CR fits with Build 62 of Table 7.8 without Poisson treatment (left) and with Poisson treatment (right). The improvement by implementing the Poisson treatment is shown in the RMS and fitted σ of the right distribution, by reducing the number of large outliers due to bins with low statistics.	83
7.5	A comparison of the Poisson corrected builds from Table 7.8 with the first Build 8 on the left and the final Build 62 on the right. Both distributions use only 2016 data and MC scaled to 138 fb^{-1}	84
7.6	The progression of the CR fit log likelihood following the model version milestones listed in the Build Table 7.8.	84
7.7	CR post-fit summary plots split by number of S-jets for 0 and 1 leptons. . .	87
7.8	CR post-fit summary plots split by number of S-jets or lepton category for 2 and 3 leptons. The two included types of splitting shown are not mutually exclusive.	88
7.9	CR post-fit summary plots with the category associated with the root factor of W+jets (top) and a 0 lepton selection splitting by kinematic categories p_T^{ISR} and γ_{\perp} (bottom).	89

7.10 CR post-fit summary plots demonstrating the effects on 2 leptons which are split by lepton categories (top) or a bronze only region which is strongly associated with lepton fake factors (bottom).	90
7.11 CR post-fit summary examples which show the agreement of data to the fitted background model for b-tagging and SV categories.	91
7.12 The Bronze only category fit with fake dominated 1 lepton and 2 lepton bronze categories.	92
7.13 Signal injection and bias test for three different signal grid points. The top left is T2tt with $m_{\tilde{t}} = 750$ GeV and $m_{\tilde{\chi}_1^0} = 670$ GeV. The top right is TChiWZ with $m_{\tilde{\chi}_2^0} = 325$ GeV and $m_{\tilde{\chi}_1^0} = 315$ GeV. The bottom figure uses TSlepSlep with $m_{\tilde{t}} = 250$ GeV and $m_{\tilde{\chi}_1^0} = 245$ GeV [1].	93
8.1 Run II expected cross section upper limits for di stop production, T2tt, excluding stop masses to the left of the 95% CL line.	94
8.2 Run II equivalent expected cross section upper limits for di stop production with an intermediate chargino, T2bW. The MC uses the 2016 samples with 2016 luminosity and 2017 samples scaled to the combined 2017 and 2018 integrated luminosity. The chargino mass is assumed to be halfway between the LSP and stop mass for each grid point.	95
8.3 Run II expected cross section upper limits for Neutralino and Chargino production, TChiWZ, which excludes chargino masses to the left of the line with 95% CL. Shown as a function of the chargino mass and chagino-LSP mass difference. The simplified model uses the Wino-like cross-section and assumes that the initial sparticle pair are mass degenerate $m_{\tilde{\chi}_2^0} = m_{\tilde{\chi}_1^\pm}$	95

8.4	2017 expected cross section upper limits scaled to the full Run II integrated luminosity of 138 fb^{-1} for chargino pairs decaying to an oppositely signed W boson pair. Chargino masses are excluded to the left of the line with 95% CL. Limits are based on wino cross-sections and a sample which is filtered to purely leptonic decays.	96
8.5	Run II expected cross section upper limits that exclude slepton masses to the left of the line at 95% CL. Shown as a function of slepton mass and slepton-LSP mass splitting. The L/R indicates the super partners of the SM left or right handed partner which are assumed to be degenerate in mass.	96
8.6	Dalitz distributions of the phase space parameters x and z. The heatmap compares the uniform phase space simplified model against the model dependent scenarios OS and SS which distribute the four momenta of the decay components differently.	99
8.7	The reweighted difermion invariant masses (left) and an illustration of the momentum partitioning for each reweighting scenario (right)	99
8.8	The expected cross section upper limits for 2016 MC scaled to 138 fb^{-1} . Compares the OS reweighting (top) and SS reweighting (bottom).	100

List of Tables

4.1	Labels for SM background aggregation and relevant signal processes with their CMS shorthand labeling.	31
5.1	Kinematic and combinatorial event requirements.	43
5.2	Kinematic requirements and working points for visible physics objects. . . .	44
5.3	Organization of categories across all lepton multiplicities. The bracketed jet ranges imply counting for all integer numbers of jets within the inclusively listed edges. The b-tag counting is limited based on the allowed number of jets in the category. The SV and γ_\perp splitting indicates two categories of either forward and central η or low and high, respectively. The numbers listed in p_T^{ISR} define the low p_T^{ISR} category edges while the high p_T^{ISR} bin is inclusive for everything above the low bin upper edge. The checkmarks indicate regions that are split by either γ_\perp or SV_η and G/S/B refer to Gold, Silver, and Bronze, respectively.	46
5.4	The complete set of R_{ISR} and M_\perp bin edges. A set of 2D bins have been designed for each allowed lepton and jet multiplicity.	48
6.1	The criteria that define the minimum requirements for an accepted lepton. The electron and muon requirements are equivalent in terms of pseudo-rapidity, vertexing, and isolation but vary in p_T threshold and the MVA VLooseFO working point. The MVA VLooseFO ID also varies between years. The parameters d_{xy} and d_z are the transverse and longitudinal impact parameters, respectively.	53
6.2	Data and MC samples for each year used by the electron Tag-and-Probe. .	58

6.3	Kinematic requirements for the electron Tag-and-Probe components.	59
6.4	Data and MC samples for each year used by the electron Tag-and-Probe. . .	62
6.5	Names of centrally produced J/ψ Tag-and-Probe trees.	63
6.6	Muon bin edges for the J/ψ case, high p_T Z case, and low p_T fitting case Z^L . .	63
6.7	Kinematic requirements for the muon Tag-and-Probe components.	63
6.8	The formulation of Gold, Silver, and Bronze efficiencies as a function of conditional Tag-and-Probe efficiency components.	64
6.9	The electron modeling systematic absolute error derived from the Tag-and-Probe for 2017 data and split into p_T and $ \eta $ regions.	71
6.10	The muon modeling systematic absolute error derived from the Tag-and-Probe data and split into p_T and $ \eta $ regions.	71
7.1	Kinematic nuisance parameter mappings which are applied to the “high” bins. Bracketed jet mappings indicate all integer jet multiplicities between the listed inclusive edges. All factors are assigned a 20% prior uncertainty.	78
7.2	The log-normal nuisance parameter mapping for all b-tag counting categories. Includes all combinations of Process \times Category \times (N_ℓ, N_{jet}^S) multiplicities. All factors are assigned a prior 20% uncertainty.	79
7.3	Lepton category nuisance parameter mapping. The complete set of nuisance parameters is represented by the product of the $N_\ell \times N_{jet}^S$ with an assigned prior uncertainty or 20%. The category !Gold indicates the combined Silver and Bronze categories.	79
7.4	The nuisance parameter mapping split by lepton and jet multiplicity for background processes. The dominant backgrounds W+jets and tt+jets are implemented with a hierarchy parameterization of factors. Global factors indicate mapping to every bin and N_{jet}^S implies each possible number of jets for a given lepton multiplicity.	79

7.5	The nuisance parameters associated to fake leptons. The global or silver or bronze rates are split between MC matched source of either Heavy flavor or Light flavor. The shape systematics are applied per lepton and S-jet combinations but combine HF/LF sources and split by flavor only.	80
7.6	The set of nuisance parameters associated to the categories that involve tagged SVs. The SV counting rates are mapped globally to every bin and the kinematic η separation is split between SVs associated with tt+jets versus SVs associated with anything else.	80
7.7	Additional secondary systematics which account for various scale factors or systematic effects of jet reconstruction and clustering. The nuisance parameters with a (*) are not currently implemented but will be added in later in the final model.	80
7.8	Listing of all the model version milestones with a brief description of each build, its Id number and number of nuisance parameters.	85

Chapter 1

The Standard Model and Supersymmetry

1.1 Introduction

The fundamental building blocks of matter and their interactions are expressed through three of the four fundamental forces of nature via the Standard Model of Particle Physics (SM). The SM is the culmination of over a century of work by many theorists and experimentalists, with roots in the late 19th century. The experimental starting point begins with the establishment of the sub-atomic world through the discovery of the electron by JJ Thomson in 1897 [14], then the proton by Ernest Rutherford in 1917 [15], followed by further development with the solution to the mystery of beta decay by the prediction of the neutrino by Enrico Fermi in 1934 [16], and its discovery in 1957 by Clyde Cowan and Frederick Reines [17]. After the neutrino, the theory of strong interactions is formulated as quantum chromodynamics (QCD) by Murray Gell-Mann and others in the 1960s, providing a description of how protons and neutrons are held together in the nucleus of an atom [18], ushering in the modern Standard Model era. In this era, the theory describing weak interactions from Enrico Fermi in the 1930s is combined with electromagnetic interactions in electroweak theory by Sheldon Glashow, Abdus Salam, and Steven Weinberg in the 1960s [19][20][21] and later confirmed by the UA1 and UA2 experiments with the discovery of the W and Z bosons in 1983[22][23]. Following the establishment of electroweak theory, the term SM is coined in the 1970s describing the collection particle physics theories over the last century. The most recent milestone added to the SM is the discovery of the Higgs boson in 2012 [24][25]. Outlining the inner-workings

from this history of particle physics, this chapter will introduce concepts of the Standard Model, the fundamental particles, fields, their basic properties, and interactions. Expanding from the SM we will discuss potential new physics with an extension of the SM which proposes a new symmetry between fermions and bosons called supersymmetry. Finally, we delve into the specifics of simplified models of supersymmetry and the challenges associated with experimental discovery.

1.2 The Standard Model

The Standard Model is a collection of theories used to predict and reproduce experimental data. The theory itself incorporates four major concepts: Quantum Field theory (QFT), the Dirac equation, the gauge principle, and the Higgs mechanism. These four principles are constrained by physical data and describe the set of elementary particles, known as fermions and bosons. The SM generally refers to the SM Lagrangian, an equation with different sectors that describe different subsets of particles, fields, and their interactions. The SM Lagrangian itself consists of 26 free parameters which are input by hand. These parameters are: the masses of the 12 fermions, 3 coupling constants, g, g', g_s , to describe gauge interactions, 2 parameters to describe the Higgs potential, m_h, v , being the Higgs mass m_h and the vacuum expectation value (vev), and 9 mixing angles describing mixing of different fermionic fields. The 12 fermion mass parameters are subdivided by three neutrinos m_{ν_i} , three charged leptons $m_{\ell_i}^{\pm}$, and six quarks m_{q_i} [26].

QFT provides a description for both known and theoretical particles by combining quantum theory, the field concept, and relativity [27]. The gauge theory aspect describes the exact nature of QFT interactions and provides the mechanisms for the electromagnetic, strong, and weak forces. We know of three gauge fields: \vec{G} which transforms under $SU(3)$ and governs strong interactions, \vec{W} and B which transform under $SU(2)_L \times U(1)$ and govern electromagnetic and weak interactions. The combination of the gauge fields, fermion fields,

and the Dirac equation yields mass eigenstates that represent fermionic matter particles. These matter particles would technically be massless if not for the inclusion of the complex scalar Higgs field. The spontaneous symmetry breaking of the Higgs field creates the non-zero vev responsible for generating the masses of the electroweak gauge bosons and SM fermions [28][29].

The set of Standard Model elementary particles is divided into two subgroups: fermions and bosons. The fermions consist of both charged and neutral leptons as well as fractionally charged quarks. There are three flavors of charged leptons (ℓ), the electron (e), the muon (μ), and the tau (τ). Each charged lepton has a flavor pairing neutral neutrino ν_ℓ . As for the quarks, there are also three generations of pairs of quarks. The lightest set of quarks are the up (u) and down (d) quarks, followed by the charm (c) and strange (s), and lastly the bottom (b) and extremely massive top quark (t). The vector bosons are the force carrying particles which represent the gauge fields. They are comprised of the vector bosons - the photon (γ), gluon (g), the W^\pm , and the Z^0 - along with the singular scalar Higgs boson (h) [5]. The elementary particle's masses, generations, and spins are summarized in Figure 1.1.

The SM is an asymmetric chiral theory, combining three groups: $SU(3)_C \times SU(2)_L \times U(1)$. The L , or left handed, subscript indicates that mirrored fields (with different chiralities) transform differently under the EW gauge group. The consequence of chirality is that the possible combinations between interaction vertices is limited [26]. This peculiar property shows up with the W boson, which only couples to left handed particles or right handed antiparticles. Extensions of the standard model also often extend chiral or symmetrical properties.

1.3 Supersymmetry

Supersymmetry (SUSY) is framework that extends the Standard Model by adding a generator that rotates the spin between bosons and fermions. This introduces a bosonic degree of

Standard Model of Elementary Particles

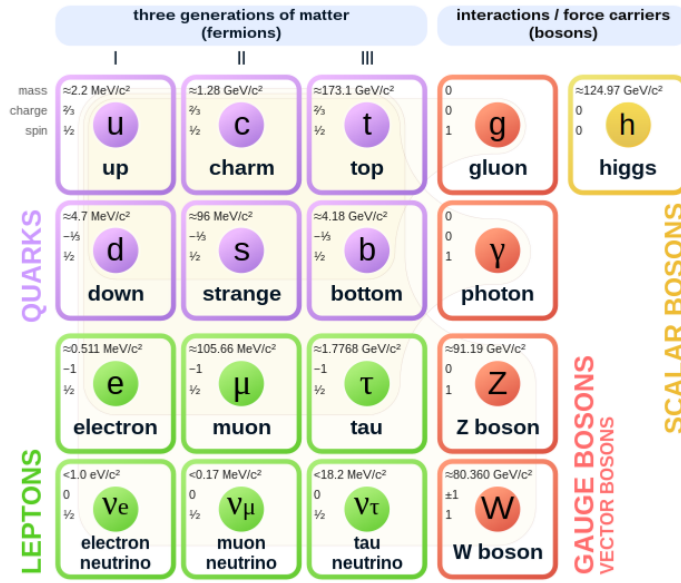


Figure 1.1: The elementary particles of the standard model which includes the color coded categories of fermions and bosons as well as their nominal mass (or mass upper limit), charge, and spin [2].

freedom for every fermionic degree of freedom, and in turn, a super partner for each particle [30]. The resulting set of mirrored elementary particles are referred to as sparticles. Each bosonic sparticle carries the same name as its fermion partner but with an ‘s’ prefix e.g. sfermion, squark, selectron. As for the bosons, with the gauge fields B and \vec{W} , these are accompanied by three super symmetric fields - the Higgsino \tilde{H} , and gauginos represented by the Bino \tilde{B} , and Wino \tilde{W} . The set of boson superpartners can be obtained with the same approach as the SM where the mixture of the B and \vec{W} SM fields are represented by a mass matrix. The diagonalization of the particle matrix leads to mass eigenstates representing the SM particles γ , Z , W^\pm . Similarly, the Higgsino, Bino, and Wino super fields mix to produce four neutral and two charged eigenstates, the neutralinos ($\tilde{\chi}_1^0, \tilde{\chi}_2^0, \tilde{\chi}_3^0, \tilde{\chi}_4^0$) and charginos ($\tilde{\chi}_1^\pm, \tilde{\chi}_2^\pm$) [31]. SUSY also requires an additional Higgs doublet to give mass to up-type and down-type fermions, leading to five Higgs boson states consisting of two charged Higgs and three neutral Higgs [32]. The lightest neutral Higgs of the five available, is usually assumed

to be the experimentally discovered Higgs boson. The full set of SM particles alongside their SUSY partners are illustrated in Figure 1.2. The addition of another Higgs doublet also introduces a second vev. The ratio between the two vevs is denoted as $v_2/v_1 = \tan\beta$ and is an important parameter in experimental searches. An important bookkeeping parameter, similar to lepton number or baryon number conservation, is R-parity. This parameter tallies the total number of SM particles (+1) and sparticles (-1) and expects the product among particles to be conserved in the initial and final states. R-parity conservation then requires sparticles to be produced in pairs. If R-parity is violated, the common consequence is that the lightest supersymmetric particle (LSP) is unstable or models allow protons to decay [33].

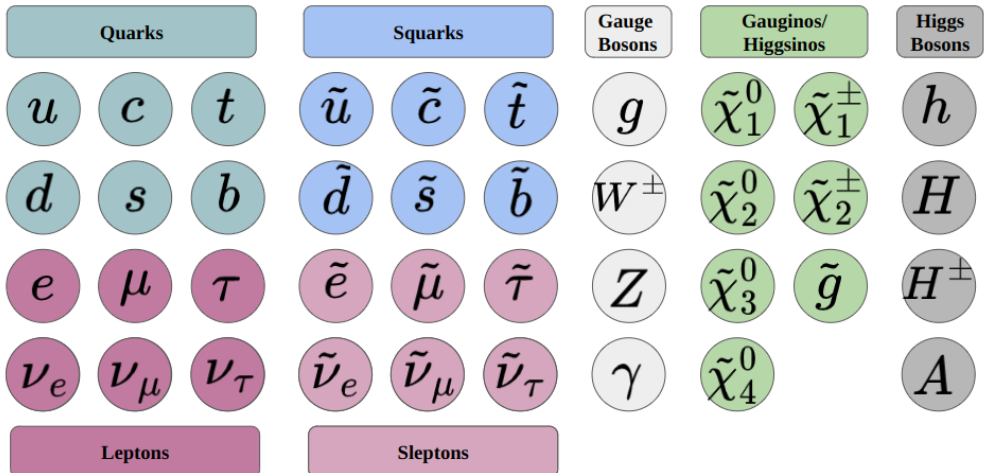


Figure 1.2: The elementary particles of the standard model with their supersymmetric partners.

Supersymmetry is an expansive model and intractable to experimentally test without significant well motivated simplifications. The most experimentally common simplified SUSY model is the Minimally Supersymmetric Standard Model (MSSM). The MSSM contains the smallest number of new particle states and new interactions which are consistent with phenomenology [30]. The MSSM, in full generality, is experimentally inaccessible due to the presence of over 100 parameters. To reduce the problem's dimensionality, further simplification is needed, resulting in a popular simplified model: the phenomenological MSSM (pMSSM). The pMSSM contains 19 parameters which include the masses of each generation

of squark and slepton, parameters to control the mixing of $\tilde{H}, \tilde{W}, \tilde{B}$, and parameters for the Higgs doublet [34]. The pMSSM is still borderline too complicated to attack directly, so, the pMSSM is boiled down into a simplified model of four parameters M_1, M_2, μ , and $\tan\beta$. M_1 and M_2 are the gaugino mass parameters, μ is the Higgsino mass parameter, and $\tan\beta$ is the previously mentioned vev ratio [35]. A model point from this four parameter space is referred to as realistic simplified gaugino-higgsino model, and targets specific regions of MSSM parameter space and experimental topologies. Realistic simplified models are typically used in most experimental searches, including this one.

To effectively grasp the structure of SUSY and various models, either in the pMSSM or simplified models, there are a couple of key elements to consider. First is the mass scale of the relative SUSY sectors, i.e. how massive are the electroweakinos versus the sleptons versus the squarks. If the mass scales are well separated, the sectors are effectively decoupled. If the mass scales are similar then it may introduce complicated cross-talk between sectors. A SUSY search with a 4 parameter simplified model can be further simplified by assuming squarks and slepton masses sit at the several TeV scale while the targeted electroweakinos are at a detectable TeV and sub-TeV scale. By decoupling sectors, outside the sector-of-interest, we remove the interaction between these groups. For example, if sleptons are decoupled from the charginos then complicated dependencies, like cascading between the two decays are avoided. The other key element is the dominant type of super field coupling or the composition of the LSP, typically $\tilde{\chi}_1^0$. A model point can be denoted by the field that dominates the overall LSP mixing, i.e. a Higgsino model LSP would be composed of a majority \tilde{H} [3]. The characteristic take away from simplified model types is that $\tilde{H}, \tilde{W}, \tilde{B}$ controls the nature of the model by governing the cross sections, topology, and how the sparticles interact amongst themselves and SM particles. Two pMSSM examples comparing the mass structure between two arbitrary mass points of a Wino model versus Higgsino model are shown in Figure 1.3. For both models in Figure 1.3, the Higgs and slepton sectors are decoupled at a multi-TeV scale while the squark and gaugino sectors are at an accessible

TeV and sub-TeV scale. Note that small changes in pMSSM model space result in differing electroweakino content and large variations in the relative mass structure and orderings. The difference in cross sections between the same two model points for neutralino/chargino pair production combinations are shown in Figure 1.4. This relative difference in cross section illustrates that the same tweak in parameter space can induce order of magnitude changes in sparticle production. The cross-section difference can also be generalized in terms of the dominant model couplings with the Wino/Bino cross-section being a factor of 8 larger than Higgsino cross-section.

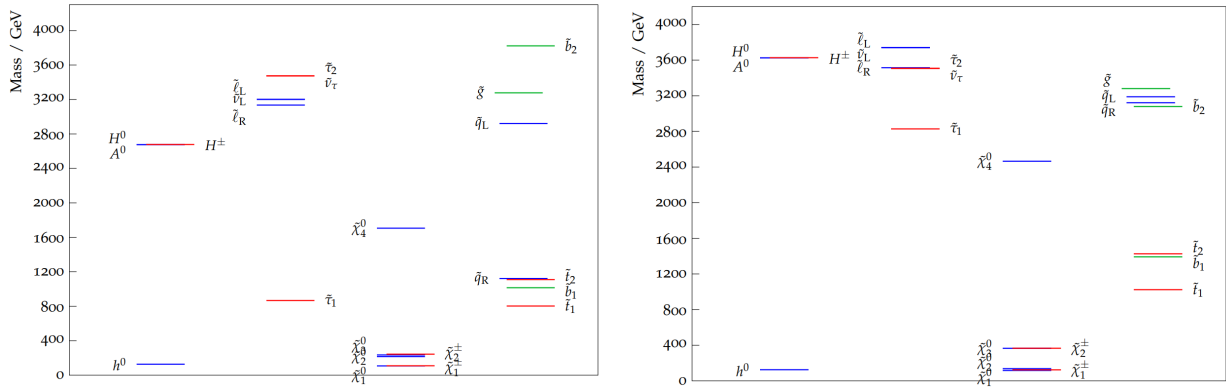


Figure 1.3: Left: Wino-like LSP from PMSSM model point 18898934. Right: Higgsino-like LSP from PMSSM model 6755879 [3]. Both models have a somewhat similar relative mass structure but order of magnitude differences in the Higgs, squark, and slepton sectors.

In addition to the mass structure and cross sections, the decay specifics of each gaugino and Higgsino mixing also vary. The variation in decay modes has a significant impact on the experimental channels and signatures of interest. In an experimental search we would expect the heavier sparticles to decay to both SM particles along with the LSP. If the LSP happens to be close in mass to its parent, say $O(100)$ GeV or less, the model would be considered as a compressed scenario. This scenario is considered compressed because the observable energy of the SM particle involved in a sparticle decay is compressed to a very small amount due to the majority of the available energy being used by the rest mass of the sparticles. Particularly interesting topologies for these compressed models involve decay signatures of processes like $\tilde{\chi}_2^0 \rightarrow Z^* \tilde{\chi}_1^0$, $\tilde{\chi}_2^0 \rightarrow \tilde{\chi}_1^\pm W^\mp$, $\tilde{\chi}_1^\pm \rightarrow W^\pm \tilde{\chi}_1^0$, $\tilde{t} \rightarrow t \tilde{\chi}_1^0$, $\tilde{\ell} \rightarrow \ell \tilde{\chi}_1^0$.

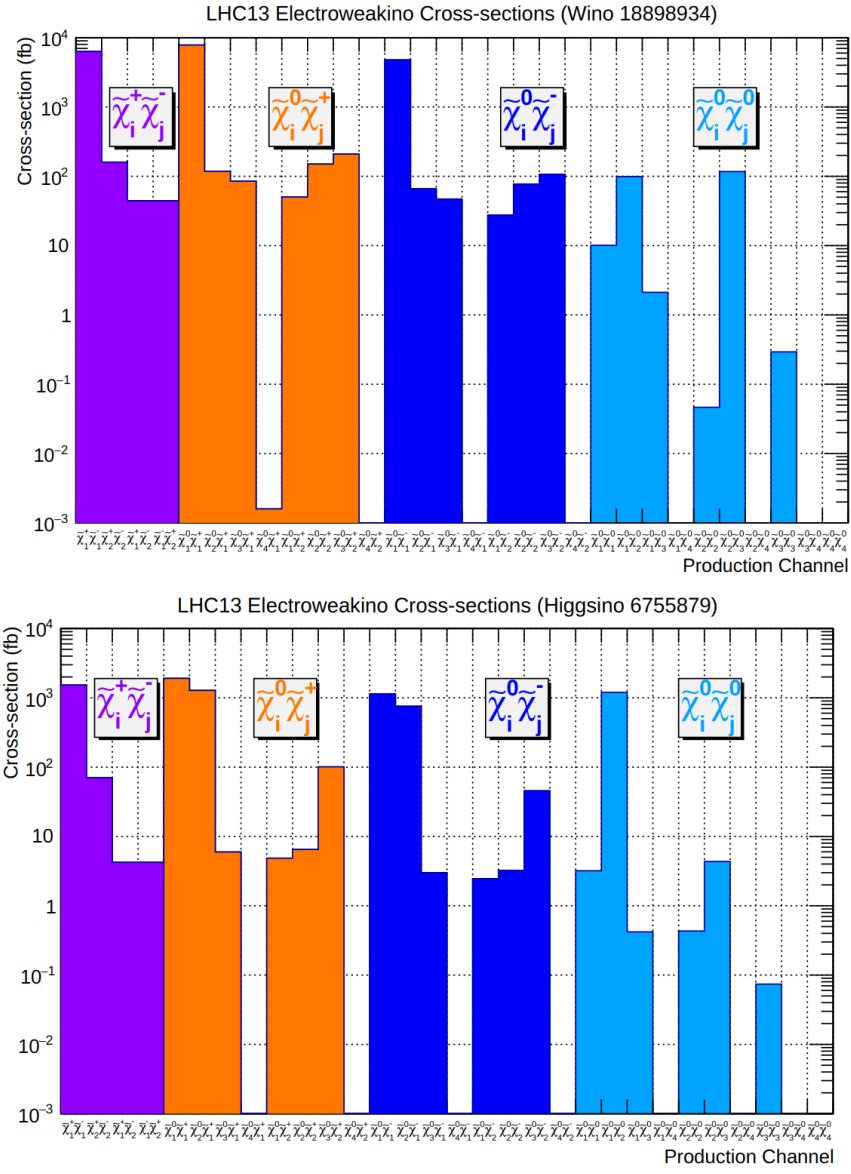


Figure 1.4: Comparison of the Wino LSP and Higgsino LSP models from Figure 1.3 sparticle pair production cross sections.

To further complicate the experimental topologies, the nature of sparticle decay is not only dependent on the superfield mixing but also on the level compression. Figure 1.5 shows the average decay modes for \tilde{H} , \tilde{W} , or \tilde{B} LSPs as a function of mass splittings from a selection of pMSSM models [3].

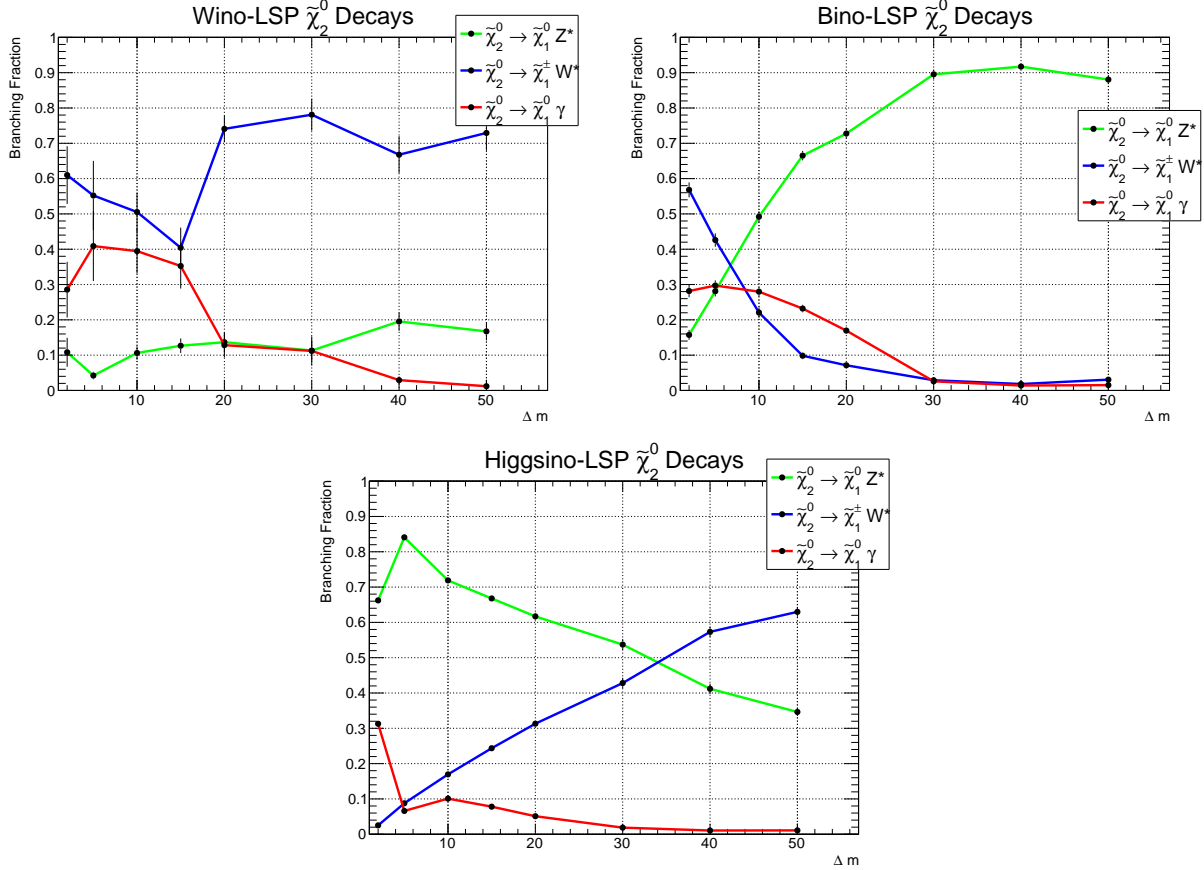


Figure 1.5: Example average neutralino branching fractions for the combined set of pMSSM model points from [3] for $\Delta m < 50$ GeV. The LSP content for each figure is Wino-like top-left, Bino-like top-right, and Higgsino-like bottom. Branching fractions are shown as a function of the mass splitting $\Delta m = m_{\tilde{\chi}_2^0} - m_{\tilde{\chi}_1^0}$. The model with Wino LSP is subject to a W channel enhancement while Z is suppressed. In the Bino case the W channel is suppressed and the Z is enhanced. The Higgsino LSP models can be dominated by either the W or Z channel depending on the mass splitting.

Note that among each model type in Figure 1.5 the Z^* and W^\pm modes can be highly suppressed or enhanced. In some cases, specific modes like $\tilde{\chi}_2^0 \rightarrow \tilde{\chi}_1^\pm W^\mp$ may be kinematically forbidden. Even when kinematically allowed such decay possibilities have often been neglected. Alongside these branching fraction complications, the decay phase space of the final

state particles is also model dependent. For instance, in the case of $\tilde{\chi}_2^0 \rightarrow Z^* \tilde{\chi}_1^0$ the shape of the Z di-lepton mass $m_{\ell\ell}$ distribution changes depending on the sign of the $\tilde{\chi}_2^0$ and $\tilde{\chi}_1^0$ eigenstates. Experimentally this problem is then divided into two possible scenarios: cases where the eigenstates are the same sign and cases where the eigenstates are the opposite sign. The distribution that showcases the $m_{\ell\ell}$ differences under two different model interpretations is shown in Figure 1.6 from a previous ATLAS search [4]. Overall, with the complications of model dependent decays, inherently rare production, varying mass orderings, and relative scale between sectors, the search for SUSY is an extraordinary challenge. To discover SUSY, a reasonable approach is to try to be generically sensitive to all of the formerly discussed complicated nuances.

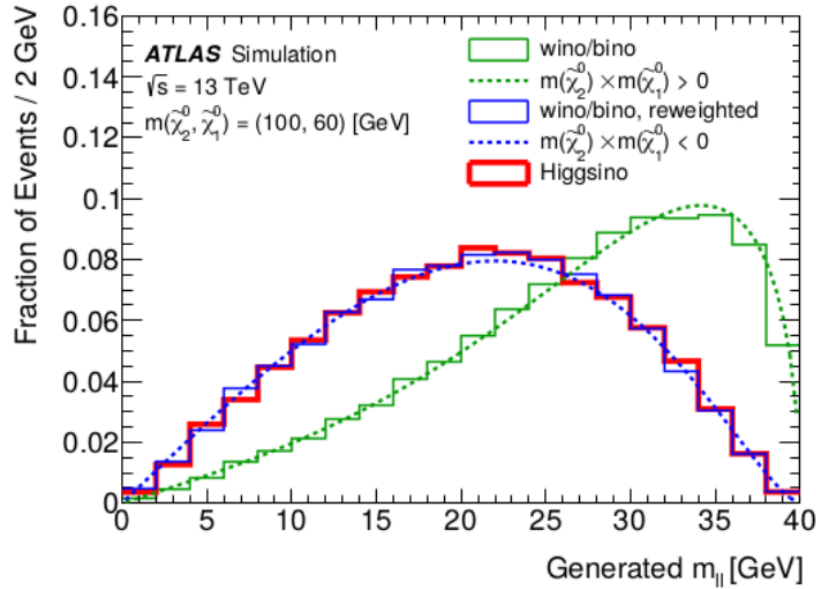


Figure 1.6: Example reweighting of simplified model from an ATLAS search which covers the different dilepton mass line shapes in the same-sign and opposite-sign eigenstate cases [4].

Chapter 2

Motivating the Search for SUSY

2.1 Introduction

The Standard Model is a remarkable theory describing a wide variety of sub-atomic phenomena which has also consistently held up to tests over many orders of magnitude in energy. However, it is not a perfect theory. There are a few experimental and theoretical problems that the SM can not yet explain such as: how to incorporate gravity, how can we explain neutrino mass and mass orderings, and why is the universe made up of matter and not anti-matter? A significant problem in physics, which connects both galactic scale and sub-atomic scale physics, is dark matter. Cold dark matter (CDM) is a type of matter that is thought to have played a crucial role in the formation of large-scale structures in the Universe, such as galaxies and galaxy clusters [36]. The evidence for CDM begins with observations of Zwicky in 1933 where he found that the observed motion of the galaxies in the Coma Cluster could not be explained by the gravitational interactions of visible matter in the cluster, but could be explained by adding additional invisible mass in the form of “dark matter” [37]. Additional evidence for CDM has been compiled over the years such as: gravitational lensing data that disfavors being completely explained by effects of black holes or condensed baryonic matter [38], large scale structure formation where CDM can explain the formation and evolution of galaxy clusters [39], and temperature fluctuations in the cosmic microwave background that suggest the matter content universe is composed of approximately 85% dark matter [40]. Despite overwhelming evidence for the existence of CDM there are no suitable SM dark

matter candidates to explain the abundance of this potential cosmic particle. SUSY offers an attractive solution with the introduction of new particles that can explain dark matter directly via massive invisible particles, such as the neutralino, $\tilde{\chi}_1^0$, or sneutrino $\tilde{\nu}$. The neutralino can handle the CDM problem with models capable of producing the expected CDM relic density of the universe and, in fact, this is used to constrain SUSY model space and simplify searches [6]. Aside from these leading motivations, other more detailed motivations will be discussed in this chapter, the first being the “naturalness problem” with its theoretically aesthetic improvement adding a symmetry to protect against divergent terms in the perturbative expansion of the Higgs mass. The next motivations are experimental, where SUSY offers an explanation for the significant deviation observed in the muon $(g - 2)_\mu$ factor from the recent FNAL result [41], as well as the deviation observed in the W boson mass at CDF II [7]. It should be noted that the divergent Higgs mass - known as the hierarchy problem - can be addressed with SUSY scenarios up to the few TeV scale [42], but, the two latter experimental measurements specifically motivate SUSY compressed scenarios.

2.2 Stabilizing the Higgs mass

An aesthetic attribute of theoretical models is naturalness. We should expect a model to function naturally if the ratio of free parameters in a model are of $O(1)$. Large swings between parameters would be considered fine-tuning and could indicate issues with the underlying theory. So, naturally, if fine-tuning exists in a model, it strongly motivates building extensions to the model to eliminate fine-tuning. One such fine-tuning arises in the hierarchy problem, specifically in the Higgs self interaction terms. The SM Higgs Lagrangian terms that involve self interaction are illustrated in equation 2.1.

$$\mathcal{L} = \frac{gm_h}{4M_W}H^3 - \frac{g^2m_h^2}{32M_W^2}H^4 \quad (2.1)$$

H represents the scalar Higgs field, m_h the Higgs mass, and M_W the W boson mass. A correction to the Higgs mass can be calculated using standard perturbation theory by evaluating the second term of the Higgs Lagrangian [30].

$$\begin{aligned}\Delta m_h^2 &= \langle H | \frac{g^2 m_h^2}{32 M_W^2} H^4 | H \rangle = 12 \frac{g^2 m_h^2}{32 M_W^2} \int \frac{d^4 k}{(2\pi)^2} \frac{i}{k^2 - m_h^2} \\ &= 12 \frac{g^2 m_h^2}{32 M_W^2} \frac{1}{16\pi^2} \left(\Lambda^2 - m_h^2 \log \frac{\Lambda^2}{m_h^2} + O(\frac{1}{\Lambda^2}) \right)\end{aligned}\tag{2.2}$$

The integral term in Equation 2.2 is the propagator for the exchange of a virtual Higgs and is integrated over phase space. Λ is known as the cutoff scale parameter and should be interpreted as the scale at which the SM breaks down, possibly near the Planck scale $O(10^{19})$ GeV. Notice the leading Λ^2 term indicates that the expansion is quadratically divergent. The divergent mass correction means there needs to be extremely large cancellations, around 20 orders of magnitude, to maintain $\Delta m_h \sim O(m_h)$. A similar phenomenon can also be observed with fermion masses, chiral symmetry protects the fermion mass from divergence by guaranteeing corrections at the same order as the fermion masses. SUSY offers a similar protection to the Higgs mass by introducing a symmetry with the additional fermionic and bosonic degrees of freedom leading to similar cancellations and producing a more natural model.

2.3 The Muon Anomalous Magnetic Moment

A major experimental motivation for SUSY lies within the measurement of the muon anomalous magnetic moment [8]. Multiple measurements between two labs, Brookhaven National Lab (BNL) and Fermi National Accelerator Lab (FNAL), have shown significant disagreement with the SM. These experiments measure the muon g factor, or specifically, its deviation from two: $(g - 2)_\mu$. The g factor is related to the electromagnetic coupling of charged particles with the photon and largely depends on the tree-level lepton-photon coupling, but gets small quantum corrections from higher-order loops. The largest correction

is the single photon loop shown in Figure 2.1. To predict the g factor, an SM calculation is performed with three types of quantum corrections: Quantum Electrodynamics (QED), Electroweak (EW), and Hadronic. Corrections from the Higgs are neglected because the effects are not experimentally observable. The g-factor prediction starts at exactly 2, with QED, and then involves quantum corrections up to $O(10^{-11})$. The prediction is compared with an experimental measurement at a very high level of precision. If the observation were to deviate from the SM prediction, it can indicate new and unaccounted for physics interactions with the SM leptons. The current best $a_\mu = \frac{g-2}{2}$ prediction is reported as $a_\mu = a_\mu^{QED} + a_\mu^{EW} + a_\mu^{\text{Hadronic}} = 116591810(43) \times 10^{-11}$ [41]. The QED component enters

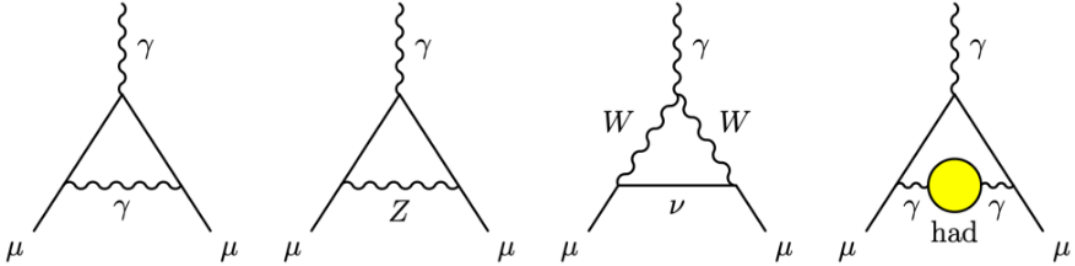


Figure 2.1: Diagrams which contribute to $(g-2)_\mu$. Left is the single photon Schwinger loop that contributes the largest deviation from two. The middle diagrams are electroweak contributions and the far right diagram is the hadronic vacuum polarization the involves a loop with hadrons [5].

at the $O(10^{-3})$ and is known to $O(10^{-11})$. The EW component enters the sum at $O(10^{-9})$ and is known to $O(10^{-10})$. Finally the most complicated hadronic component, contributes at $O(10^{-8})$ and is known up to $O(10^{-9})$. The hadronic contributions arise from Hadronic vacuum polarization (HVP) and light by light scattering (LBL) with the former diagram also illustrated in Figure 2.1. The a_μ^{Hadronic} precision dominates the overall a_μ error and is constrained by data driven measurements alongside the limitations of the computational approach using lattice QCD. The BNL measurement of a_μ yields a difference with the SM prediction of $\Delta a_\mu := a_\mu^{BNL} - a_\mu^{SM} = 279(76) \times 10^{-11}$ which carries a significance of 3.7σ . The most recent a_μ measurement from FNAL confirms the BNL measurement within 1σ and the

combined experimental average increases the SM deviation to a significance of 4.2σ [41].

The 4.2σ deviation is a compelling sign for new physics, but not a smoking gun. It is possible to reduce or eliminate the discrepancy by improving the calculations of the HVP and LBL contributions. New and updated calculations are being performed, attempting to resolve the discrepancy by a few σ , but do not yet fully resolve the differences between observations and theory. If computational improvements can't bring the theory into focus, new particles could introduce quantum corrections which may bring experiment and theory into agreement. Several models qualify and successfully explain the a_μ SM deviation, one being SUSY, where additional diagrams contribute couplings to supersymmetric particles illustrated in Figure 2.2.



Figure 2.2: Example muon diagrams which include sparticle loops that would contribute to $(g - 2)_\mu$ [6]

2.4 The W boson mass

The W boson is an important and peculiar particle, it is the electrically charged boson and couples only with left handed particles. The decay modes follow two channels: (1) the hadronic mode with different flavor quark pairs and (2) the leptonic mode with a charged lepton and neutrino. Measuring the W mass directly is challenging at the LHC due to either high levels of QCD di-jet background or missing energy from the neutrino. The mass parameter itself, m_W , underpins many important parameters in the SM as well. In fact, m_W is related to the Higgs vev, implying that the coupling of the Higgs field to all particles is

effectively tuned by m_W . Similarly, m_W is related to the g factor from $(g - 2)_\mu$, so, both m_W and g can be used to constrain new physics. The W mass can be parameterized at tree level in terms the fine structure constant α , the Fermi constant G_μ and the Z-boson mass m_Z , with higher order radiative corrections, Δr , shown in equation 2.3 [43].

$$m_W^2 = m_Z^2 \left(\frac{1}{2} + \sqrt{\frac{1}{4} - \frac{\pi\alpha}{\sqrt{2}G_\mu m_Z^2}(1 + \Delta r)} \right) \quad (2.3)$$

There is no exact SM prediction of the W mass, but, since there is an interdependence of many parameters such as v , m_z , G_μ, α , the SM prediction is constrained by experimentally well measured parameters. A recent measurement of m_W was performed by CDF II at the Tevatron, where m_W was obtained by fitting the kinematic distributions of light leptonic decays recoiling against a system of jets. The CDF II measurement is 50% more precise than the previous measurement by ATLAS, and heavier than both the ATLAS measurement and SM prediction. The combination of a large deviation with very small error bars results in a significance of 7σ [7].

If follow up experiments confirm the excess in the W mass, it is a definite sign of new physics. The new physics would express itself as new particles in the radiative corrections via equation 2.3. Numerous SUSY models can explain the excessive mass of the W boson, but in general, a slightly heavier W favors light SUSY models, potentially at the electroweak scale, as illustrated in Figure 2.3. A light SUSY model also implies light Higgsinos which favor compressed scenarios. To illustrate the SUSY capability to satisfy both heavy m_W and deviations in $(g - 2)_\mu$, an abundance of model points are shown in Figure 2.4.

2.5 The current status of SUSY

There have been many searches for SUSY particles, starting from LEP and still ongoing at the LHC. There is not yet observed evidence of SUSY, but, there also is not enough lack of observation to fully reject the SUSY hypothesis. The most comprehensively searched

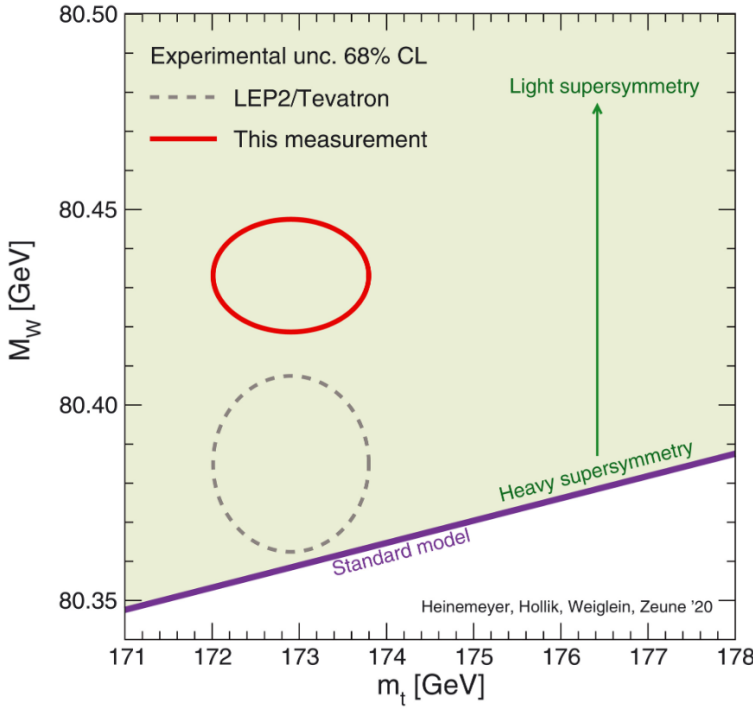


Figure 2.3: The mass of the W boson as a function of top quark mass which displays the CDF II measurement with 68% C.I. compared to the SM prediction and LEP2/Tevatron measurement with 68% C.I [7].

region of SUSY space is related to strong production of SUSY particles. The large expected cross sections for squarks and gluinos compared to the electroweakino or slepton sectors offer the most low hanging fruit for potential discovery. Simplified model searches in ATLAS and CMS have excluded \tilde{g} and \tilde{q} (not including \tilde{t}) up to around 2 TeV, with the most recent limits shown in Figure 2.5 and 2.6 and their sister exclusions of stop squarks around 1 TeV shown in 2.7. The area inside the limit lines in each figure indicates that the 2-D mass points of the sparticle and LSP pair are ruled out at a 95% confidence level for the associated simplified model.

The CMS and ATLAS electroweak limits are shown in Figure 2.8. Note that the electroweak limits have sufficient data to only reach the TeV scale, while SUSY remains possible at the few TeV scale. This leaves significant room in the 2D mass plane to either discover or exclude SUSY by adding more data. One particular simplified model which is nearly unaddressed by both CMS and ATLAS is chargino pair production associated with final states

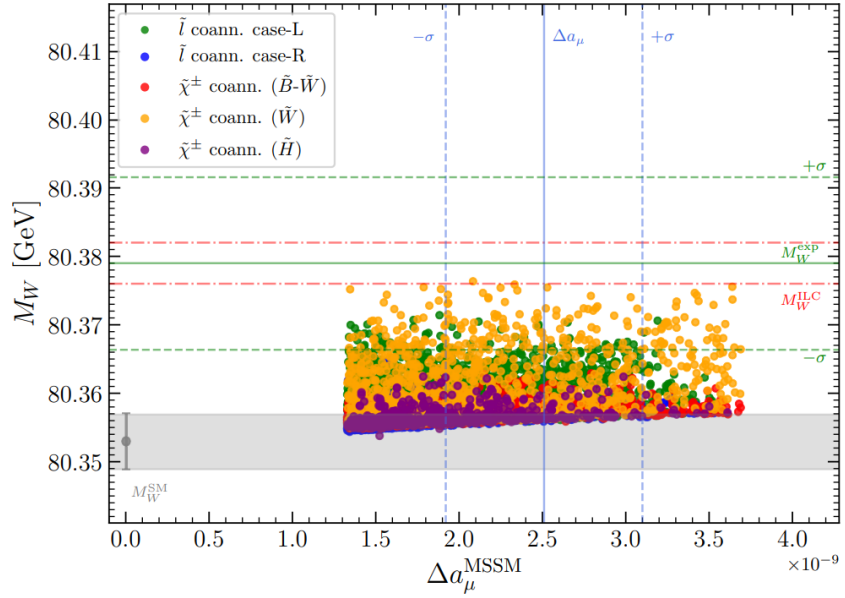


Figure 2.4: Illustration of various color coded model points which correspond to different scenarios and electroweakino model types that favor the measured $(g - 2)_\mu$ and W mass that exceeds the SM prediction. The grey band represents the SM prediction, the green line combines all the experimental results for the W mass, and the blue line indicates the combined $(g - 2)_\mu$ experimental results [8].

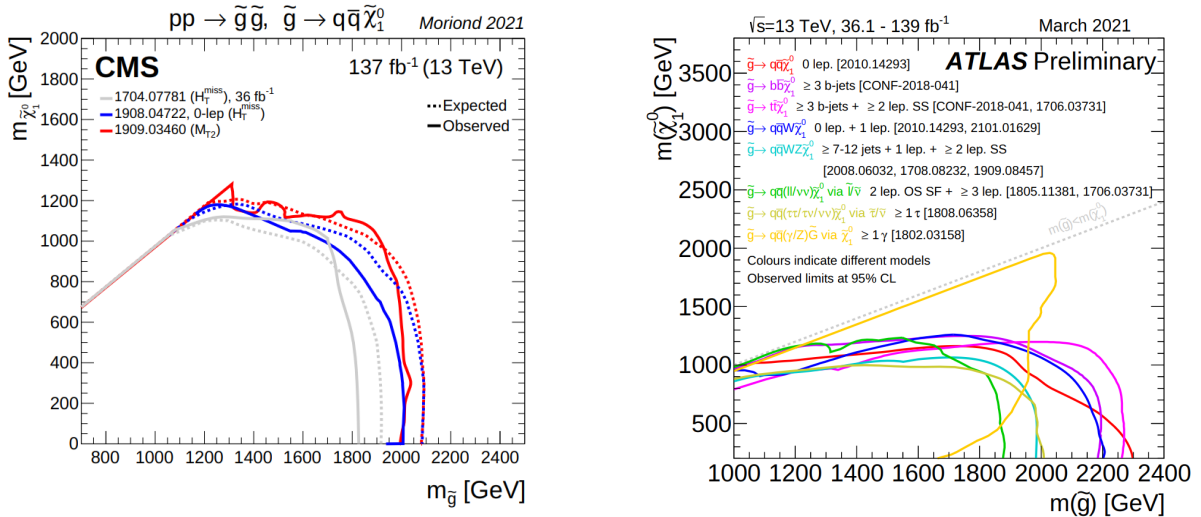


Figure 2.5: The CMS (left) and ATLAS (right) gluino limits from multiple competing channels and models [9][10].

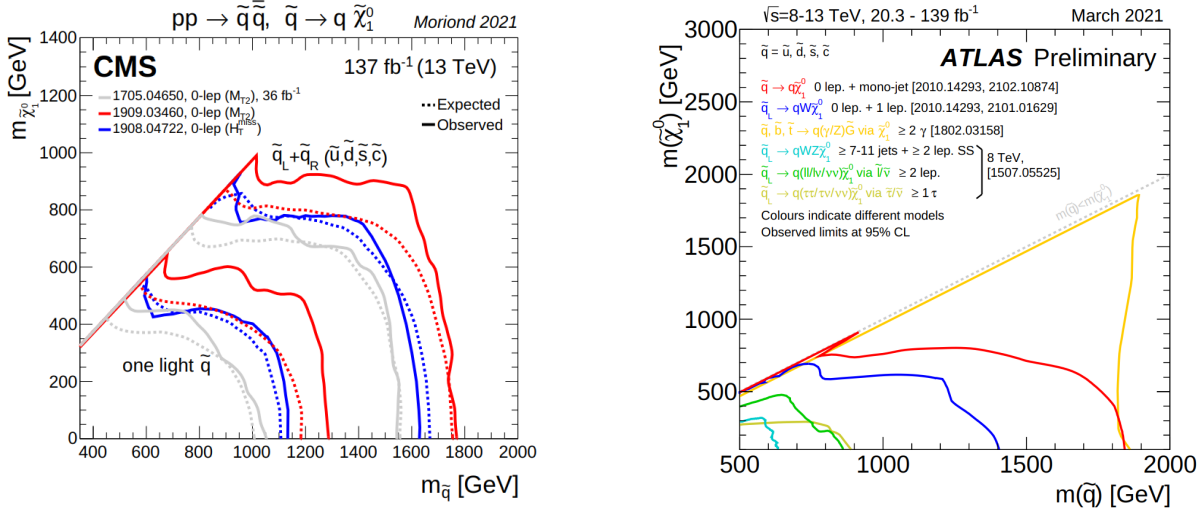


Figure 2.6: The CMS (left) and ATLAS (right) squark limits from multiple competing channels and models [9][10].

with two oppositely charged W bosons. Most simplified models assume a mass degeneracy with $m_{\tilde{\chi}_2^0} = m_{\tilde{\chi}_1^\pm}$ but, there is no reason to believe that $\tilde{\chi}_2^0$ can not be decoupled from $\tilde{\chi}_1^\pm$. If this were the case, the limits would not apply in excluding charginos of any mass, So, it is important to address specific final states. The slepton limits for both CMS and ATLAS are shown in Figure 2.9. These are generally the weakest limits of all the aforementioned processes, but, potentially the most important in association with $(g - 2)_\mu$.

For all of the previously presented limits from CMS and ATLAS, excluding gluinos and squarks, a common thread is that the weakest exclusion regions are the compressed regions. The compressed region varies from process to process. For example, compressed relative to stops is such that the mass difference between the LSP and next lightest supersymmetric particle (NLSP) $\Delta m = m_{NLSP} - m_{LSP}$ is less than the top mass $\Delta m < m_t$. Compression with electroweakinos would have a Δm below the W or Z pole. For sleptons decaying directly to leptons, there are no intermediate heavy particles like a W, Z or t , so, the compressed region is more ambiguous and is considered to be “soft” interpreted as $O(20 - 30)$ GeV or less. Several of the compressed scenarios, are unaddressed by CMS, but are complemented by dedicated compressed searches in ATLAS. However, each ATLAS summary result combines different

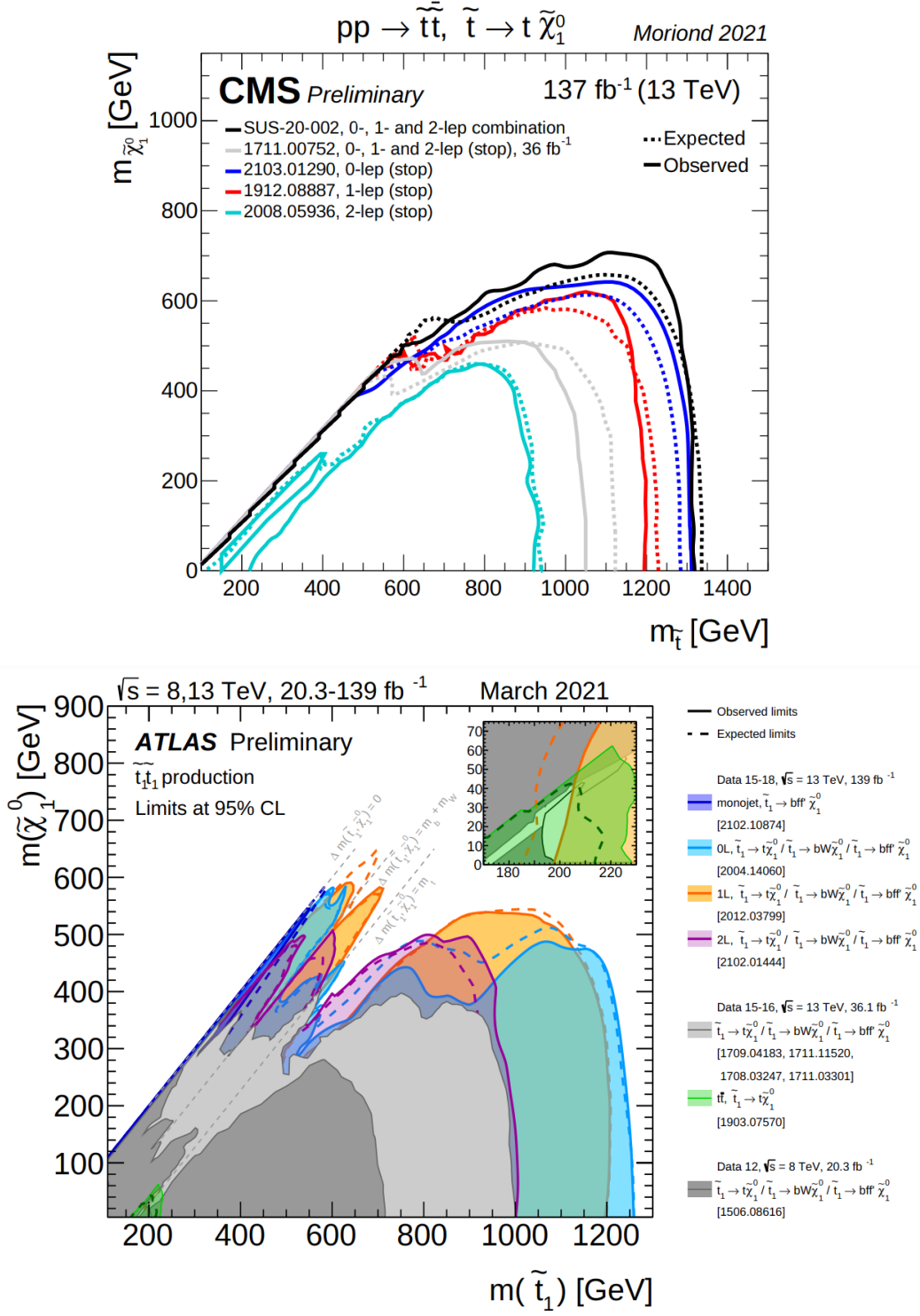


Figure 2.7: The CMS (top) and ATLAS (bottom) limits on stop production [9][10].

searches with the common feature of large gaps between the results. So, based on the current status of all SUSY results, there is a strong motivation to test supersymmetry using CMS data in the compressed regions where there are relatively few comparable results. We expect to extend current limits and provide sensitivity to new final states that have previously not been explored well or at all.

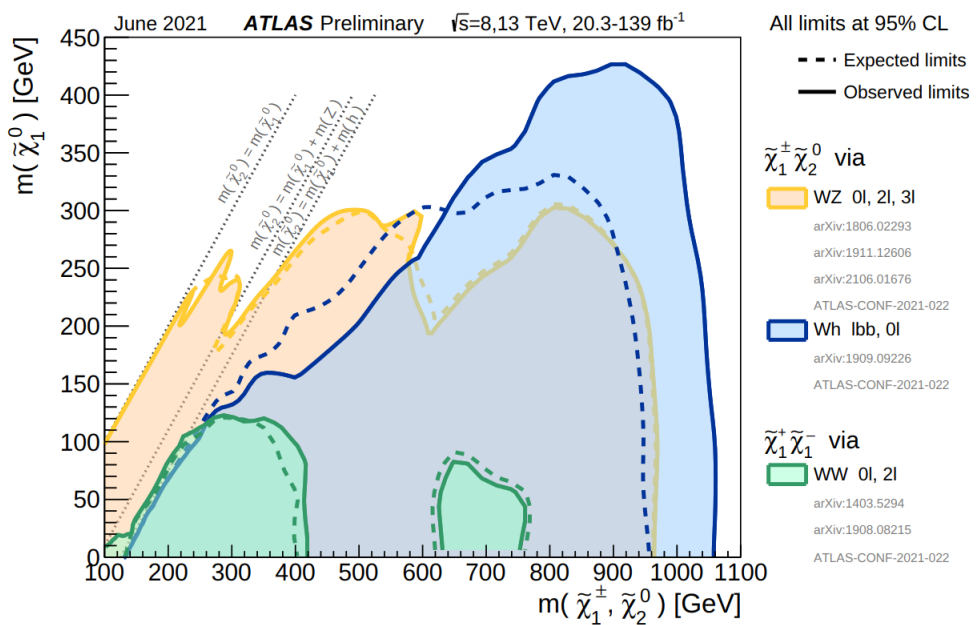
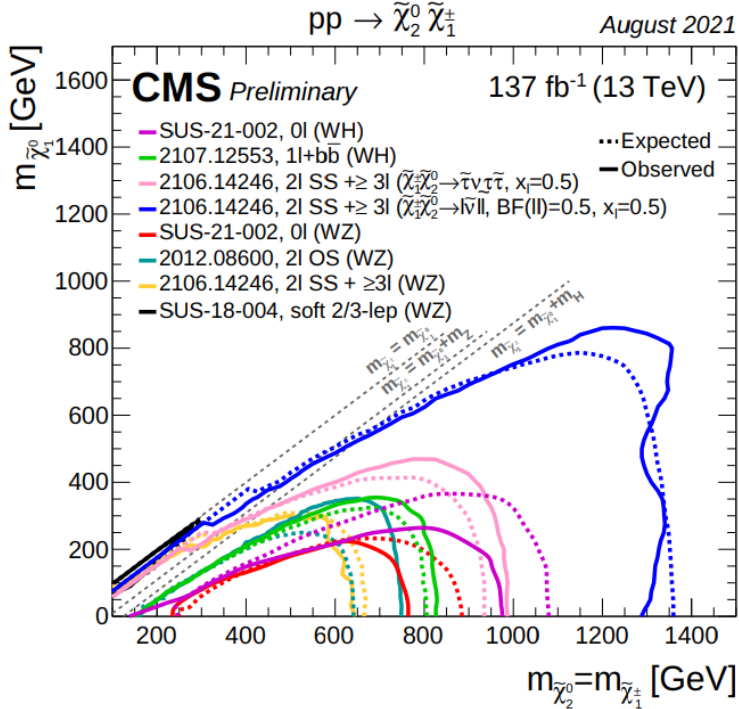


Figure 2.8: The mass limits on chargino pair production with degenerate masses $m_{\tilde{\chi}_2^0} = m_{\tilde{\chi}_1^\pm}$ for CMS (top) and ATLAS (bottom). There are no published limits on compressed chargino pairs in CMS [9][10].

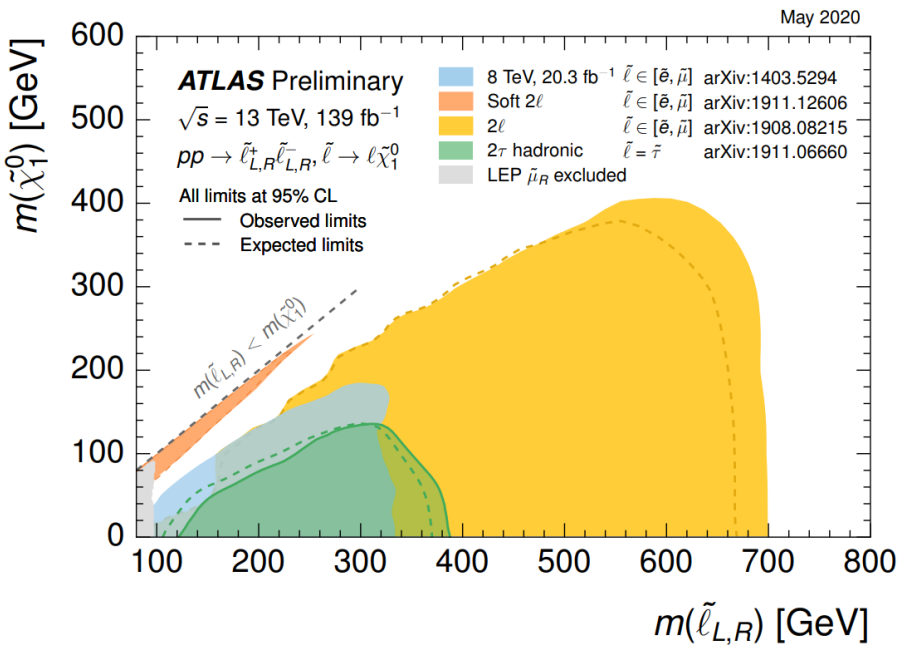
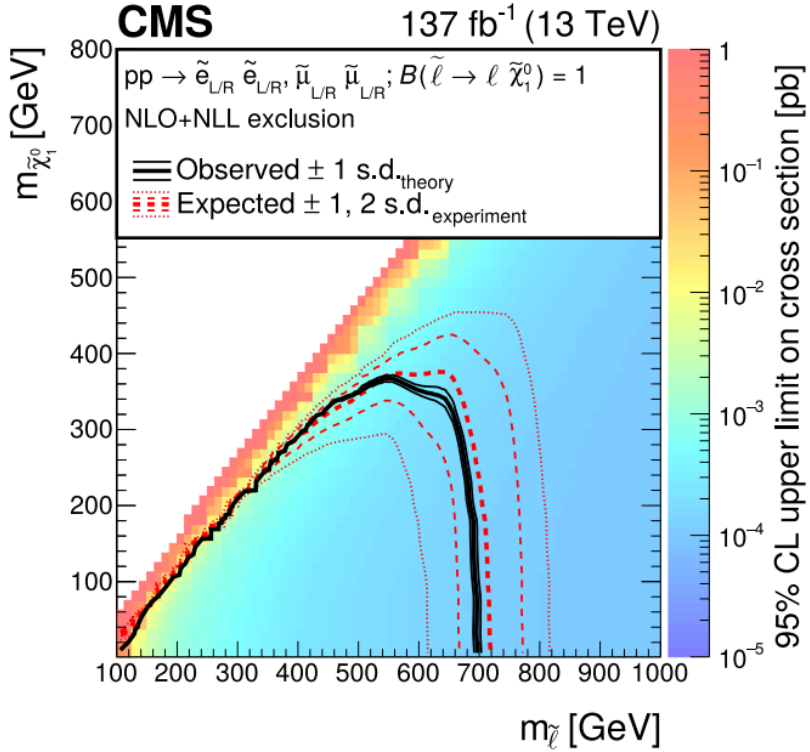


Figure 2.9: The slepton mass limits for CMS (top) and ATLAS (bottom) which assume the same masses for L and R sleptons and combine smuon and selectron production [9][10].

Chapter 3

The CMS experiment

3.1 Introduction

The Compact Muon Solenoid experiment consists of a detector which is a part of the Large Hadron Collider (LHC). The detector encapsulates two synchronous bunches of high energy protons which counter rotate through the LHC accelerator ring. Protons collide at the center of the detector with a large energy and the expectation that more massive and potentially new particles can be produced. Each particle produced in the collision can either decay, interact, or escape detection. The particles that interact are measured by the detector, where different detector layers specialize in measuring certain classes of particles. Then, from energy and momentum measurements, the initial interaction and everything in between is reconstructed.

3.2 The Large Hadron Collider

The LHC is a 27 km circumference circular collider designed to collide proton beams with a center-of-mass energy of 14 TeV and an instantaneous luminosity of $10^{34} \text{ cm}^{-2}\text{s}^{-1}$ [11]. The main accelerator ring consists of two counter rotating proton beams, which are encased in an ultra high vacuum to prevent unintended interactions. The beams are accelerated with cryogenic electro-magnets which operate at -273°C and are cooled by liquid helium. There are two types of magnets present, 1232 dipole magnets which bend the beam around the ring and 392 quadrapole magnets which focus the beams. The beam itself is structured with proton bunches, with each bunch spaced 25 ns apart and about 2800 bunches per beam. The

periods of recording collision data are referred to as runs, of which there are two completed runs denoted as Run I and Run II. The runs have integrated luminosities of 58 fb^{-1} and 138 fb^{-1} with operational center of mass energies of 8 TeV and 13 TeV, respectively. There is also an expected cumulative integrated luminosity of up to 400 fb^{-1} which includes Run I, Run II, and the presently ongoing Run III. Around the accelerator ring there are 4 detectors at different points, CMS, ATLAS, ALICE, and LHCb shown in Figure 3.1.

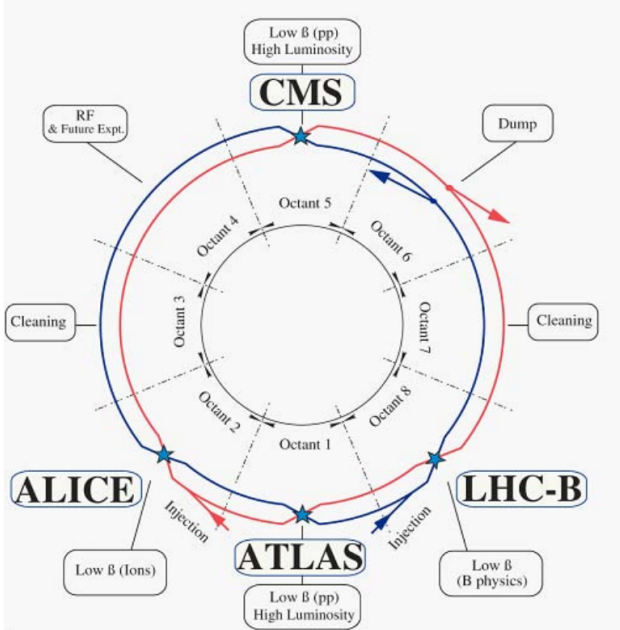


Figure 3.1: Layout of the LHC with the red clockwise beam and blue counter clockwise beam. The beams collide at the interaction regions of the four experiments: CMS, ATLAS, ALICE, and LHCb. [11]

3.3 The CMS Detector

The CMS detector is a hermetic shell that surrounds the interaction point of the two proton beams. The beams collide at the center of the detector illustrated in Figure 3.2. and produce outgoing showers of particles that travel into the detector. The observable outgoing particles, depending on the type of particle, are then measured in one of the specialized concentric layers of the detector. The initial transverse depiction of sub atomic interaction, and intermediate particles, can then be reconstructed from the energy and momentum measured

in the detector. The total longitudinal momentum is not reconstructable for two reasons: first being that the momentum fraction of the initial partons is unknown and second is that some particles travel along the beam line outside the detector acceptance. There is also an abundance of collisions seen by the detector that are not recorded. Instead, interesting events, say due to the presence of a muon or large missing energy, trigger the detector to take a snapshot resulting in a permanent record of the event.

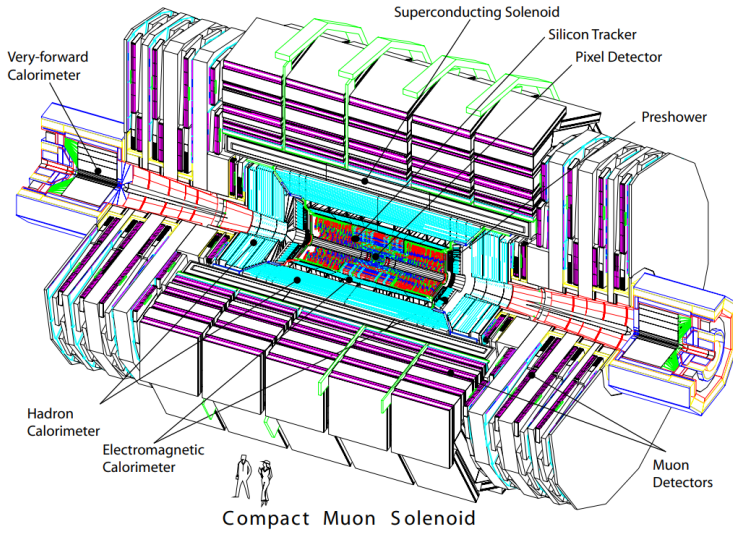


Figure 3.2: Cross-sectional view of the CMS detector and main detector components [12]

The coordinate system adopted for CMS is right-handed with the z axis pointing along the beam line and x axis pointing toward the center of the ring. The origin is defined as the nominal collision point. The angular coordinates are defined as ϕ in the x - y plane, the polar angle θ measured from the z axis, and pseudo-rapidity $\eta = -\log(\theta/2)$. The momentum and energy transverse to the beam direction are denoted as p_T and E_T and are computed from the x and y components [44].

A particle's traversal through the detector, as shown in Figure 3.3, is as follows: Particles are produced post-collision at a primary interaction point, or primary vertex. Other interactions can occur nearby in the same snapshot and are denoted as pile-up, a form of noise obfuscating the primary interaction. From either primary or secondary vertices, both charged and neutral

particles traverse the first region of the detector, the silicon tracker. The vertex selected as the primary vertex, from the set of approximately simultaneously created vertices, is the vertex with the largest scalar sum of transverse momentum from tracks consistent with that vertex. The tracker consists of concentric thin silicon sensors with coverage provided in the barrel up to $|\eta| < 1.2$ and end-cap sensors which extend the acceptance range to $|\eta| < 2.5$. The tracker is also divided into an inner pixel tracker and outer silicon strip tracker. The inner pixel tracker is designed to have high spatial resolution to determine particle origins while being radiation tolerant. The silicon strip tracker complements the pixel tracker by adding significantly more coverage but with less spatial resolution. All tracker sensors register hits from only charged particles with the sequence of hits being connected into a track that represents the path and origin of the charged particle. The next stop is the Electromagnetic Calorimeter (ECAL), which consists of scintillating PbWO₄ crystals that are designed to stop and measure the energy deposits of photon and electrons. These different energy deposits are distinguished by tracks that seed ECAL super clusters. Particles that do not stop inside the ECAL, encounter the hadronic calorimeter (HCAL). The HCAL consists of brass and plastic scintillators that stop the remaining massive particles and measure their energy. The ECAL and HCAL acceptance extends to $|\eta| < 3.0$. The last two regions of the detector are only seen by muons and are the centerpieces of CMS. First is the solenoidal magnet, which generates a 3.8 T uniform magnetic field throughout all of the inner regions of the detector. The magnetic field allows the measurement of two important observables: charge and momentum. A charged particle's path will bend in the presence of a magnetic field, and the clockwise or counter clockwise trajectory indicates the charge, while the curvature of the bend determines the momentum. The outer-most part of the detector is the muon chambers, which similar to the tracker, register a sequence of hits via drift tubes or cathode strips. The tracks in both the tracker and muon chambers can then be combined to precisely measure the momentum of the muon. The muon chamber also has interspersed resistive plate chambers which act as a hardware level muon trigger. The tracker performance has an

efficiency above 99% for muons with $p_T > 1$ GeV and momentum resolution of about 2% for charged tracks in the barrel with $p_T < 100$ GeV. The particles which register in the ECAL and HCAL, have their energy deposits clustered into jets. All particles and jets are then reconstructed according to the particle flow method [13] [12] [44].

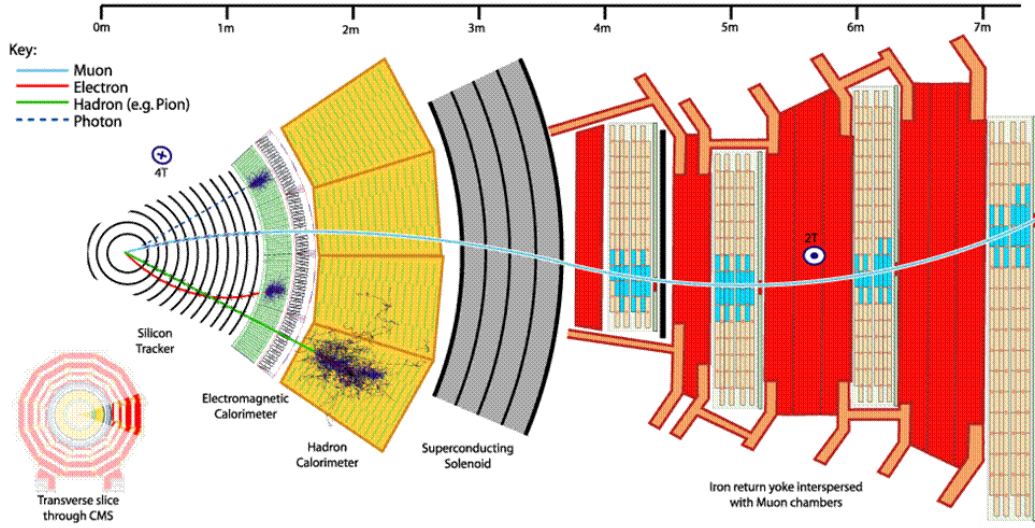


Figure 3.3: A Transverse slice of the CMS detector that illustrates the components that specialize in detecting specific particles [13].

Chapter 4

Compressed SUSY Search

4.1 Data and Simulation

The analysis involves the full Run II data-set, which is divided by the years 2016, 2017, 2018, and has a cumulative integrated luminosity of 138 fb^{-1} . Each year is comprised of $36.31 \text{ fb}^{-1} \pm 1.2\%$ [45], $41.48 \text{ fb}^{-1} \pm 2.3\%$ [46], $59.83 \text{ fb}^{-1} \pm 2.5\%$ [47] in 2016, 2017, and 2018, respectively. The data is modeled by Monte Carlo (MC) that represents the full SM background and is qualitatively grouped by process and final state. The grouping of SM backgrounds is defined in Table 4.1.

The signals being addressed in this search include multiple sparticle processes and final states and will be discussed in more detail in the following sections. A list of the signals and their CMS shorthands that will be used throughout this text is provided in Table 4.1. Each signal is produced according to a mass grid for each year. The raw number of events per mass points and grid spacings for the signals shown are displayed in Figure 4.1 with all years combined.

The majority of signal and backgrounds use the MadGraph [48] generator to model at LO and NLO. The single top backgrounds use PowHEG 2.0 [49] to model at NLO. Parton shower and fragmentation for all samples is done with PYTHIA 8 [50]. Each year is subjected to an underlying event tune with CUETP8M1 for 2016, CP2 for 2017 and 2018 signals and CP5, for 2017 and 2018 backgrounds [51][52]. The detector conditions and response are simulated for all samples with GEANT4 [53]. Pile-up corrections are applied to MC by reweighting

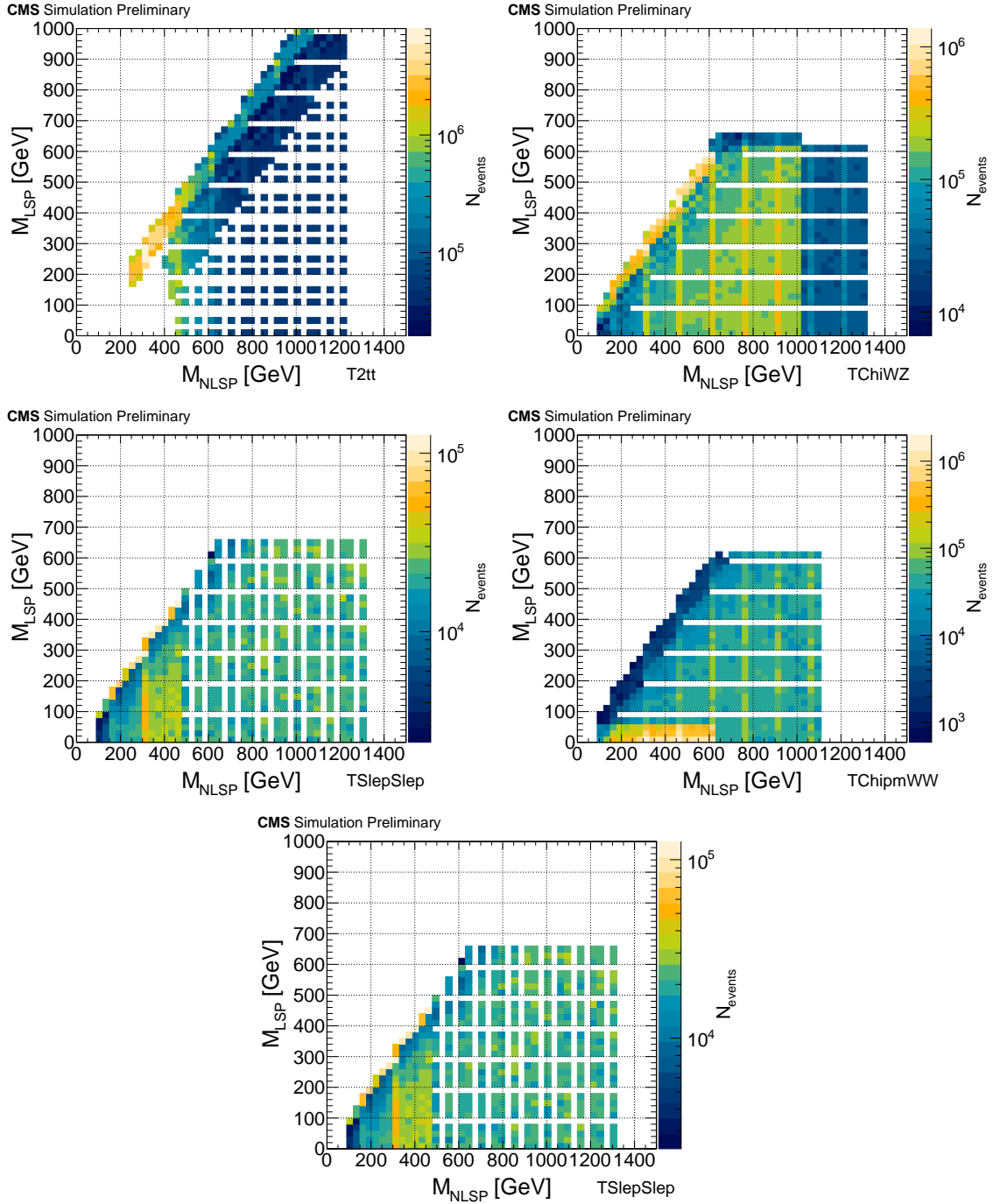


Figure 4.1: Mass grids and associated numbers of events per grid point for each the SUSY processes T2tt, T2bW, TChiWZ, TChipmWW, and TSlepSlep [1].

Table 4.1: Labels for SM background aggregation and relevant signal processes with their CMS shorthand labeling.

Bkg. Label	Bkg. Composition
W + jets	Single W boson, a dominant background that composes about 50% of the total background
tt+jets	$t\bar{t}$ which can be accompanied by a W,Z,h, or γ , the other dominant background composes about 50% of the total background
ZDY Di-boson (DB)	Z+jets and Drell Yan, an intermediate background WW,ZZ,WZ,Wh,Zh, an intermediate background
ST	Single top processes including tW, a rare background
Tri-boson (TB)	WWW,ZZZ,WWZ, WZZ, WZ γ , WW γ , a rare background
Signal Label	Signal Composition
T2tt	$pp \rightarrow \tilde{t}\tilde{t}; \tilde{t} \rightarrow t\tilde{\chi}_1^0$
T2bW	$pp \rightarrow \tilde{t}\tilde{t}; \tilde{t} \rightarrow b\tilde{\chi}_1^\pm; \tilde{\chi}_1^\pm \rightarrow W^\pm \tilde{\chi}_1^0$
TChiWZ	$pp \rightarrow \tilde{\chi}_2^0 \tilde{\chi}_1^\pm; \tilde{\chi}_2^0 \rightarrow Z\tilde{\chi}_1^0; \tilde{\chi}_1^\pm \rightarrow W^\pm \tilde{\chi}_1^0$
TSlepSlep	$pp \rightarrow \tilde{\ell}\tilde{\ell}; \tilde{\ell} \rightarrow \ell\tilde{\chi}_1^0$
TChipmWW	$pp \rightarrow \tilde{\chi}_1^\pm \tilde{\chi}_1^\mp; \tilde{\chi}_1^\pm \rightarrow W^\pm \tilde{\chi}_1^0$

the distribution of number of primary vertices per event to match data.

4.2 Compressed Signal Overview

Influenced by strong experimental and phenomenological motivation for compressed spectra and with the intention to comprehensively test SUSY, we conduct a search designed to be generically sensitive to many compressed final states. The kinematic techniques in this chapter is based largely on the previous work by C. Rogan and the Recursive Jigsaw Reconstruction (RJR) framework [1][54]. The targeted processes include, but are ultimately not limited to, the pair production of stops, electroweakinos, and sleptons, whose diagrams are included in Figure 4.2. Each of the processes in Figure 4.2 has a pair-produced visible system alongside a massive invisible system. For these systems to be compressed, most of the energy available in the sparticle decay is used by the rest mass of the LSP. These small mass splittings lead to low momentum visible products that are difficult to reconstruct or are

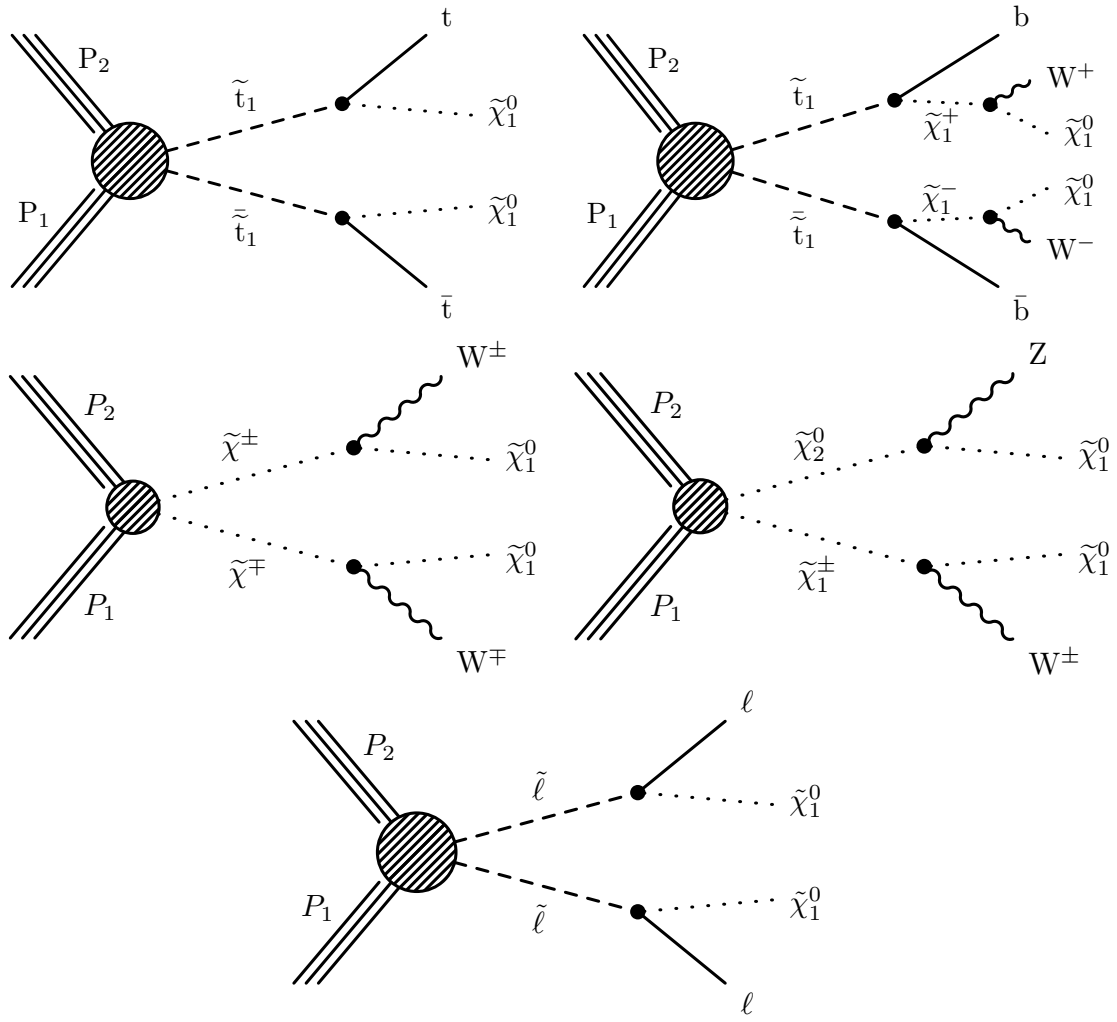


Figure 4.2: Feynman diagrams for SUSY pair produced processes. Top row involves stop pairs where the intermediate state on the top left (T2tt) undergoes stop to stop decay and the top right (T2bW) instead undergoes a stop to chargino decay. The middle left diagram (TChiPMWW) shows chargino pairs decaying to two W boson and the middle right (TChiWZ) is a neutralino and chargino pair which decay into a W and Z boson final state. The bottom diagram (TSlepSlep) shows di-slepton production with sleptons decaying directly to SM leptons.

undetectable. In the case of intermediate massive particles, such as Z boson, these are forced off-shell so the Z visible decay products receive even less momentum because the available energy goes into the mass of the intermediate particle. In order to identify these types of events, we study events with significant initial state radiation (ISR). The ISR system recoils against, or boosts, the sparticle system leading to high missing transverse momentum which is a tractable experimental signature. A depiction of this type of event is shown in Figure 4.3, with objects grouped into either the ISR or sparticle system. The initial sparticle system is then further divided into two sparticle rest frames according to RJR rules. From these rest frames, we compute a basis of kinematic observables that aid in the discrimination of compressed SUSY against SM processes.

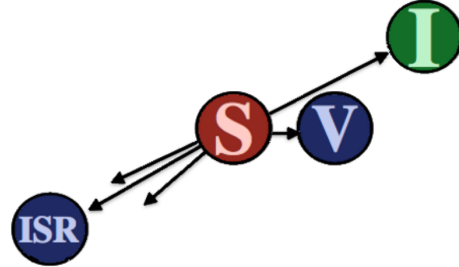


Figure 4.3: Illustration of a visible ISR system recoiling against a sparticle system (S) which can be decomposed into soft visible subsystem (V) and massive invisible subsystem (I) [1].

4.3 RJR Methodology

The ISR-assisted topology involves a collimated invisible and soft visible system recoiling against another visible system of ISR jets. Each event is organized by imposing a decay tree of rest frames onto the visible (V) and invisible objects (I) and assigning the visible components to either the ISR or sparticle (S) side of the event. From the initial assignment, the sparticle system is further subdivided into subsystems a and b where each subsystem has a visible ($V_{a/b}$) and invisible ($I_{a/b}$) component. The three decay trees that contain these sets of objects and reference frames are illustrated in Figure 4.4.

In order to resolve the two invisible four momenta, kinematic and combinatoric unknowns

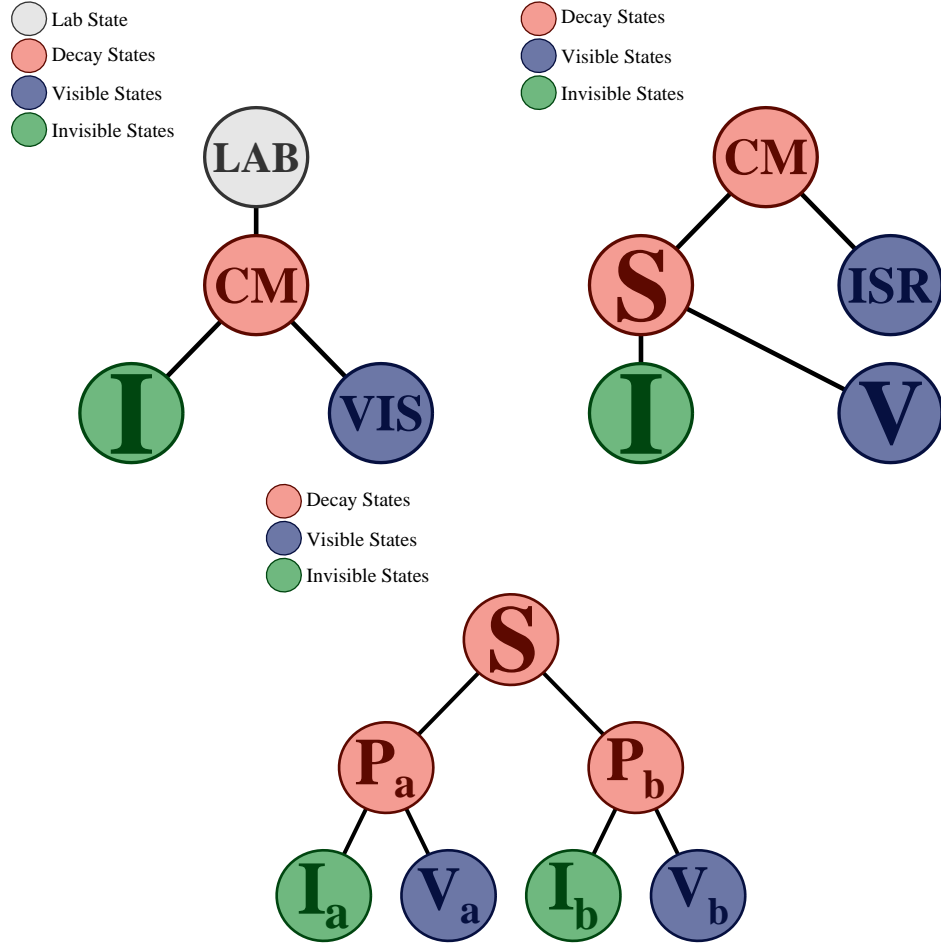


Figure 4.4: A depiction of the three reference frames used in this RJR analysis. The top left shows the lab frame which is composed of the visible and invisible systems. The top right shows the CM frame in which the visible objects are divided into either ISR or visible objects associated with the sparticle system. The bottom figure further breaks down the sparticle system into a system composed of sparticle pairs of which both have their own visible and invisible subsystem [1].

need to be estimated. The visible objects between the ISR and sparticle systems are indistinguishable, so a minimization must dictate the assignment of the visible objects to either the ISR or sparticle system. Similarly, the object partitioning, both for visible and invisible subsystems, can be determined when only the transverse invisible momentum is known. To fully solve the system, the objects need to be assigned to systems and the momentum of each system needs to be estimated. The combinatoric assignment and the estimated four

momenta depend on each other, so we apply a set of rules to simultaneously determine both. RJR provides the framework and rules to organize and evaluate each event [54]. The set of rules used by this analysis are as follows:

1. Assign charged leptons to the S system
 - Targets leptonic sparticle signatures and fixing the leptonic system to always recoil against ISR
2. Fully determine the set of $\{V, ISR\}$ objects by assigning other visible objects to either the S or ISR systems by maximizing the momentum of the sparticle system, p_S^{CM} , in the CM frame

$$\{V, ISR\} = \arg \max_{V, ISR} p_S^{CM} \quad (4.1)$$

3. The visible S system objects are assigned to V_a or V_b by minimizing the masses transverse to the ISR boost axis of each sparticle subsystem, $M_{P_{a/b}}$ in the sparticle rest frame, i.e. grouping objects that are traveling in similar directions

$$\{V_a, V_b\} = \arg \min_{V_a, V_b} M_{P_a}^2 + M_{P_b}^2 \quad (4.2)$$

4. Adjust the total mass of the invisible system, M_I , according to the masses visible systems, $M_{V_{a/b}}$ with the individual particle invisible masses set to zero.

$$M_I^2 = M_V^2 - 4M_{V_a}M_{V_b} \quad (4.3)$$

5. Estimate the longitudinal component of invisible momentum by minimizing total mass in the CM frame, M_{CM} , i.e. determining the transverse mass of V+I systems

$$\vec{\beta}_{CM,z}^{\text{lab}} = \arg \min_{\vec{\beta}_{CM,z}^{\text{lab}}} M_{CM} \quad (4.4)$$

- Determine the full kinematics of I_A and I_B and momentum partitioning by evaluating the S frame velocities, $\vec{\beta}_{P_{a/b}}^S$, through minimizing the mass of the sparticle subsystems

$$\vec{\beta}_{P_a}^S, \vec{\beta}_{P_b}^S = \arg \min_{\vec{\beta}_{P_a}^S, \vec{\beta}_{P_b}^S} M_{P_a}^2 + M_{P_b}^2 \quad (4.5)$$

By iterating through the rest frames and determining the four momenta of the groupings from Figure 4.4, the optimal organization for the event is the one that satisfies the aforementioned RJR prescription. The consequences of this organization are discussed in the following section, where we construct a largely orthogonal basis of kinematic variables to exploit specific characteristics of compressed SUSY and discriminate against SM processes.

4.4 Compressed Kinematics

The main observables are designed to be sensitive to the properties of compressed SUSY, specifically that there are massive invisible particles in the event unlike in the SM. The ISR-system recoils against a massive invisible particle boosting the momentum of the invisible system. The boost of a massive invisible particle can be exploited to discriminate SUSY versus SM through a ratio of ISR and invisible momenta, or approximated by the ratio of invisible mass, m_I , to the invisible particle's parent mass m_P , and defined as R_{ISR} :

$$R_{ISR} = \frac{|\vec{p}_I^{CM} \cdot \hat{p}_{ISR}^{CM}|}{|\vec{p}_{ISR}^{CM}|} \sim \frac{m_I}{m_P} \quad (4.6)$$

In a compressed scenario, the fraction of the invisible momentum to the total ISR kick is expected to be near one due to the visible system using a small fraction of the momentum, making the ISR and invisible system anti-parallel. The peak of the R_{ISR} distribution can be approximated by the ratio of the LSP invisible mass, m_I to the LSP parent mass, m_P . The R_{ISR} distribution contracts around a mean that approaches one as the level of compression increases due to the diminishing available phase space for the visible sparticle objects that

can offset the R_{ISR} ratio. The R_{ISR} behavior doesn't depend specifically on an underlying SUSY process, but only on the fact that there is a heavy invisible system recoiling against ISR. SM massless invisible particle backgrounds do not exhibit the same behavior in R_{ISR} so, the result is strong discrimination between compressed SUSY and SM at high R_{ISR} . This discrimination actually improves as the mass splitting $\Delta m = m_P - m_I$ decreases or as m_P increases such that the ratio m_I/m_P can get closer to one. An illustration of the R_{ISR} shapes comparing signal to background is shown in Figure 4.5

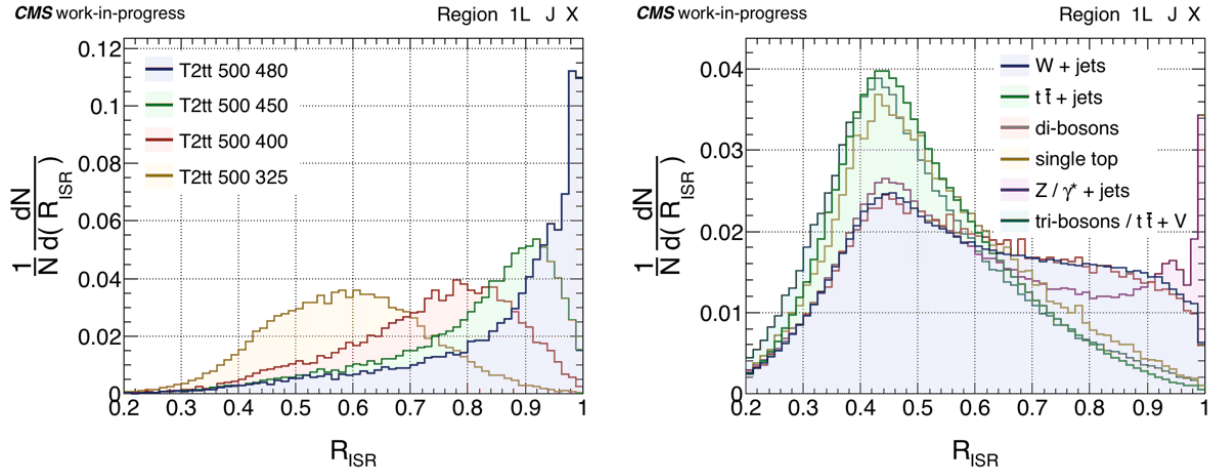


Figure 4.5: R_{ISR} shapes with a basic 1 lepton selection for stop pairs on the left comparing a range of mass splittings. The right distribution is the R_{ISR} shape for the components of the full SM background with the same basic 1 lepton selection [1].

We can also calculate another observable uncorrelated with R_{ISR} , using RJR, that is sensitive to compressed topologies called M_\perp . This observable is constructed from the average squared masses of the sparticle subsystems $M_{P_{a/b}}$ and is explicitly defined as

$$M_\perp = \sqrt{\frac{M_{P_{a\perp}}^2 + M_{P_{b\perp}}^2}{2}} \quad (4.7)$$

The masses of the invisible particles in the sparticle system are set to zero, which is an incorrect assumption in the case of massive invisible particles. The consequence is then that the boost to the sparticle rest frames is sensitive to the inherent mass splittings between the

parent sparticle and LSP. The behavior of the M_{\perp} distribution is that it exhibits a kinematic endpoint or edge at the $\Delta m = m_P - m_I$. An example of the shape of the M_{\perp} distribution with various signal points and backgrounds is shown in Figure 4.6.

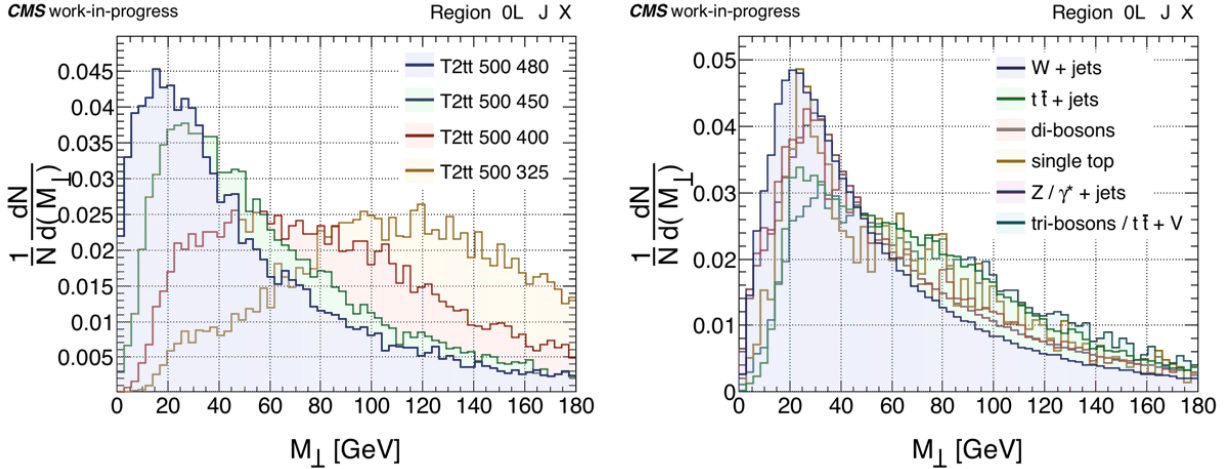


Figure 4.6: M_{\perp} shapes with no leptons for di-stop pairs on the left comparing a range of mass splittings. The right distribution is the M_{\perp} shape for the components of the full SM background with the same lepton multiplicity [1].

The combination of both R_{ISR} and M_{\perp} form a mass-sensitive 2D plane in which to conduct a bump hunt. An example showing the 2D localizations of signal and background is illustrated in Figure 4.7, where the most sensitive region is high R_{ISR} and low M_{\perp} , with sensitivity that improves as mass splittings decrease. Not only is the sensitive signal region at high R_{ISR} useful, the low R_{ISR} region provides a high statistics background-rich region to constrain the background yields in the sensitive region and cross-constrain processes in different categories. Two additional kinematic variables are utilized to aid in discrimination against SM backgrounds. Both are less powerful than R_{ISR} and M_{\perp} but are still very useful. The first quantity is complementary to R_{ISR} and is the transverse momentum of the ISR system p_T^{ISR} . The more momentum in the ISR system the larger the sparticle boost, leading to better resolution in the R_{ISR} distribution. Fortunately, the R_{ISR} distributions from backgrounds are anti-correlated with p_T^{ISR} , so an event with both high p_T^{ISR} and high R_{ISR} has the highest probability of being signal-like. Both correlations for signal and background are

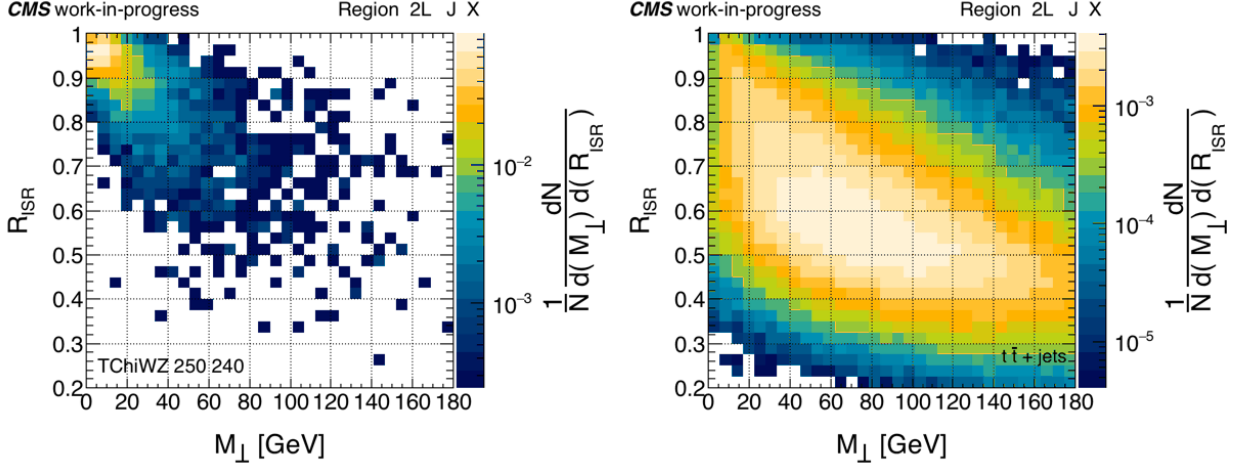


Figure 4.7: 2D distributions of R_{ISR} and M_\perp with a basic 2 lepton selection for neutralino-chargino pairs, with LSP and NLSP mass splitting of 10 GeV on the left and $t\bar{t}+jets$ background on the right. The bump from the left distribution develops a more resolved peak and better signal to background at its center in cases with increasing compression [1].

visualized in Figure 4.8.

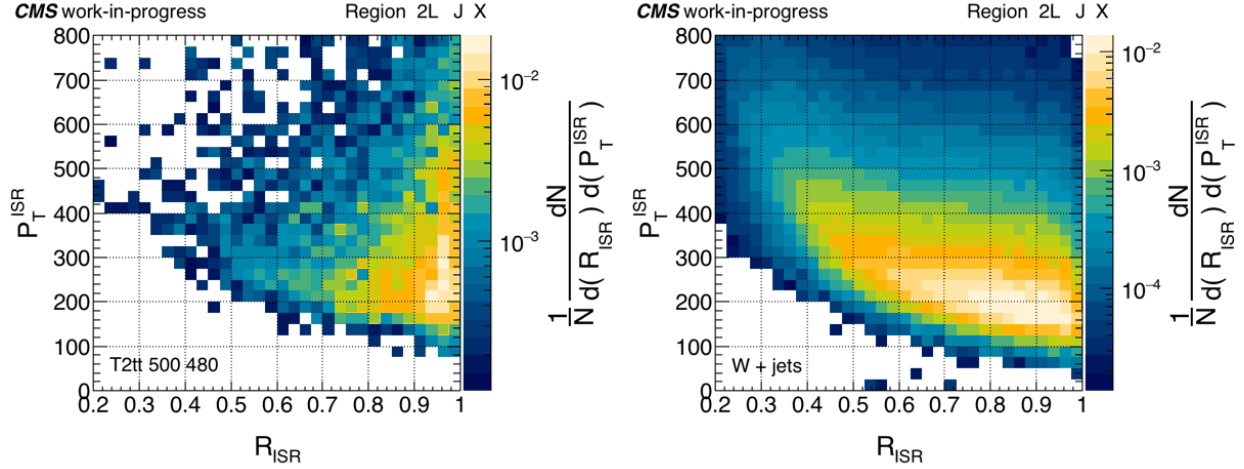


Figure 4.8: 2D distributions with R_{ISR} versus p_T^{ISR} with a 2 lepton selection and compressed di-stop model with a 20 GeV mass splitting on the left and $W+jets$ background on the right [1].

The other complementary kinematic variable used in this search is γ_\perp , a measure of the symmetry of the di-sparticle system and is defined as:

$$\gamma_\perp = \frac{2M_\perp}{M_{S\perp}} \quad (4.8)$$

M_S is the mass of the transverse four momenta of all objects in the sparticle system. The behavior of γ_{\perp} is that it tends to larger values for events with asymmetry in the final state, as illustrated in Figure 4.9. This is useful for isolating signals and backgrounds with semi-leptonic decays of pairs of W or Z bosons. Since both complementary variables p_T^{ISR} and γ_{\perp} do not have the discriminating power of R_{ISR} and M_{\perp} , they are used to categorize events. The p_T^{ISR} categories are separated into high or low categories with the edges depending on the lepton and jet multiplicity. For γ_{\perp} categorization, we also construct high and low categories around $\gamma_{\perp} = 0.5$. The combination of high and low provides a cross-constraint for the background-rich low categories to the signal-rich high categories.

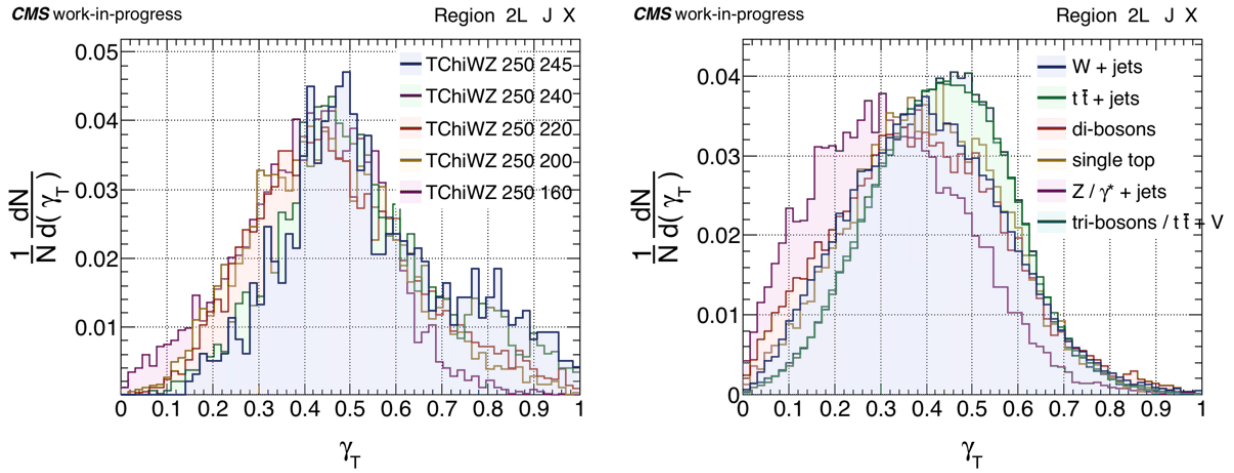


Figure 4.9: Distributions of γ_{\perp} for neutralino and chargino pairs over a range of mass splittings on the left and the comparison of SM background components on the right [1].

Chapter 5

Analysis Description

5.1 Introduction and Strategy

The full analysis is built on the compressed kinematics and RJR strategy described in the previous chapter. The goal of this chapter is to build on this strategy with specific details about the objects and categorization used to potentially discover SUSY. This includes the description of events selected to analyze and their associated physics objects. This being a general search, it casts a wide net to capture a variety of signatures and final states with the consequence being a large number of categories and bins. Finally, I will discuss the data driven strategy to constrain and predict background events in the most sensitive regions with a series of fits to construct and test a fit model.

5.2 Event Selection and Physics Objects

For events to be qualified for analysis, they pass a handful of selected triggers and a preselection that reflects the compressed kinematic description provided in the previous chapter. The triggers used PFMET and PFMHT cross triggers. PFMET is particle flow missing transverse energy which is expected to capture the p_T^{miss} from the LSP. The threshold for the PFMET trigger is that the missing transverse energy is above 120 GeV. The definition of missing momentum is the negative sum of all visible momentum and is as follows:

$$p_T^{\text{miss}} = - \sum p_T^{\text{vis}} \quad (5.1)$$

PFMHT is expected to trigger on events with significant jet activity which are likely candidates for ISR events. The threshold for PFMHT is that the scalar sum of all visible transverse momentum is above 120 GeV. In general, the compressed SUSY topology is a somewhat rare organization of an event, due to the uncommon nature of these events, the MC modeling does not always sufficiently and precisely describe data, so, a data driven approach is utilized for physics objects to compensate for any disagreement. This approach compares the overall efficiency or behavior of selected objects and computes data driven scale factors, while also providing a platform to model and understand systematic effects. These scale factor calibrations are then applied to MC to bring data and MC into agreement. The instance of scale factor generation arises in the modeling of the trigger efficiency, with efficiency defined as events that pass the trigger and preselection versus only preselection. The comparisons of data and MC missing E_T efficiency are shown in Figure 5.1 with the efficiency shapes modeled by a Gaussian CDF.

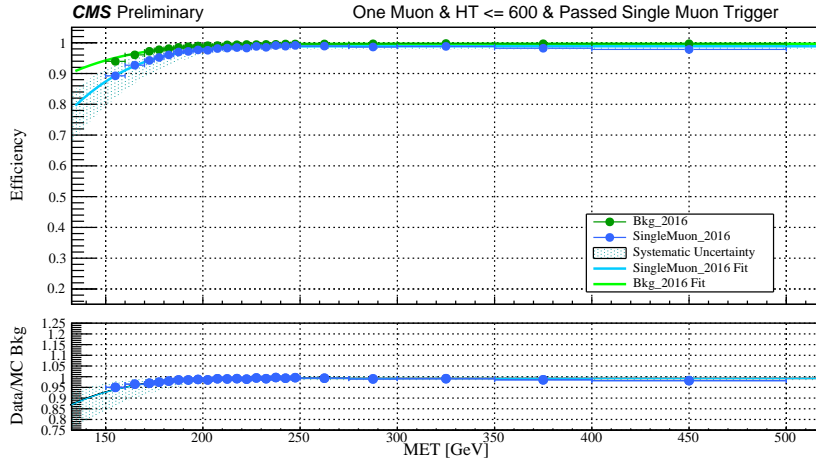


Figure 5.1: Example MET trigger efficiency comparison for Single Muon triggers between data and MC [1].

The preselection is a set of carefully studied criteria to remove background and mismodeled events while selecting events with objects associated with signals. The preselection consists of the criteria listed in Table 5.1 and introduces three quantities p_T^{CM} which is the vector sum of the transverse momentum of the CM frame, $\Delta\phi_{p_T^{\text{miss}}, V}$ the angle between the visible

Table 5.1: Kinematic and combinatorial event requirements.

Preselection Requirements	
Criteria	Description
$N_V \geq 1$	At least one visible object assigned to the S system
$N_j^{ISR} \geq 1$	At least one jet assigned to the ISR system
$p_T^{\text{miss}} > 150 \text{ GeV}$	Minimum transverse missing energy based on trigger efficiency
$p_T^{ISR} > 250 \text{ GeV}$	Minimum ISR kick to resolve massive invisible particles
$R_{ISR} > 0.5$	Target Massive LSPs
$ \Delta\phi_{\vec{p}_T^{\text{miss}}, V} < \pi/2$	Ensures visible and invisible system are traveling in the same direction
$p_T^{CM} < 200 \text{ GeV}$	Rejects mismodeled events
veto $f(\Delta\phi_{CM,I}, p_T^{CM})$	2D function to also reject mismodeled events - See Fig 5.2

and invisible system, and $\Delta\phi_{CM,I}$ the angle between p_T^{CM} and the invisible system. There is an additional parabolic cleaning cut which vetoes events outside of the curves:

$$\pm 2.777\Delta\phi_{CM,I}^2 + 1.388\Delta\phi_{CM,I} + 0.8264 \quad (5.2)$$

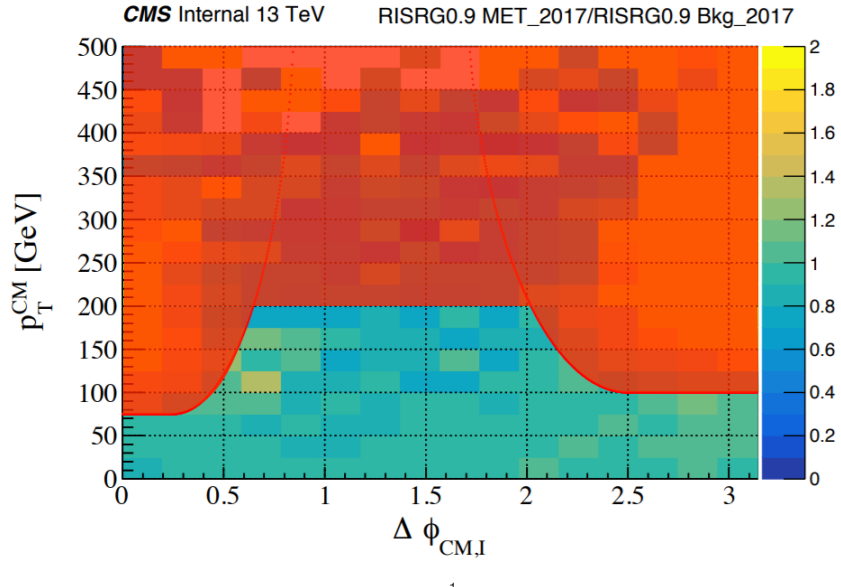


Figure 5.2: Cleaning cuts designed to veto events in the red regions with significantly large data to MC R_{ISR} ratios. The accepted region corresponds to events passing the last two criteria of Table 5.1 [1].

Table 5.2: Kinematic requirements and working points for visible physics objects.

Visible Physics Objects	
Jets	AK4 PF Jets Tight ID $p_T^{jet} > 20$ GeV $ \eta < 2.4$
B-tagged Jets	AK4 PF Jets DeepJet Medium WP $p_T^{b-jet} > 20$ GeV
SVs	$2 < p_T^{SV} < 20$ GeV
Leptons	Very Loose ID $p_T^{\mu^\pm} > 3$ GeV $p_T^{e^\pm} > 5$ GeV Gold/Silver/Bronze quality classes

The preselection forms the basis for an event to be analyzed. Following preselection, the physics objects can be selected, classified, and categorized. The possible object composition can consist of jets, b-tagged jets, soft secondary vertices (SVs), and leptons. The discussion of the leptons and their classification will be reserved for the following chapter alongside the calculation of lepton scale factors. A summary of these physics objects and their kinematic requirements are listed in Table 5.2. The AK4 jets are clustered with the anti- k_t algorithm and $\Delta R = 0.4$ [55] and selected based on working points (WP) defined by their physics object group which are standard objects used in CMS physics analysis [56]. The b-tagging is done by the MVA based DeepJet NN [57] which only identifies b-jets $p_T \geq 20$ GeV. SVs above 20 GeV are tagged using Inclusive Secondary Vertex Finder [58]. A complementary SV tagger was developed which efficiently extends the SV tagging range $2 \leq p_T \leq 20$ GeV for final state topologies with very soft b-jets [59].

5.3 Categorization

Once an event passes the preselection and the leptons are classified, the event is then categorized based on object composition, object multiplicity, and kinematic characteristics. The

goal of categorization is to finely split up background and create generically sensitive regions for any type of signal. The regions with no signal function as control regions and constrain the background prediction in the sensitive regions. The most fundamental categories for the analysis are the lepton and jet multiplicities, events can contain either 0, 1, 2, or 3 leptons and are accompanied by a range of sparticle system jets (S jets) from $0 \leq N_{S_{jet}} \leq 5$ where the upper limit of S jet counting is dependent on the lepton multiplicity. The type of jets are also counted i.e. whether or not the jets have been tagged as b-jets. The b-jet counting is dependent on the lepton multiplicity and restricted by the maximum number of S jets per jet multiplicity category. ISR system can have jets can have 0 or ≥ 1 b-jets and the S system can be composed of 0, 1, or ≥ 2 b-jets. SV tagging is similar to ISR jet counting in the S system, but, SVs are not counted in the ISR system. Events with SVs are further classified based on their orientation being either central or forward with respect to $|\eta| = 1.5$ with the forward range at of maximum of $|\eta| < 2.4$. The counting of b-jets and SVs is very important because it creates categories that isolate $t\bar{t}+jets$ and stop signals and similarly the opposite regions are created with no b-jets that isolate backgrounds like $W+jets$ and signals such as TChiWZ. The benefit of having different object counting regions is that they can cross-constrain each other and is illustrated in Figure 5.3, showing the presence and absence of $t\bar{t}+jets$ or $W+jets$ backgrounds based on S system b-jet counting.

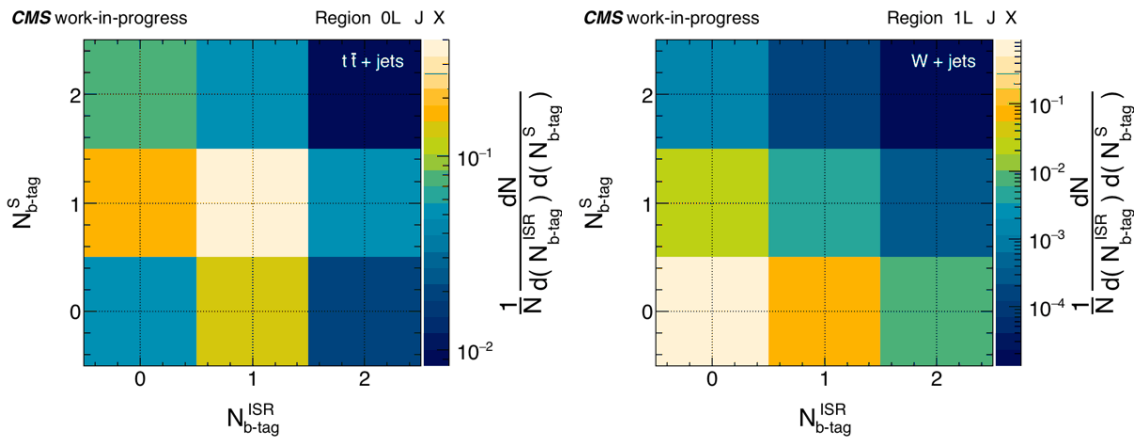


Figure 5.3: Example of relative background presence for $t\bar{t}+jets$ (left) and $W+jets$ (right) with b-tag counting.

Table 5.3: Organization of categories across all lepton multiplicities. The bracketed jet ranges imply counting for all integer numbers of jets within the inclusively listed edges. The b-tag counting is limited based on the allowed number of jets in the category. The SV and γ_\perp splitting indicates two categories of either forward and central η or low and high, respectively. The numbers listed in p_T^{ISR} define the low p_T^{ISR} category edges while the high p_T^{ISR} bin is inclusive for everything above the low bin upper edge. The checkmarks indicate regions that are split by either γ_\perp or SV_η and G/S/B refer to Gold, Silver, and Bronze, respectively.

Obj. Combinatorics							Obj. Kinematics		
N_ℓ	ℓ Type	ℓ Quality	N_{jets}^S	$N_{b\text{-tag}}^S$	N_{SV}^S	$N_{b\text{-tag}}^{ISR}$	SV_η	γ_\perp	p_T^{ISR}
0	-	-	0	0	[1, ≥ 2]	-	✓	-	≥ 350
0	-	-	1	-	≥ 1	-	✓	-	≥ 400
0	-	-	1	-	0	-	-	-	[400, ≥ 550]
0	-	-	[2, ≥ 5]	[0, ≥ 2]	0	[0, ≥ 1]	-	✓	[350, ≥ 500]
1	e^+, e^-, μ^+, μ^-	G	0	0	0	[0, ≥ 1]	-	✓	[350, ≥ 500]
1	ℓ^+, ℓ^-	G	0	0	1	-	✓	-	≥ 350
1	e, μ	G	1	0	≥ 1	-	✓	-	≥ 350
1	ℓ	G	[1, ≥ 4]	[0, ≥ 2]	0	[0, ≥ 1]	-	✓	[350, ≥ 500]
1	e, μ	S/B	[0, ≥ 1]	0	1	-	✓	-	≥ 350
1	e, μ	S/B	[2, ≥ 4]	-	-	-	-	✓	[350, ≥ 500]
2	$e^\pm e^\mp, \mu^\pm \mu^\mp$	G	0	0	0	[0, ≥ 1]	-	✓	[250, ≥ 350]
2	$e^\pm \mu^\mp$	G	0	0	0	[0, ≥ 1]	-	✓	[250, ≥ 350]
2	Z, noZ	G	[1, ≥ 2]	[0, ≥ 1]	-	[0, ≥ 1]	-	✓	[250, ≥ 350]
2	$\ell^\pm \ell^\pm$	G	[0, ≥ 2]	-	-	-	-	-	[250, ≥ 350]
2	$ee, \mu\mu, e\mu$	S/B	[0, ≥ 2]	-	-	-	-	-	≥ 350
2	$\ell\ell$	G/S/B	0	0	≥ 1	-	✓	-	≥ 250
3	Z, noZ	G/S/B	[0, ≥ 1]	-	-	-	-	-	≥ 250
3	$\ell^\pm \ell^\pm \ell^\pm$	G/S/B	-	-	-	-	-	-	≥ 250

Aside from jet counting, there is lepton and kinematic categorization. The electrons and muons are separated by flavor, charge, quality, and Z/noZ candidate. A Z candidate is defined as an opposite sign, same flavor pair (OSSF) in events with 0 S jets and OSSF in the same A or B hemisphere in events with S jets. A compressed scenario expects an off-shell Z so there is no mass requirement on the OSSF lepton pair in a Z category. The complementary compressed kinematic observables p_T^{ISR} and γ_\perp both have a high and low category. A complete table of all the categories is included in Table 5.3.

Each category is divided into a 2D set of (R_{ISR}, M_\perp) bins. The number of bins and bin edges are optimized for each combination of lepton and jet multiplicity. An example binning of the sensitive variables with the total SM background in each lepton multiplicity is shown in

Figure 5.4 and a full table of all binnings is included in Table 5.4.

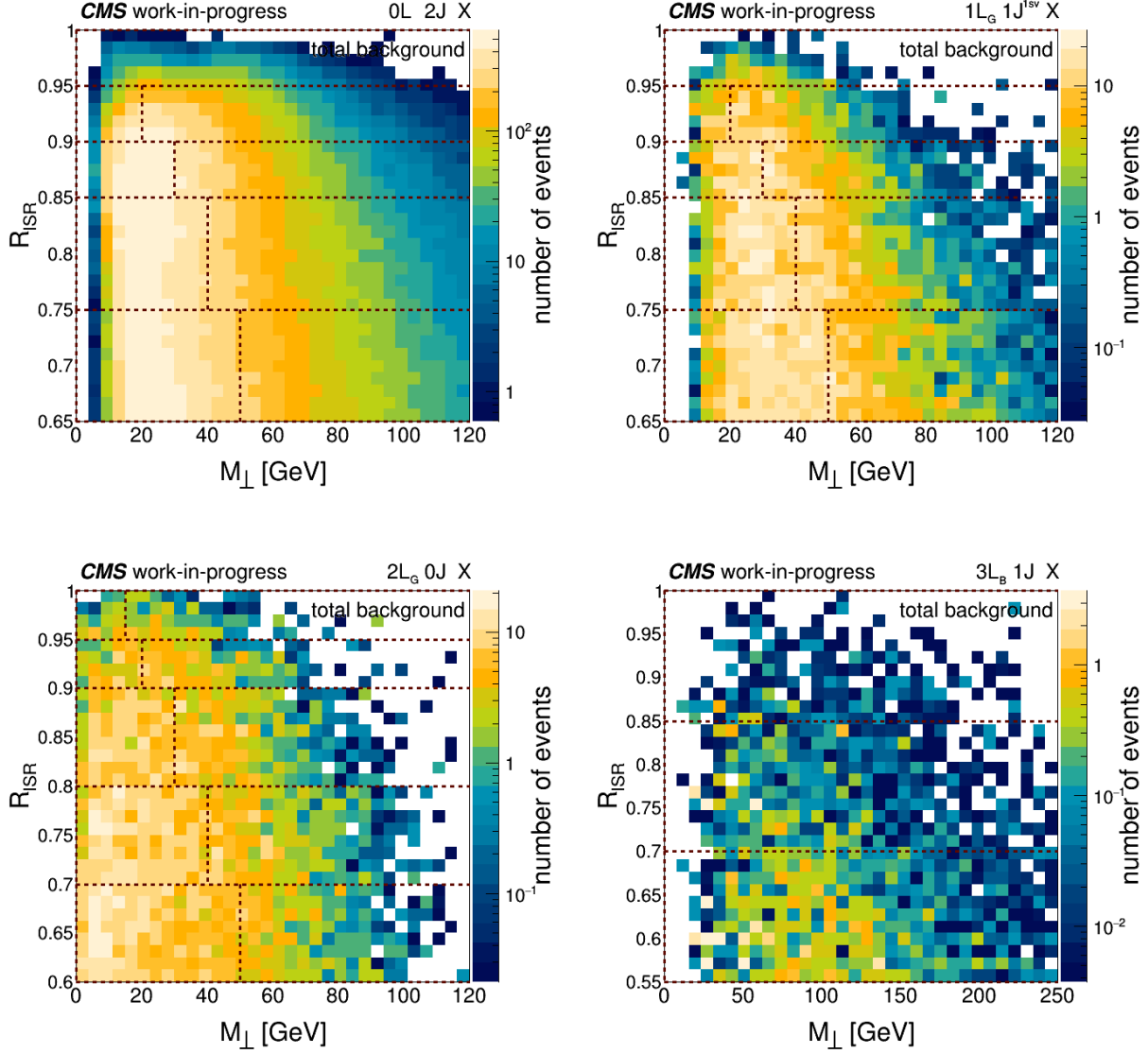


Figure 5.4: The dotted lines show example 2D R_{ISR} and M_{\perp} binning for each lepton multiplicity with the full SM MC background. The bin edges for each figure are based on the contour of the total background and the number of edges reflect the amount of background [1].

In total, there are 392 categories and 3093 total bins, the number of categories contributing to each lepton multiplicity is 84 categories from 0L, 178 categories from 1L, 115 categories from 2L, and 15 categories from 3L. The optimization of all the numerous bins and categories was a large undertaking and was performed using two statistical metrics: the Cousins Z-

Table 5.4: The complete set of R_{ISR} and M_\perp bin edges. A set of 2D bins have been designed for each allowed lepton and jet multiplicity.

-	0L		1L		2L		3L	
N_{jets}^S	R_{ISR}	M_\perp	R_{ISR}	M_\perp	R_{ISR}	M_\perp	R_{ISR}	M_\perp
0	[0.95,0.985]	[≥ 0]	[0.9,0.96]	[≥ 0]	[0.6,0.7]	[0, ≥ 50]	[0.6,0.7]	[≥ 0]
0	[0.985,1]	[0, 5, ≥ 10]	[0.96,0.98]	[0, ≥ 10]	[0.7,0.8]	[0, ≥ 40]	[0.7,0.8]	[≥ 0]
0			[0.98,1]	[0, 5, ≥ 10]	[0.8,0.9]	[0, ≥ 30]	[0.8,0.9]	[≥ 0]
0					[0.9,0.95]	[0, ≥ 20]	[0.9,1]	[≥ 0]
0					[0.95,1]	[0, ≥ 15]		
1	[0.8,0.9]	[≥ 0]	[0.65,0.75]	[0, ≥ 50]	[0.5,0.6]	[0, ≥ 100]	[0.55,0.7]	[≥ 0]
1	[0.9,0.93]	[0, ≥ 20]	[0.75,0.85]	[0, ≥ 40]	[0.6,0.7]	[0, ≥ 80]	[0.7,0.85]	[≥ 0]
1	[0.93,0.96]	[0, ≥ 20]	[0.85,0.9]	[0, ≥ 30]	[0.7,0.8]	[0, ≥ 60]	[0.85,1]	[≥ 0]
1	[0.96,1]	[0, ≥ 15]	[0.9,0.95]	[0, ≥ 20]	[0.8,0.9]	[0, ≥ 40]		
1			[0.95,1]	[≥ 0]	[0.9,1]	[0, ≥ 30]		
2	[0.65,0.75]	[0, ≥ 50]	[0.55,0.65]	[0, ≥ 110]	[0.5,0.65]	[0, ≥ 100]		
2	[0.75,0.85]	[0, ≥ 40]	[0.65,0.75]	[0, ≥ 90]	[0.65,0.75]	[0, ≥ 80]		
2	[0.85,0.9]	[0, ≥ 30]	[0.75,0.85]	[0, ≥ 70]	[0.75,0.85]	[0, ≥ 60]		
2	[0.9,0.95]	[0, ≥ 20]	[0.85,0.9]	[0, ≥ 50]	[0.85,1]	[≥ 0]		
2	[0.95,1]	[≥ 0]	[0.9,1]	[≥ 0]				
3	[0.55,0.65]	[0, ≥ 110]	[0.55,0.65]	[0, ≥ 150]	[0.5,0.65]	[0, ≥ 130]		
3	[0.65,0.75]	[0, ≥ 90]	[0.65,0.75]	[0, ≥ 100]	[0.65,0.8]	[0, ≥ 100]		
3	[0.75,0.85]	[0, ≥ 70]	[0.75,0.85]	[0, ≥ 80]	[0.8,1]	[≥ 0]		
3	[0.85,0.9]	[0, ≥ 50]	[0.85,1]	[≥ 0]				
3	[0.9,1]	[≥ 0]						
4	[0.55,0.65]	[0, ≥ 150]	[0.5,0.6]	[0, ≥ 210]				
4	[0.65,0.75]	[0, ≥ 100]	[0.6,0.7]	[0, ≥ 180]				
4	[0.75,0.85]	[0, ≥ 80]	[0.7,0.8]	[0, ≥ 150]				
4	[0.85,1]	[≥ 0]	[0.8,1]	[≥ 0]				
5	[0.5,0.6]	[0, ≥ 210]						
5	[0.6,0.7]	[0, ≥ 180]						
5	[0.7,0.8]	[0, ≥ 150]						
5	[0.8,1]	[≥ 0]						

binomial method [60] which is a measure of the signal to background significance with a 20% assumption on systematic error, and the median asymptotic limit based on a profile likelihood ratio [61], comparing the signal+background versus background only hypotheses but the observed data is taken as the nearest floor rounded integer from the MC model. Both metrics were tested with the presence of multiple signal types being either, stop, slepton, or electroweakinos. The optimization efforts targeted R_{ISR} , M_\perp , p_T^{ISR} , γ_\perp , the number of bins and bin edges, as well as object counting such as the maximum allowed number of S jets or counted b-jets per lepton multiplicity. The categories and bins were also consolidated to guarantee non-zero expected background events in every bin. The bin by bin statistics for guaranteeing non-zero expected events was studied with MC separately for each year scaled to 138 fb^{-1} as well as with the full Run II combined MC. An example of this study is the flavor consolidation of two lepton categories with $N_{jets}^S > 0$ from the original implementation with flavor separated categories. This consolidation instance was found to have too few events with electrons which led to pathologically good exclusion limits from the empty bins. Similarly 2L $N_{jets}^S \geq 3$ was reduced to $N_{jets}^S \geq 2$ to boost the statistics of high jet multiplicity events in 2L. Example limits comparing many different optimization tests are illustrated in Figure 5.5.

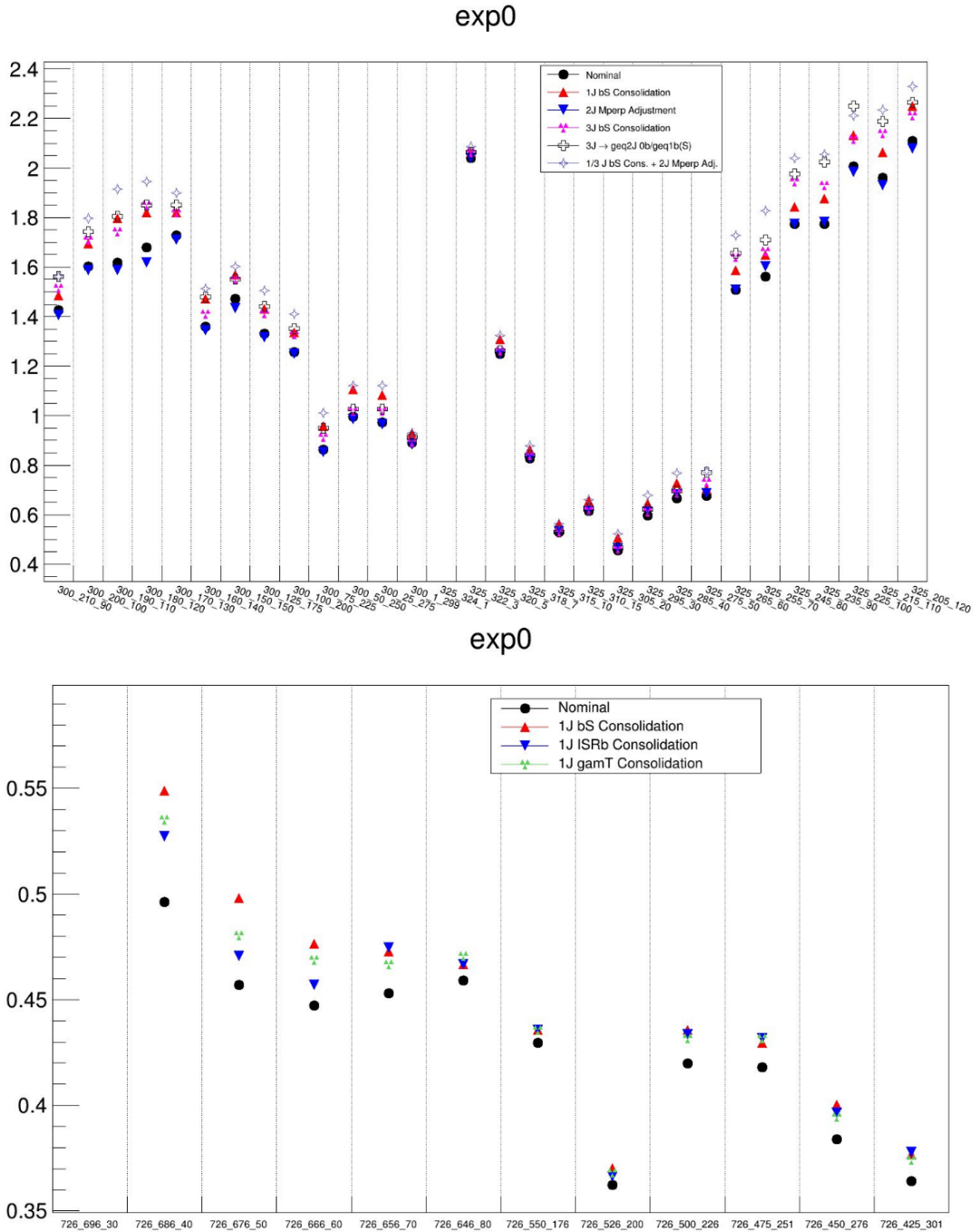


Figure 5.5: Example internal sensitivity optimization plots. The y-axis is the median asymptotic limit with smaller values indicating stronger expected exclusion of the signal grid points on the x-axis. The x-axis label conventions are $m_{NLSP} - m_{LSP}$ ($m_{NLSP} - m_{LSP}$). The top distribution shows tests performed on TChiWZ with bin consolidation and jet multiplicity consolidation. The bottom distribution tests b-tag counting and γ_T bin optimization on T2tt.

Chapter 6

Lepton Selection and Efficiency Measurement

6.1 Lepton Object Definitions

Electrons and muons are selected according to the minimum requirement “VeryLoose” which depends on kinematic and topological quantities in Table 6.1. The electrons use an additional loose requirement, the MVA VLooseFO Id [62]. The set of VeryLoose leptons are further subdivided by quality into three mutually exclusive categories: Gold, Silver, and Bronze. Each category has a measure of three main quantities, the first is the quality of the pre-determined Id. The Id’s differ per flavor and are the standard working points defined by the corresponding physics object group. Id’s range from Loose to Medium to Tight and gain stricter requirements for each tighter requirement. The Loose Id has the highest selection efficiency and misidentification rate while the Tight Id is the least efficient and has the lowest misidentification rate. The muons use the Medium Id [63] and electrons use a more strict selection with the Tight Id [64]. The second quantity is the “promptness” or distance of the lepton production point from the primary vertex. Promptness is measured by the significance of the 3D impact parameter (SIP3D) defined as the impact parameter normalized by its measured error. The impact parameter is the distance of the track’s point of closest approach to the primary vertex. There are three relevant impact parameters, d_{xy} , d_z , and IP_{3D} . The first two parameters: d_{xy} and d_z are the distance in the $x - y$ and $r - z$ planes, respectively. IP_{3D} is the three dimensional distance from the primary vertex to track’s point of closest approach. All three impact parameters are signed based on the same convention.

For a track with direction \hat{t} and distance vector \hat{d} directed from the primary vertex to point of closest approach, the sign of the impact parameter follows $\hat{t} \cdot \hat{d}$. The last component is isolation, a measure of the density of particles in a cone around the lepton. Two similar but complimentary absolute isolations are used: PFIso [65] and MiniIso [66]. Both isolations are an energy sum of neighboring particles inside a cone, but, PFIso has a fixed cone size of $R = 0.4$ cm. PFIso is defined in Equation 6.1 where $p_{T,\text{ch. had}}^{PV}$ is the transverse momentum of tracks associated with the primary vertex that are inside the cone, $E_{T,\text{neut. had}}$ is the transverse energy from energy deposits not associated with tracks that are inside the cone, and $p_{T,\text{ch. had}}^{PU}$ is the transverse momentum of tracks not associated with the primary vertex that are inside the cone. Unlike PFIso, MiniIso uses the same cone-based particle summation strategy, but the cone sizes varies inversely with lepton p_T as shown in Equation 6.2.

$$\sum p_{T,\text{ch. had}}^{PV} + \max(0, \sum E_{T,\text{neut. had}}) - 0.5 * \sum p_{T,\text{ch. had}}^{PU} \quad (6.1)$$

$$R_{\text{miniIso}} = \begin{cases} 0.2 & p_T^\ell < 50\text{GeV} \\ \frac{10}{p_T^\ell} & 50\text{GeV} \leq p_T^\ell \leq 200\text{GeV} \\ 0.05 & p_T^\ell > 200\text{GeV} \end{cases} \quad (6.2)$$

The explicit flavor independent formulas for Gold, Silver, and Bronze can be generalized by the product of three components which are the measured efficiencies of the three previously mentioned quantities. The efficiencies take the form of conditional probabilities to be measured independently in sequence relative to each other:

$$\begin{aligned} \epsilon_{\text{Gold}} &= \epsilon_{\text{ID}} \times \epsilon_{\text{Isolated|ID}} \times \epsilon_{\text{Prompt|}(ID \cap \text{Isolated})} \\ \epsilon_{\text{Silver}} &= \epsilon_{\text{ID}} \times \epsilon_{\text{Isolated|ID}} \times (1 - \epsilon_{\text{Prompt|}(ID \cap \text{Isolated})}) \\ \epsilon_{\text{Bronze}} &= 1 - (\epsilon_{\text{ID}} \times \epsilon_{\text{Isolated|ID}}) \end{aligned} \quad (6.3)$$

The subscript for an efficiency, e.g. $\epsilon_{\text{Prompt} | (\text{ID} \cap \text{Isolated})}$, reads as the efficiency to pass the SIP3D requirement given the lepton passes the Id and Isolation requirements. From equation 6.3 the Gold, Silver, and Bronze efficiencies can be read off as Gold passes all criteria, Silver fails only the SIP3D requirement, and Bronze fails either the Id or isolation and is agnostic to SIP3D. While isolation and vertexing requirements are physically uncorrelated, there is an intersection between the two, meaning a lepton can be both prompt and isolated. This intersection then demands the necessity for conditional efficiencies. The order of the conditional efficiencies is also chosen to minimize the number of measured efficiencies by reusing efficiencies across Gold, Silver, and Bronze.

Table 6.1: The criteria that define the minimum requirements for an accepted lepton. The electron and muon requirements are equivalent in terms of pseudo-rapidity, vertexing, and isolation but vary in p_T threshold and the MVA VLooseFO working point. The MVA VLooseFO ID also varies between years. The parameters d_{xy} and d_z are the transverse and longitudinal impact parameters, respectively.

Criteria	Electron	Muon
p_T	≥ 5 GeV	≥ 3 GeV
$ \eta $	< 2.4	< 2.4
$\text{IP}_{3D}/\sigma_{\text{IP}_{3D}}$	< 8	< 8
$ d_{xy} $	< 0.05 cm	< 0.05 cm
$ d_z $	< 0.1 cm	< 0.1 cm
$\text{PFIso}_{\text{abs}}$	$< 20 + (300/p_T)$ GeV	$< 20 + (300/p_T)$ GeV
MVA VLooseFO ID	✓	—

The advantage of having multiple lepton quality categories allows for robust sensitivity to a wide range of signal processes. This strategy boosts the overall statistics and provides control regions for multiple scenarios. The populations of different truth matched objects per quality are shown in Figure 6.1 and the MC efficiency for Gold, Silver, and Bronze with truth matched objects is shown in Figure 6.2. The Gold region is mainly populated by prompt and isolated leptons that are produced within the primary vertex. This region also coincides with the signature of many targeted electroweakino models. The Silver selection accommodates both leptonically decaying taus, providing an ideal region for stau's, and assists in recovering efficiency of isolated b decays, which, as a consequence provides regions

to cross-constrain $t\bar{t}$ +jets and stop signals. The Bronze selection is rich in fake leptons and provides the best regions to extract fake rates and anchor the fit through a surplus of events.

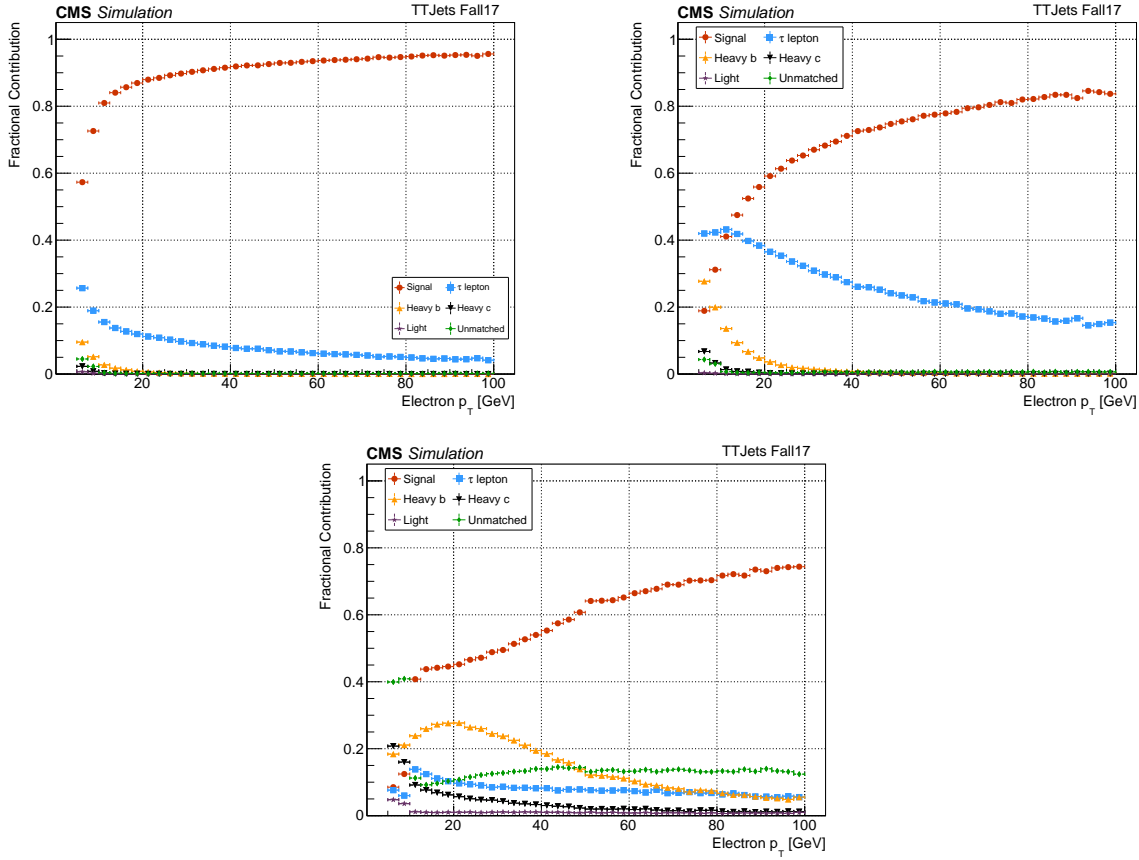


Figure 6.1: Gold (Top-Left), Silver (Top-Right) and Bronze (Bottom) MC truth matching in $t\bar{t}$ sample for 2017. Each figure demonstrates the MC truth composition of each electron quality where a reconstructed electron is ΔR matched to either a signal electron from a prompt W boson decay, a leptonic tau decay, b-quark jet, c-quark jet, or light quark jet [1].

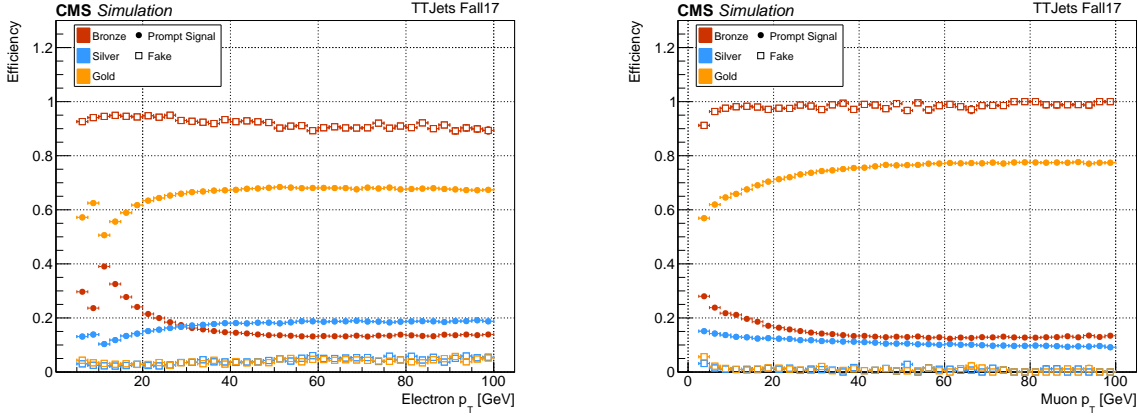


Figure 6.2: Gold, Silver, and Bronze efficiency on truth matched prompt signal leptons from W bosons in $t\bar{t}+j$ ets. The fake efficiencies are also shown for each lepton quality with leptons truth matched to any other source [1].

6.2 Tag-and-Probe Methodology

An important element of a lepton based search is properly modeling the efficiency of selected leptons. A purely Monte-Carlo driven approach is inadequate in perfectly describing nuances in data due to imperfections in modeling. Instead of trying to model exactly all physics and detector effects with simulation, the efficiencies can be directly measured from data by using the Tag-and-Probe method. Then the efficiency ratio between data and MC can be used to multiply the MC as calibration to match data.

The Tag-and-Probe method is used to measure lepton selection criteria by using a well known resonance such as a Z , J/ψ , or Υ and counting the number of probes that pass that criteria. Each counted instance of the Tag-and-Probe consists of two selected leptons. One of the selected leptons is the tag and the other is the probe. The tag passes the tight selection requirement to give high confidence that it isn't a fake lepton. Fake leptons fall into two possible categories: reducible and irreducible. A reducible fake lepton is a particle that fakes the signature of a lepton such as a charged pion. An irreducible fake lepton is an actual lepton which coincidentally passes some selection criteria but is not the leptons of interest from the primary vertex e.g. an isolated muon from a jet accompanying a leptonic

Z decay. The second lepton in the Tag-and-Probe is the probe. The probe is subjected to the selection criteria whose efficiency is being measured. The invariant mass of the pair of leptons is calculated and required to fall within a defined range around the resonance. A particular event may have multiple lepton pairs but the tag and the probe are not allowed to switch positions and be counted twice, as double counting would lead to a bias in the efficiency measurement [67]. To avoid bias, the tag and probe are required to be the opposite charge and same flavor where the tag is randomly selected. If multiple same flavor lepton pairs occur in single event i.e. there are multiple probes to a single tag, the treatment for selecting the pairs differs between electrons and muons. There is no specific study which led to justifying the differing arbitration approaches in flavors, only that the choice reflects the default choices implemented in the existing code bases. For muons, no arbitration is used, all pairs are utilized which means an additional pair not truly from the resonance will then contribute as combinatorial background in a single event. For electrons, only a single probe is selected per event which has the highest p_T . The selected probes can either pass or fail their selection which leads to the formation of three distributions, one with a passing probe, one with a failing probe, and one with all probes. An example of all three distributions is shown in Figure 6.3. The probability of observing k passing probes in n Tag-and-Probe pair trials is dependent on the selection efficiency ε and can be expressed as a likelihood from the binomial probability density $P(k|\varepsilon, n) = \binom{n}{k} \varepsilon^k (1 - \varepsilon)^{n-k}$. The MLE estimator for efficiency is then the fraction of passing probes to the total number of pairs, or $\varepsilon = k/n$. Technical documentation for the Tag-and-Probe in CMS is scarce, but, an early strategy for fitting efficiency is defined in [68]. The legacy code base as of `CMSSW_10_6_X` uses a binned maximum likelihood between the observed passing probes and failing probes where the efficiency extracted is an explicit fit parameter. The two simultaneously fit functions are:

$$N^{\text{Pass}} = N_{\text{Total}}(\varepsilon \cdot f_{\text{All}}^{\text{sig}}) + \varepsilon_{\text{bkg}} \cdot (1 - f_{\text{All}}^{\text{sig}}) \quad (6.4)$$

$$N^{\text{Fail}} = N_{\text{Total}}((1 - \varepsilon) \cdot f_{\text{All}}^{\text{sig}} + (1 - \varepsilon_{\text{bkg}}) \cdot (1 - f_{\text{All}}^{\text{sig}})) \quad (6.5)$$

$N^{\text{Pass/Fail}}$ is the total number of observed probes that either pass or fail the selection criteria while N_{Total} is the total number of Tag-and-Probe pairs. The binomial estimator for efficiency, ε , enters the fit functions as the first term but is accompanied by a second term that describes the background contribution with its own efficiency ε_{bkg} . The term $f_{\text{All}}^{\text{sig}}$ is the fraction of background subtracted signal events over the allowed dilepton mass range. $f_{\text{All}}^{\text{sig}}$ depends on the defined signal and background pdfs. The nominal pdfs chosen for reported fits use a 5 parameter Voigtian+Voigtian signal model which shares a common mean but uses independent width parameters, in conjunction with an Exponential background model.

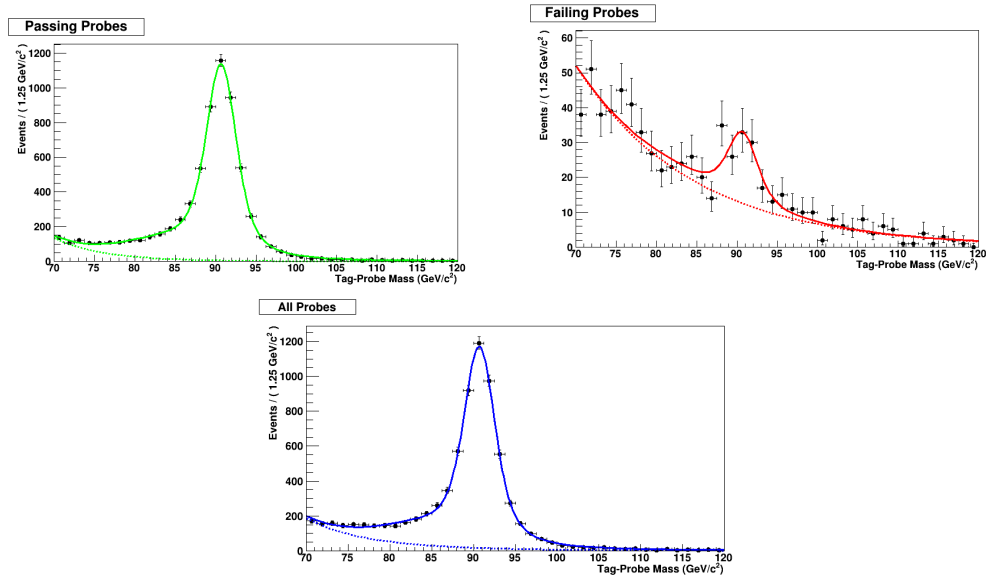


Figure 6.3: Example Tag-and-Probe Z di-muon fits for passing,failing, and all probes with the Medium Id, $|\eta| < 1.2$, and $p_T < 20$ GeV

6.3 The Electron Tag-and-Probe

The electron Tag-and-Probe is performed with the Z resonance over a range of bins divided by p_T and η , where the selected binnings follow the p_T and η binning conventions from the electron physics object group and are $p_T \in [5, 10, 20, 30, 40, 70, 100]$ and $|\eta| \in [0, 0.6, 1.4, 2.4]$. A centrally curated CMSSW PhysicsTools in `CMSSW_10_2_X` package is used to perfrom the Tag-and Probe. The software pipeline consists of two steps, an ntuplizing stage from

Table 6.2: Data and MC samples for each year used by the electron Tag-and-Probe.

Type	Year	Sample Name
Data	2016	/SingleElectron/Run2016-17Jul2018_ver2-v1/MINIAOD
Data	2017	/SingleElectron/Run2017-31Mar2018-v1/MINIAOD
Data	2018	/EGamma/Run2018-17Sep2018-v2/MINIAOD
MC	2016	/DYJetsToLL_M-50_TuneCUETP8M1_13TeV-madgraphMLM-pythia8 /RunIISummer16MiniAODv3-PUMoriond17_94X_mcRun2_asymptotic_v3_ext2-v2/MINIAODSIM
MC	2017	/DYJetsToLL_M-50_TuneCP5_13TeV-madgraphMLM-pythia8 /RunIIFall17MiniAODv2-PU2017RECOv1_step_12Apr2018_94X_mc2017_realistic_v14_ext1-v1/MINIAODSIM
MC	2018	/DYJetsToLL_M-50_TuneCP5_13TeV-madgraphMLM-pythia8 /RunIIAutumn18MiniAOD-102X_upgrade2018_realistic_v15-v1/MINIAODSIM

processing data in the MiniAOD format [69], and a fitting stage. The Ntupleizing stage selects Tag-and-Probe pairs along with all potential variables of interest and loads them onto an ntuple using `TnPTreeProducer` [70]. Samples used in the Ntupleizing stage are listed in Table 6.2. In the fitting stage, a random subset of TnP pairs are sampled with `TnPTreeAnalyzer` [71]. The analyzer performs all of the fitting and efficiency measurements according to the specified selection criteria.

A general selection is applied for electron TnP candidates that differs between the tag and probe, but both depend on super cluster (SC) kinematics. The super clusters are expected to fall within the calorimeter acceptance which includes vetoing super clusters in the end-cap gaps. The invariant mass of the electron of the pair also is required to fall within a specified Z-window. The selection specifics are listed in Table 6.3. The tag is also required to pass a trigger requirement to reflect the inherit trigger bias which is not applied in simulation by default. The triggers selected are HLT electron collections and are grouped by specific paths and filters. The tag electrons are matched to trigger objects in the path/filter combination and passed based on the OR of triggers in the collection. The chosen trigger combinations are `HLT_Ele27_eta2p1_WPTight_Gsf_v*`, `HLT_Ele32_WPTight_Gsf_L1DoubleEG_v*`, `HLT_Ele32_WPTight_Gsf_v*` for 2016 through 2018, respectively.

The measurements of the Gold, Silver, and Bronze efficiencies components, and VeryLoose, are shown in Figure 6.4. The relative efficiencies per component range from approximately 75% to 95% with a slight dependence on $|\eta|$. The largest combined systematic and statistical

Table 6.3: Kinematic requirements for the electron Tag-and-Probe components.

Tag-and-Probe Electron Candidate Selection Criteria			
Tag	Probe	Super Cluster	Pair
$ \eta_{SC} \leq 2.1$ veto $1.4442 \leq \eta_{SC} \leq 1.566$ $p_T \geq 30.0 \text{ GeV}$ Passes Tight Id	$ \eta_{SC} \leq 2.5$ $E_{ECAL} \sin(\theta_{SC}) > 5.0 \text{ GeV}$	$ \eta < 2.5$ $E_T > 5.0 \text{ GeV}$	$m_{ee} > 50 \text{ GeV}$ $m_{ee} < 130 \text{ GeV}$

errors are $O(4\%)$ and occur in data with the lowest p_T bins. The data and MC agreement is within a few percent for both the Id, Isolation, and SIP3D. The efficiency components combined into Gold, Silver, and Bronze are shown in Figure 6.5. The range of efficiencies for each quality ranking are $(50 - 70)\%$, $(10 - 20)\%$, and $(10 - 30)\%$ for Gold, Silver, and Bronze respectively. The Gold, Silver, and Bronze data to MC ranges around a few percent, but large discrepancies from the data to MC ratio can be seen, at the highest and lowest p_T bins. More granular Id measurements could be obtained by using a different resonance such as $J/\psi \rightarrow ee$ for the lower p_T ranges, however, data triggers with electrons for J/ψ are not available.

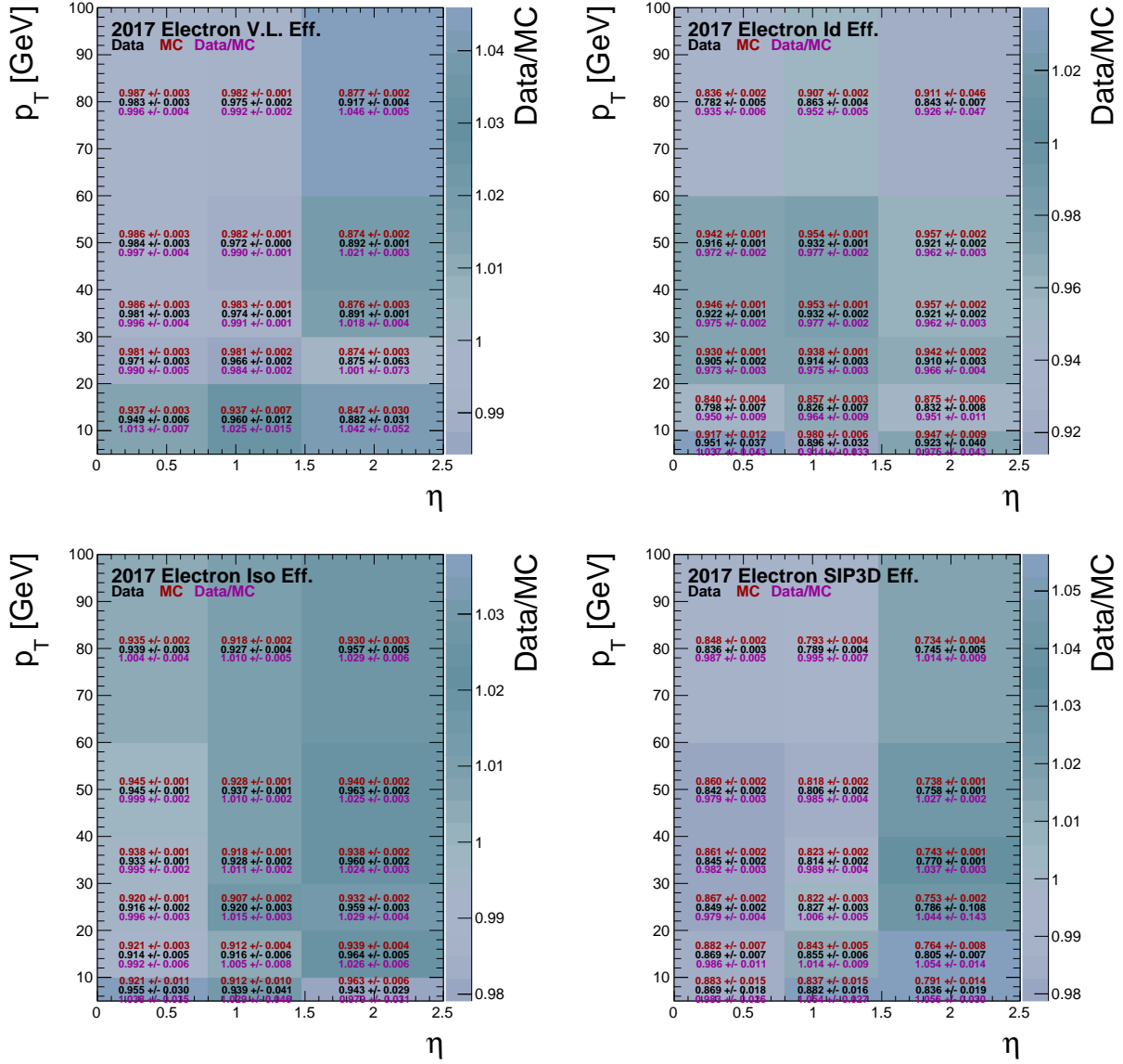


Figure 6.4: The 2017 individually measured electron efficiencies for Very Loose, ID, Isolation, and Impact parameter in bins of p_T and $|\eta|$.

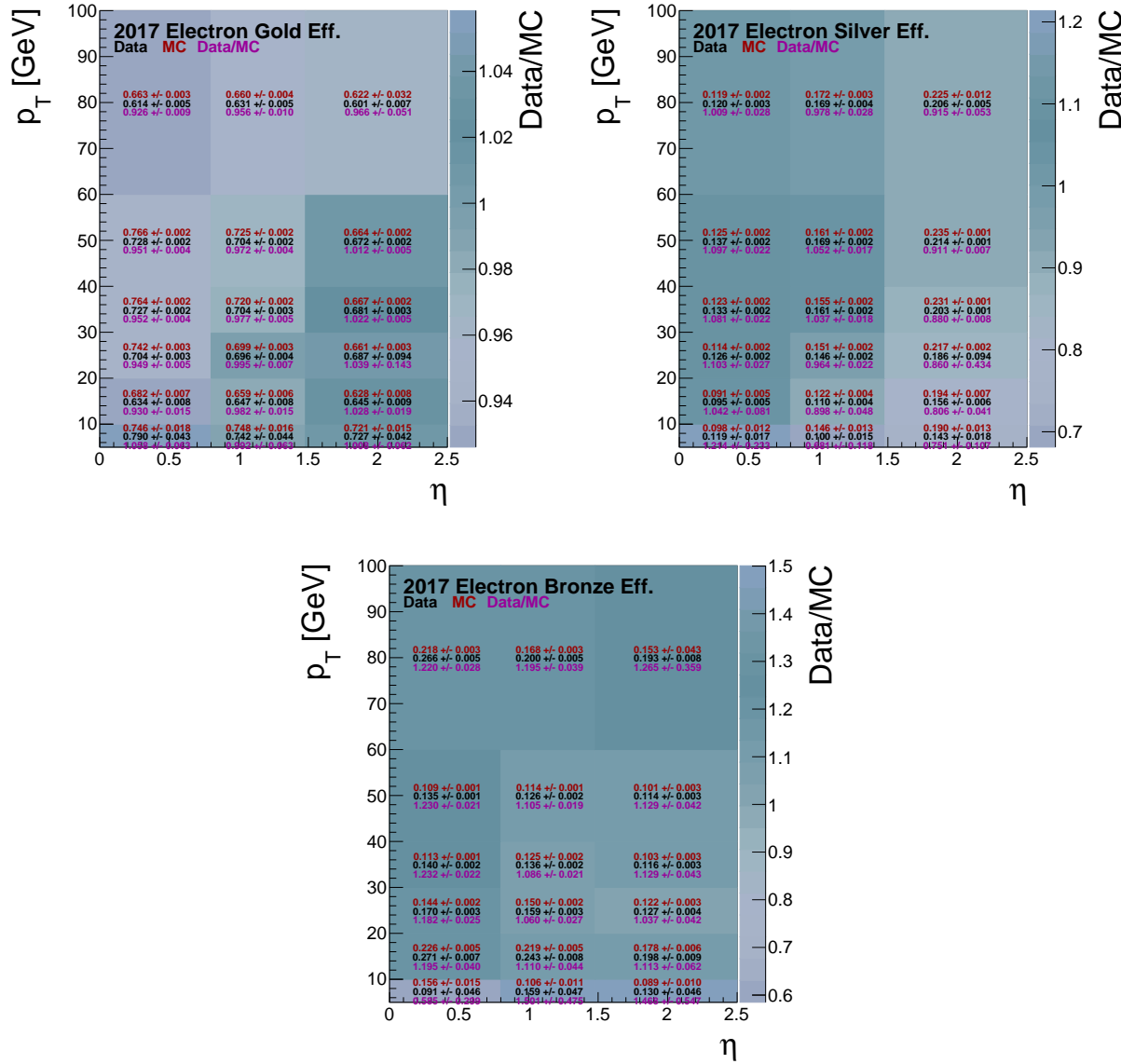


Figure 6.5: The 2017 combined electron efficiencies for Gold, Silver, and Bronze.

6.4 The Muon Tag-and-Probe

The muon Tag-and-Probe tools also use the same centrally curated CMSSW PhysicsTools in `CMSSW_10_6_X`. The software pipeline is identical to electrons in that it consists of an miniAOD [69] ntuplizing [72] and fitting [73] stage. Both code bases for muons and electrons are separate but functionally identical. The samples chosen for Z measurements are shown in Table 6.4. J/ψ ntuples are available from a central repository of standard Tag-and-Probe selection variables which use the pre-ultra legacy samples for each year [74] and are used for low p_T Id efficiency measurement. Muon Tag-and-Probe efficiencies are measured above 20 GeV using the Z boson and below 20 GeV with the J/ψ meson. The η bins are divided into central and forward regions around the end-caps at $|\eta| = 2.1$. In total there are three sets of binnings: The low p_T J/ψ binning, J/ψ^L for muon Id below 20 GeV, the high p_T Z binning, Z^H above 20 GeV, and the low p_T Z binning, Z^L , used to extrapolate isolation and impact parameter efficiencies down to 3 GeV. The explicit bin edges for each range are defined in Table 6.6.

Isolation and impact parameters are unable to be measured using the J/ψ . About 30% of prompt J/ψ are produced from χ_c and $\Psi(2S)$ inside a jet and likely will be unisolated [75]. Similarly, another 10% of all J/ψ are produced within b-jets, which lead to non-prompt unisolated events [76].

The criteria for the tag or probe vary between Z and J/ψ but are identical across the two Z ranges. The selections follow the standard criteria defined from the centrally produced

Table 6.4: Data and MC samples for each year used by the electron Tag-and-Probe.

Type	Year	Sample Name
Data	2016	<code>/SingleMuon/Run2016-17Jul2018-v1/MINIAOD</code>
Data	2017	<code>/SingleMuon/Run2017-31Mar2018-v1/MINIAOD</code>
Data	2018	<code>/SingleMuon/Run2018-17Sep2018-v2/MINIAOD</code>
MC	2016	<code>/DYJetsToLL_M-50_TuneCUETP8M1_13TeV-madgraphMLM-pythia8</code> <code>/RunIISummer16MiniAODv3-PUMoriond17_94X_mcRun2_asymptotic_v3_ext2-v2/MINIAODSIM</code>
MC	2017	<code>/DYJetsToLL_M-50_TuneCP5_13TeV-madgraphMLM-pythia8/</code> <code>RunIIFall17MiniAODv2-PU2017RECOsimStep_12Apr2018_94X_mc2017_realistic_v14_ext1-v1/MINIAODSIM</code>
MC	2018	<code>/DYJetsToLL_M-50_TuneCP5_13TeV-madgraphMLM-pythia8/</code> <code>RunIIAutumn18MiniAOD-102X_upgrade2018_realistic_v15-v1/MINIAODSIM</code>

Table 6.5: Names of centrally produced J/ψ Tag-and-Probe trees.

Type	Year	Sample Name
Data	2016	TnPTreeJPsi_LegacyRereco07Aug17_Charmonium_Run2016Bver2_GoldenJSON.root
Data	2017	TnPTreeJPsi_17Nov2017_Charmonium_Run2017Cv1_Full_GoldenJSON.root
Data	2018	TnPTreeJPsi_Charmonium_Run2018Dv2_GoldenJSON.root
MC	2016	TnPTreeJPsi_80X_JpsiToMuMu_JpsiPt8_Pythia8.root
MC	2017	TnPTreeJPsi_94X_JpsiToMuMu_Pythia8.root
MC	2018	TnPTreeJPsi_102XAutumn18_JpsiToMuMu_JpsiPt8_Pythia8.root

Table 6.6: Muon bin edges for the J/ψ case, high p_T Z case, and low p_T fitting case Z^L .

Range	Muon Binning	
	p_T GeV	$ \eta $
J/ψ^L	[3.0, 4.0, 5.0, 6.0, 7.0, 9.0, 14.0, 20.0]	[0, 1.2, 2.4]
Z^H	[10, 20, 30, 40, 60, 100]	[0, 1.2, 2.4]
Z^L	[6,8,10,14,18,22,28,32,38,44,50]	[0, 1.2, 2.4]

muon Tag-and-Probe efficiencies and are described in Table 6.7.

The muon data also has an implicit selection due to triggering. To reflect the trigger bias in MC, the tag is required to pass a chosen trigger in the efficiency denominator in addition to HLT object matching. The triggers available vary from year to year for Z using `IsoTkMu22` in 2016 and `isoMu24eta2p1` in 2017 and 2018. J/ψ uses the same trigger for all years, which is `Mu7p5Tk2`.

The Gold, Silver, and Bronze efficiency definitions use the same bin ranges J/ψ^L , Z^L , and Z^H shown in Table 6.6. The explicit form for Gold Silver and Bronze based on p_T range and as a function of conditional efficiency components of ID, Isolation, and SIP3D are shown in table 6.8. The low p_T muons include the Id measured by J/ψ as well as the extrapolated

Table 6.7: Kinematic requirements for the muon Tag-and-Probe components.

Tag-and-Probe Muon Candidate Selection Criteria		
Tag	Probe	Pair
passes tightID $\sum p_T^{ch}/p_T < 0.2$ $p_T > 15$ GeV	No requirement	$m_{\mu\mu} > 60$ GeV $ z_{\mu_1} - z_{\mu_2} < 4$ cm

Table 6.8: The formulation of Gold, Silver, and Bronze efficiencies as a function of conditional Tag-and-Probe efficiency components.

$$p_T \in [3, 20)$$

$$\begin{aligned}\epsilon_{\text{Gold}} &= \epsilon_{\text{ID}}^{J/\psi} \times \epsilon_{\text{Isolated}|\text{ID}}^{Z_L} \times \epsilon_{\text{Prompt}|(\text{ID} \cap \text{Isolated})}^{Z_L} \\ \epsilon_{\text{Silver}} &= \epsilon_{\text{ID}}^{J/\psi} \times \epsilon_{\text{Isolated}|\text{ID}}^{Z_L} \times (1 - \epsilon_{\text{Prompt}|(\text{ID} \cap \text{Isolated})}^{Z_L}) \\ \epsilon_{\text{Bronze}} &= 1 - (\epsilon_{\text{ID}}^{J/\psi} \times \epsilon_{\text{Isolated}|\text{ID}}^{Z_L})\end{aligned}\quad (6.6)$$

$$p_T \in [20, 100]$$

$$\begin{aligned}\epsilon_{\text{Gold}} &= \epsilon_{\text{ID}}^{Z_H} \times \epsilon_{\text{Isolated}|\text{ID}}^{Z_H} \times \epsilon_{\text{Prompt}|(\text{ID} \cap \text{Isolated})}^{Z_H} \\ \epsilon_{\text{Silver}} &= \epsilon_{\text{ID}}^{Z_H} \times \epsilon_{\text{Isolated}|\text{ID}}^{Z_H} \times (1 - \epsilon_{\text{Prompt}|(\text{ID} \cap \text{Isolated})}^{Z_H}) \\ \epsilon_{\text{Bronze}} &= 1 - (\epsilon_{\text{ID}}^{Z_H} \times \epsilon_{\text{Isolated}|\text{ID}}^{Z_H})\end{aligned}\quad (6.7)$$

efficiencies from SIP3D and isolation fits in Z_L . The high p_T muons are composed of all the factors directly measured in Z_H .

The 2017 efficiencies for Id, Isolation, SIP3D, and VeryLoose are shown in Figure 6.6. The efficiencies for the other years are nearly identical. The overlapping bins of efficiency between J/ψ and Z do not all match within statistical uncertainties. However, the average deviation of the efficiency central values are 0.2% for MC and 1% for data. The relative efficiencies per component range from approximately 88% to 98% and are fairly uniform between the barrel and end-caps. The efficiencies for the isolation ranges from (90 – 95)% where the end-caps generally are about 5% more efficient. As for SIP3D, the efficiency ranges from about (80 – 93)% with another 5% $|\eta|$ based efficiency gap, however, in the SIP3D case, the barrel is more efficient as opposed to isolation. The extrapolation of the vertexing and isolation efficiencies below 20 GeV is done by fitting a quadratic polynomial to the efficiencies on the Z_L interval. Both data and MC are shown in Figure 6.7. The errors for each bin are the combined statistical and systematic errors from Table 6.10 and are adjusted before the polynomial fit. Any efficiencies below 20 GeV are then reported from the fit model. The fit errors are the 68% confidence interval combined with the systematic errors. The worst

observed right tail P-value from all fits is $\approx 2\%$, the median P-value from the Figure 6.7 is 84%. The fits in each year behave qualitatively the same as 2017. The product of the efficiency components into their corresponding Gold, Silver, and Bronze category is shown in Figure 6.8. The range of efficiencies for each quality ranking are $(70 - 80)\%$, $(5 - 15)\%$, and $(4 - 20)\%$ for Gold, Silver, and Bronze, respectively. The Data and MC agreement for all three ranks is better than electrons with the largest discrepancy in Gold being 2% and the average deviation in Silver and Bronze begin approximately $(5 - 10)\%$.

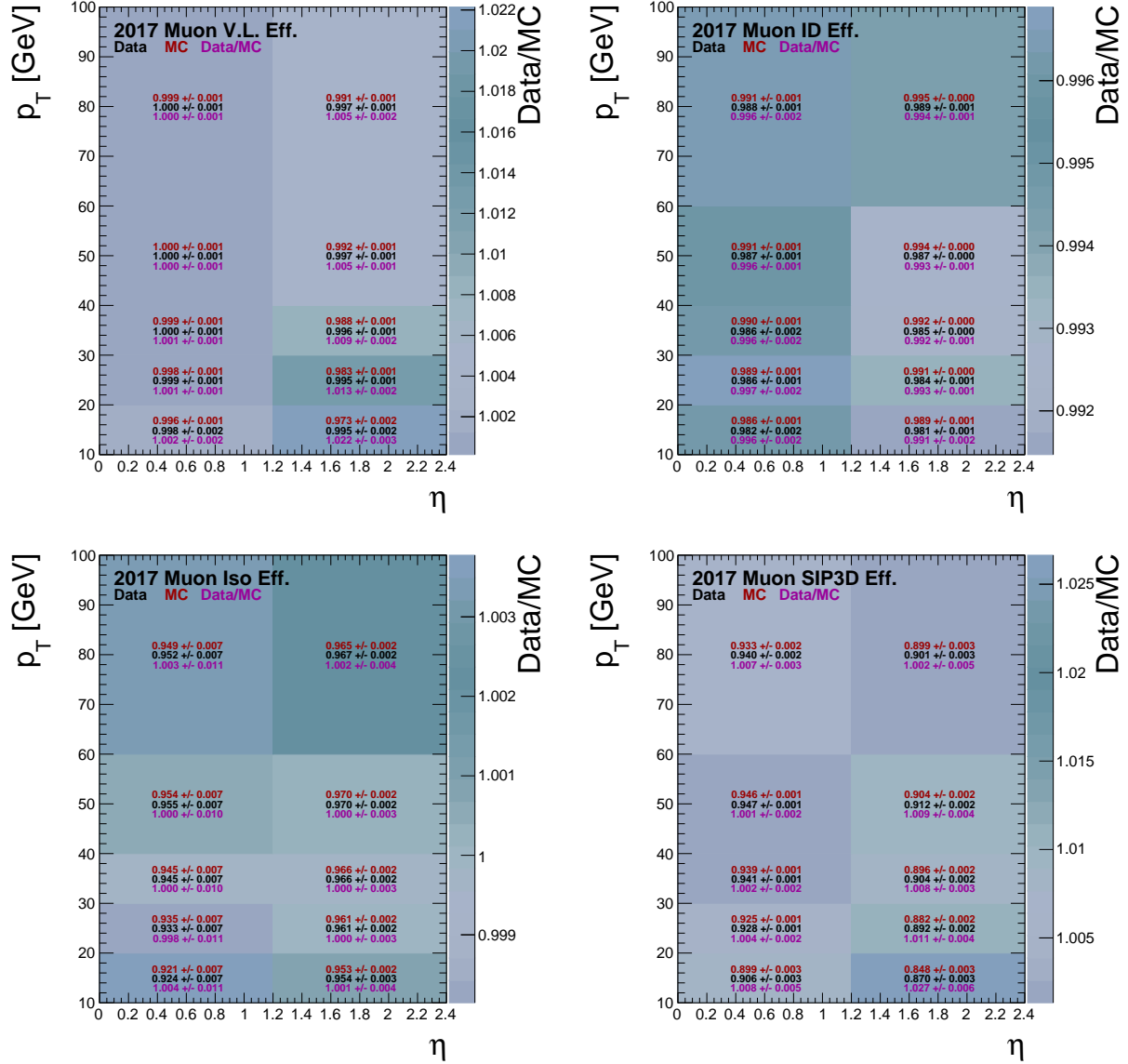


Figure 6.6: Tag-and-Probe efficiencies for the muon Very Loose, Id, Isolation, and SIP3D in 2017. The $p_T < 20$ GeV isolation bins incorporate the efficiency shape fit from Figure 6.7 to extrapolate isolation and SIP3D to low p_T . The Id $p_T < 20$ GeV bins include the J/ψ contribution below 20 GeV. Low p_T binning does not reflect actual bin granularity, bins are merged for readability.

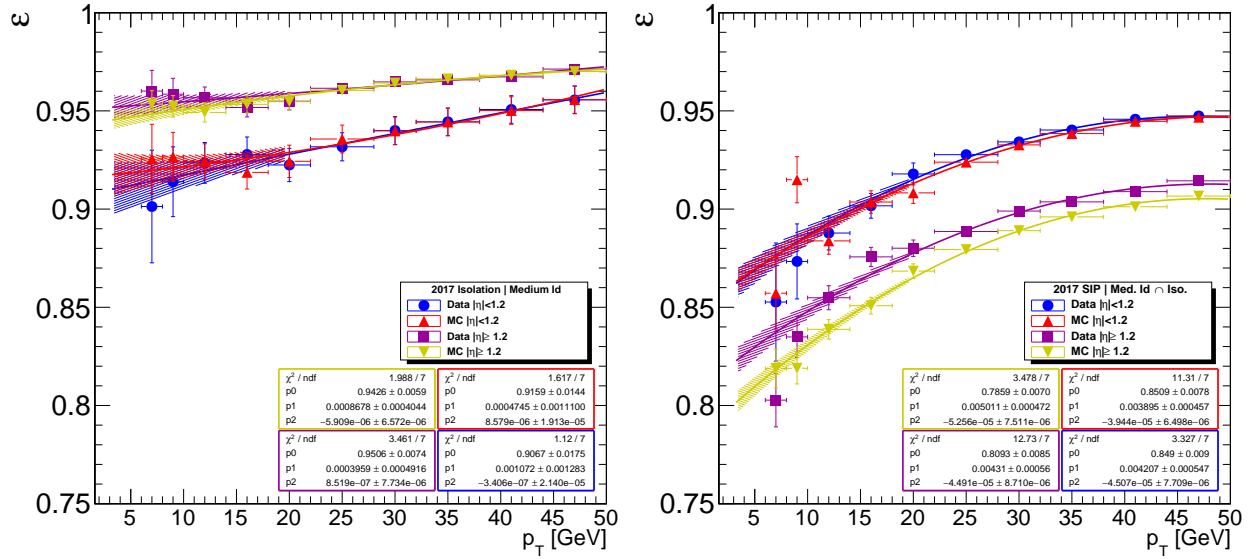


Figure 6.7: The fitted muon isolation and SIP3D efficiencies for 2017. Both distributions compare data and MC separated between barrel and end-cap.

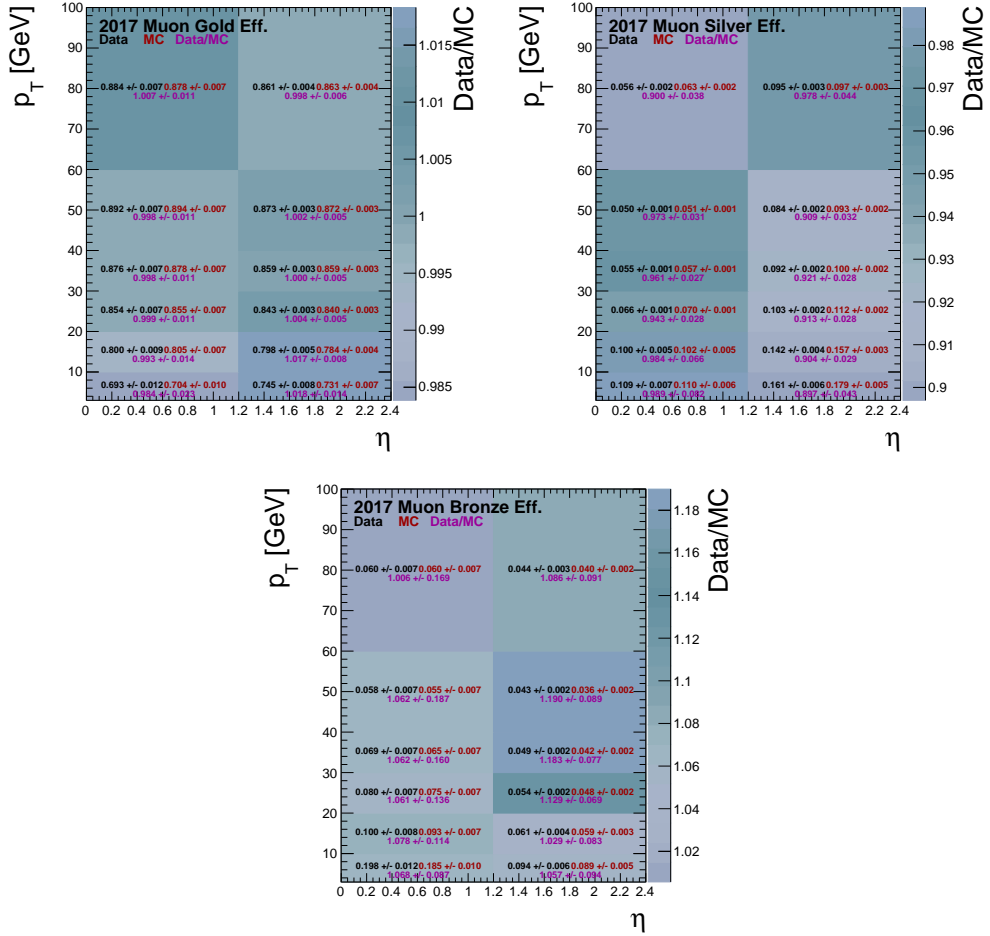


Figure 6.8: The combined efficiency components from equations 6.6 and 6.7 and Very Loose for 2017. The low- p_T region (< 20 GeV) includes the contributions from J/ψ as well as the isolation and SIP3D extrapolations. Propagated errors are treated as uncorrelated.

6.5 Lepton Systematics and Scale Factors

The systematic errors for the electron and muon efficiencies are derived by varying the Tag-and-Probe signal and background models: shifting the mass window, increasing and decreasing the number of bins used in the fit, varying the selection on the tag, and testing MC samples with different generators. The systematic error is defined as the maximum spread in efficiencies between the efficiency variations with an example spread shown in Figure 6.10. Rather than compute the systematic error for every bin, similarities between neighboring bins motivates using a simplified bin approach which was chosen qualitatively by the background shape. The shape of the p_T based mass distributions is illustrated in Figure 6.9. The same η bins are utilized according to lepton flavor, but the p_T bins are consolidated into a high and low bin pivoting on 20 GeV. A high and low systematic is derived for each selection criteria per flavor per year and is applied to the efficiencies that fall within the corresponding p_T and η range for modeling shape systematics. The tag systematics are computed by varying the p_T requirement on the tag and are found to be $< 1\%$. The MC systematics are computed by comparing ZDY MC sample with Z p_T ranging between 100-250 GeV against an inclusive sample and are found to be about 1%.

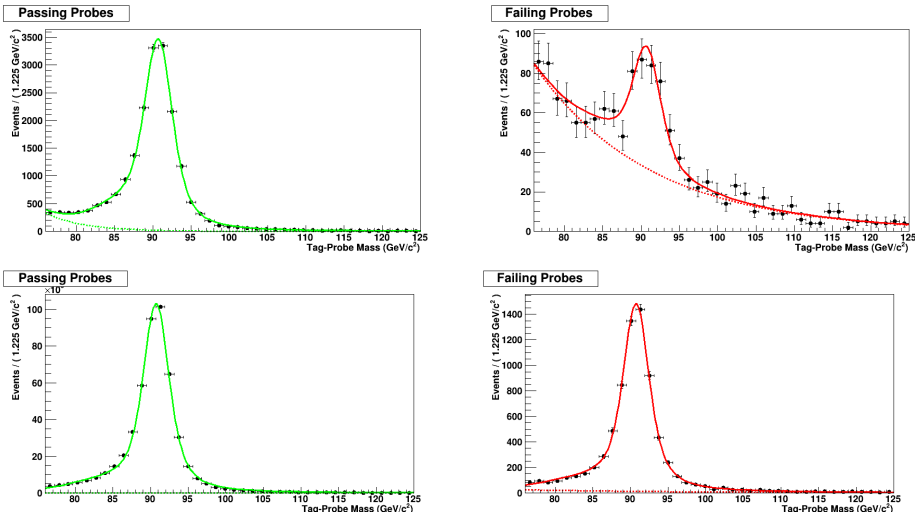


Figure 6.9: Tag-and-Probe di-muon mass distributions for both passing and failing probes. The top set of plots consist of probes below 20 GeV and the bottom set are above 20 GeV.

Scale factors are derived bin by bin for each criteria per flavor per year by finding the ratio of efficiencies in data to Monte Carlo. The scale factor error is propagated by combining both the statistical error from the Tag-and-Probe in quadrature with the systematic error. The 2017 shape modeling systematics for electrons and muons is shown in Table 6.9 and Table 6.10 and is nearly identical to the systematics derived in the other years. Additional scale factors are also needed to adjust the differences between samples which are either created with a full simulation or fast simulation. The fast to full factor is obtained by extracting the efficiency ratio between full and fast sim $t\bar{t}$ MC.

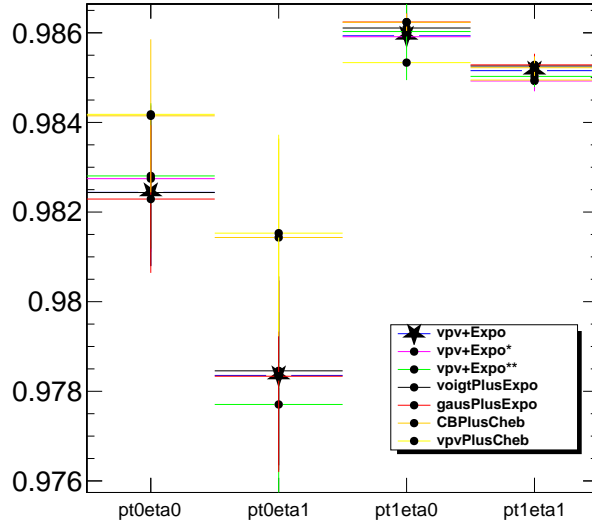


Figure 6.10: Example systematic spread from various fit models and binnings for muons. Includes the four combinations of regions either low or high p_T and central and forward $|\eta|$. The starred points are the nominal pdfs, the ‘*’ points use nominal pdfs with variations on the number of fit bins and fit window. The other points use the nominal number of fit bins and window with different signal models such as: Voigtian, Gaussian, Crystalball or a Chebyshev background model.

Table 6.9: The electron modeling systematic absolute error derived from the Tag-and-Probe for 2017 data and split into p_T and $|\eta|$ regions.

ID	$0 \leq \eta < 0.8$	$0.8 \leq \eta < 1.479$	$ \eta \geq 1.479$
$p_T < 20$ [GeV]	0.003	0.001	0.005
$p_T \geq 20$ [GeV]	0.001	0.001	0.002
Iso ID			
$p_T < 20$ [GeV]	0.002	0.003	0.003
$p_T \geq 20$ [GeV]	0.001	0.001	0.002
SIP Iso \cap ID			
$p_T < 20$ [GeV]	0.006	0.004	0.007
$p_T \geq 20$ [GeV]	0.002	0.002	0.0006
VeryLoose			
$p_T < 20$ [GeV]	0.002	0.007	0.03
$p_T \geq 20$ [GeV]	0.003	0.0001	0.0007

Table 6.10: The muon modeling systematic absolute error derived from the Tag-and-Probe data and split into p_T and $|\eta|$ regions.

ID	$ \eta < 1.2$	$ \eta \geq 1.2$
$p_T < 20$ [GeV](J)	0.001	0.001
$p_T \geq 20$ [GeV](Z)	0.001	0.0003
Iso ID		
$p_T < 20$ [GeV]	0.007	0.004
$p_T \geq 20$ [GeV]	0.007	0.002
SIP Iso \cap ID		
$p_T < 20$ [GeV]	0.005	0.003
$p_T \geq 20$ [GeV]	0.001	0.002
Very Loose		
$p_T < 20$ [GeV]	0.001	0.0003
$p_T \geq 20$ [GeV]	0.001	0.001

Chapter 7

Data Driven Fit and Fit Evaluation

7.1 Introduction

This analysis is a counting experiment that is evaluated with a Poisson likelihood. The MC model is designed to be data-driven. Background dominates the majority of regions, and the data is used to adjust the MC model to the data in the fit. The anchoring provided by background-rich regions translates into well-constrained background predictions in sensitive regions with an ABCD-like approach [77]. To obtain a robust MC model before unblinding, three regions are defined: the Control Region (CR) which has no signal; a Validation Region (VR) which has mild sensitivity and tests the modeling in regions untouched by the CR; and the Signal Region (SR), which is comprised of the high R_{ISR} bins and is sensitive to all signals. The fits are conducted in three stages, starting with the CR only, then CR+VR, and finally the full fit combining all three fit regions CR+VR+SR.

7.2 Fit Strategy and Fit Region Definitions

The fits are carried out in three stages combining the Control Region, Validation Region, and Signal Region. The control region is designed to have negligible signal sensitivity and covers the majority of bins. The expected signal contamination in the control region from stops, sleptons, or electroweakinos is < 1% for sparticle masses that are not excluded. The categories and bins that compose the CR are the low R_{ISR} region, more specifically the lowest two R_{ISR} bins of almost every category. The only category that has been specifically

excluded from the CR is 2L high p_T^{ISR} categories. The high p_T^{ISR} is very sensitive to stop processes and electroweakinos. The CR region is comprised of 1298 bins which hold 72% of the total expected Run II events. This means that the CR dominates the behavior of the fit, but does not guarantee satisfactory modeling at high R_{ISR} . To deal with this shortcoming, we introduce the Validation Region. This region is combined with the CR and extends the fit sampling all categories and kinematic ranges. The VR is composed of the remaining bronze category R_{ISR} distributions not covered by the CR. The signal presence in VR bins is at the few percent level with signals showing up in the most sensitive categories, like $\mu\mu$. Together the CR+VR fit covers 1517 total bins increasing the expected number of events seen by the fit 10%. The remaining region is the SR, it has 1576 total bins, but only 19% of total expected events. The sensitivity to every signal is high in this region, with examples of the S/B significance using the Z-binomial statistic [60] shown in Figures 7.1 and 7.2.

7.3 Fit Implementation and Model Definition

The fitting framework is provided by the CMS `HiggsCombine` tool which generates datacards that encode all the components of the fit into a standard format, which is then processed by the CMS `CombineHarvester` and `RooFit/RooStats` packages [78][79]. The fit can be represented by a Poisson likelihood defined as:

$$\mathcal{L}(\vec{\alpha}|\vec{n}) = \left[\prod_i^N \text{Pois}(n_i|\lambda_i(\vec{\alpha})) \right] \left[\prod_j^M \pi_j(\alpha_j) \right]. \quad (7.1)$$

Equation 7.1 extends over the range of all N analysis bins where each i -th bin is composed of a count of observed events n_i and expected events λ_i . The expected events are subject to the set of nuisance parameters $\vec{\alpha}$, of which some are conditioned by prior probability distributions $\pi_j(\alpha_j)$. The best fit model for $\lambda(\vec{\alpha})$ is found by maximizing the likelihood with the minimal set of nuisance parameters $\vec{\alpha}$ that is sensitive to the signal+background or background only hypothesis. There are three types of nuisance parameters implemented

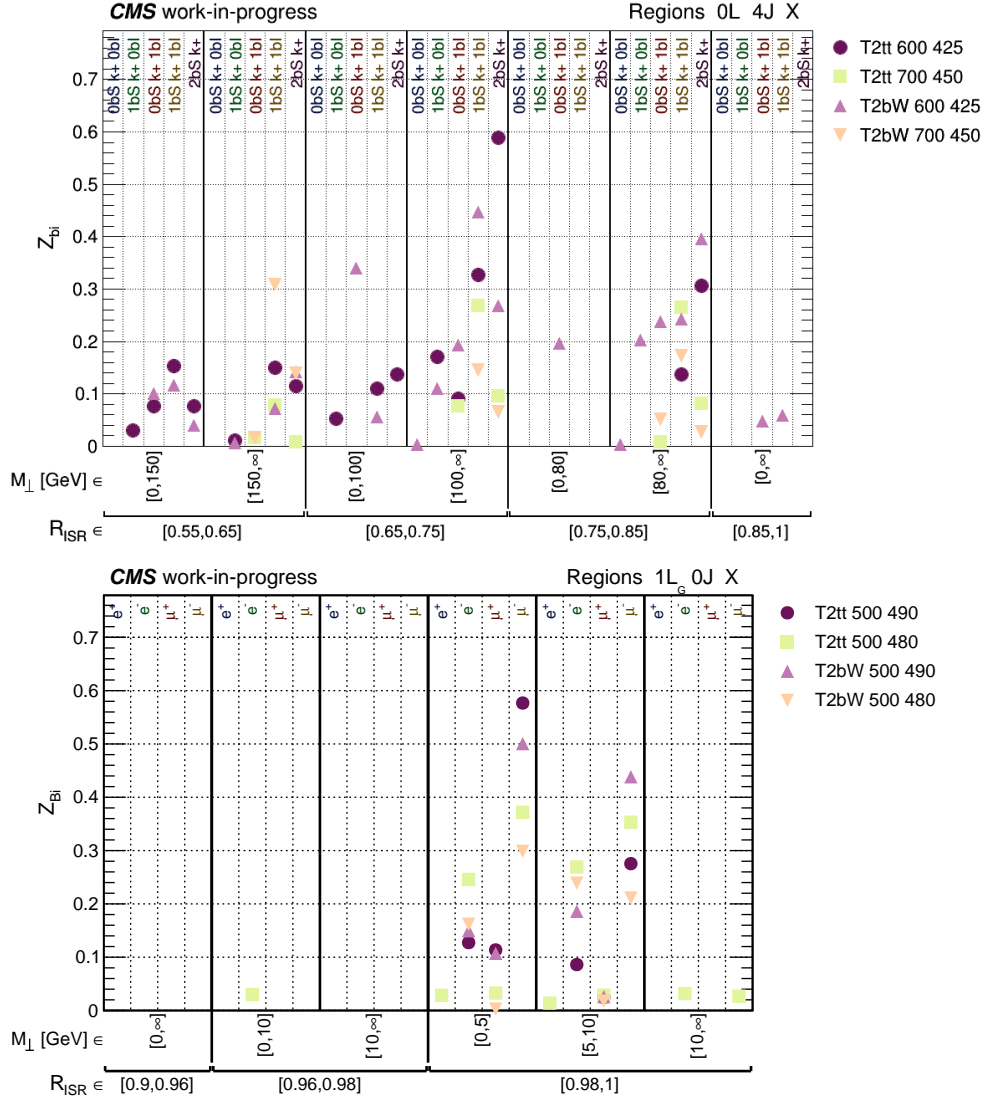


Figure 7.1: Distributions that show the relative sensitivity of compressed stop processes in R_{ISR} and M_{\perp} bins. The top distribution shows 0 lepton and 4 S-jets with color-coded b-tag counting categories. The k^+ denotes high p_T^{ISR} and high γ_{\perp} categories. The bottom distribution shows 1 gold lepton and 0 S-jets with color-coded lepton flavor categories. The X in both distribution indicates the integration over all sub-categories not explicitly listed.

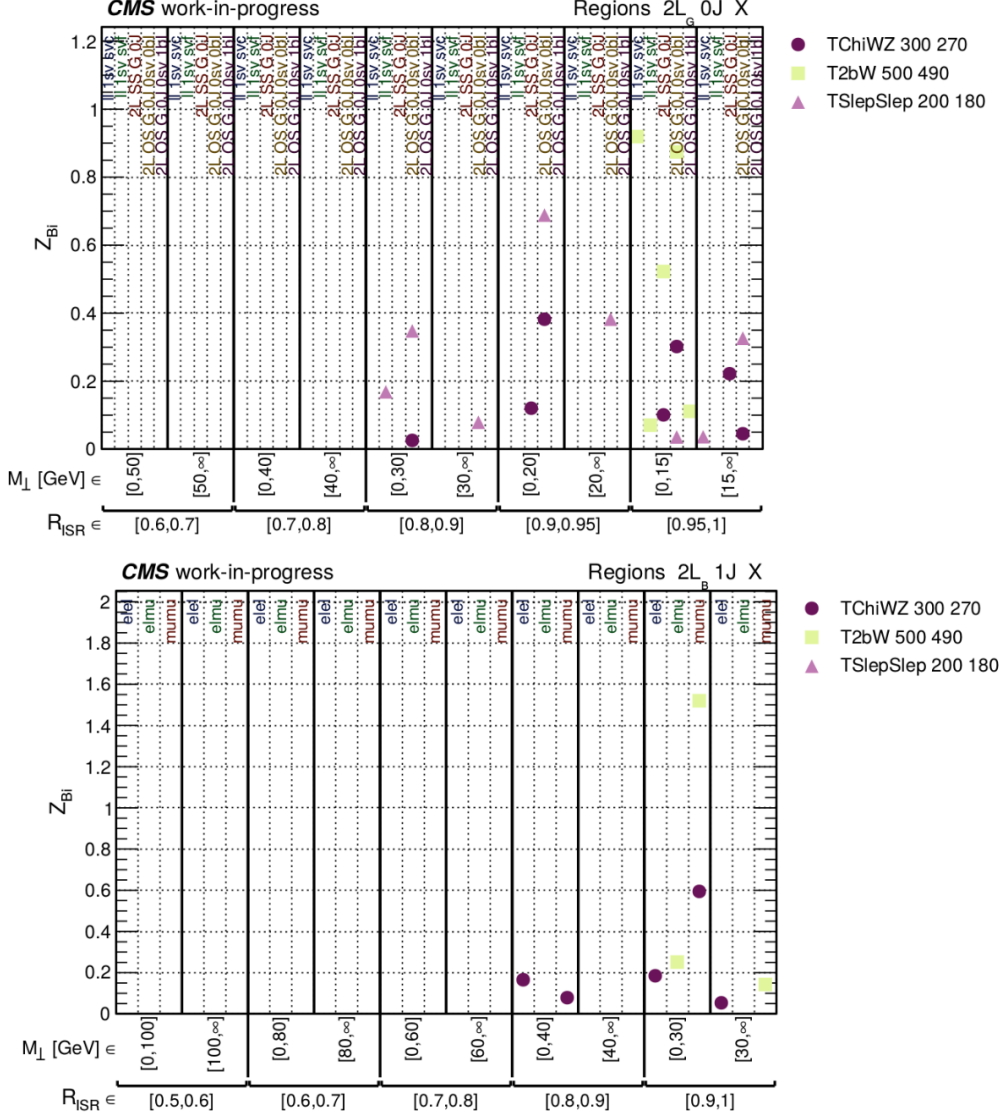


Figure 7.2: A comparison of three different signal processes with a 2 lepton selection for R_{ISR} and M_1 bins. The top plot shows gold regions with 0 S-jets which are split by sign or include SVs. The bottom plot shows bronze regions with 1 S-jet split by flavor combinations. Bronze categories are still sensitive at high R_{ISR} despite being considered background rich regions. The X in both distributions indicates integration of all categories not shown.

in the fit: freely floating rate parameters, log-normal constrained parameters, and shape parameters. Freely floating parameters contribute to a factor κ , with a starting value of one, that is multiplied by the expected bin yield λ , adjusting the yield by some fraction with respect to the nominal value. The free parameters have no associated penalty with their adjustment and are fully determined by data. Individual bins i are mapped together by common processes, k , which are all associated under a common nuisance parameter j . The selection of processes associated to a nuisance parameter can either be from a non-fake background process or flavor and source separated fake leptons background processes. The definition of a free rate parameter can then be defined as

$$\kappa_{ijk}(\alpha_j) = \alpha_j \quad (7.2)$$

The log-normal parameters also use a κ factor that is applied to the expected events of the associated bin. The log-normal parameters are different from the freely floating parameters such that they are penalized for moving from the nominal value with a normally distributed prior $\pi(\alpha_j)$. The prior uncertainty associated with a process j and nuisance parameter k , is written as σ_{jk} . The log-normal definition follows with:

$$\kappa_{ijk}(\alpha_j) = (1 + \sigma_{ijk})^{\alpha_j} \quad (7.3)$$

The third type of nuisance parameter is different from the first two because it adjusts expected bin yields based on the underlying shapes of the R_{ISR} and M_\perp distributions. The κ factor for shapes is then a function of up and down variations of one of the kinematic variables and is encoded with a normally distributed prior $\pi(\alpha_j)$. The κ definition is based on the interpolation $-1 < \alpha_j < 1$ and is written as follows based on a predefined shape treatment [80].

$$\kappa_{ijk}(\alpha_j) = 1 + \frac{1}{2}((\delta^+ - \delta^-)\alpha_j + \frac{1}{8}(\delta^+ + \delta^-)(3\alpha_j^6 - 10\alpha_j^4 + 15\alpha_j^2)) \quad (7.4)$$

The δ^\pm components are ratios of the up and down shape variations of the nominal shape $\lambda^{nominal}$ such that $\delta^+ = \lambda^{up}/(\lambda^{nominal} - 1)$ and $\delta^- = \lambda^{down}/(\lambda^{nominal} - 1)$.

The Likelihood Equation 7.1 combines the three types of nuisance parameters from equations 7.2, 7.3, and 7.4. Each nuisance parameter is mapped to either a set of processes or shapes in conjunction with a mapping to a set of bins. The fit adjusts the three κ factors to maximize the agreement between the observed data \vec{n} and the modeled expected events, $\vec{\lambda}$, in a maximum likelihood sense.

7.4 Definitions of Modeling Systematics

The set of nuisance parameters has gone through an extensive evolution, beginning with very early fits with only 10 nuisance parameters [59]. The first fits only used a single nuisance parameter to describe b-tag systematics, one for MET trigger systematics, one for luminosity and one for each background process rate. The final configuration consists of over 200 nuisance parameters which are divided into 5 subcategories: kinematic, process normalizations, lepton fakes, lepton categorization, and b-tagging. The optimizations of these nuisance parameters, that is, their bin association, process mapping, and allowed degrees of freedom, have undergone extensive study. The complete list of systematics, their type, and prior uncertainties are listed in Tables 7.1 – 7.7. The kinematic nuisance parameters from Table 7.1 contribute 27 factors which serve the purpose of accounting for systematic effects between the high and low p_T^{ISR} and γ_\perp for each lepton and jet multiplicity. The kinematic nuisance parameters, and nuisance parameters in general, that appear to be missing (e.g. γ_\perp 0L 1J) are merged with neighboring jet multiplicities if they are determined to be extraneous degrees of freedom or are highly correlated with another nuisance parameter. Table 7.2 describes 73 nuisance parameters designed to accommodate systematic effects from categorization of b-tagged jets in either the S or ISR system for each lepton and jet multiplicity. Regions with few b-tags are mapped to all background processes, otherwise, each

Table 7.1: Kinematic nuisance parameter mappings which are applied to the “high” bins. Bracketed jet mappings indicate all integer jet multiplicities between the listed inclusive edges. All factors are assigned a 20% prior uncertainty.

Category Mapping	N_L Mapping	N_{jets}^S Mapping
p_T^{ISR}	0	$[1, \geq 5]$
p_T^{ISR}	1	$[0, \geq 4]$
p_T^{ISR} (QCD)	0	$[0, \geq 5]$
γ_\perp	0	$[2, \geq 4]$
γ_\perp	1	$[1, \geq 4]$
γ_\perp	2	$[0, \geq 2]$
γ_\perp (QCD)	0	$[2, \geq 4]$

nuisance parameter process mapping is divided into tt+jets or not tt+jets. There are 21 lepton categorization nuisance parameters which account for systematically different rates in gold categories versus silver or bronze categories. Table 7.4 shows the rates for each background process normalizations, which includes a special hierarchy parameterization that will be discussed later. The strategy for splitting background process degrees of freedom is that dominant processes are split by lepton and jet multiplicity, intermediate backgrounds are split by lepton, and rare backgrounds are mapped globally with a single nuisance parameter. The fake lepton nuisance parameters are comprised of global rates for each flavor and source, a single nuisance parameter to account for the global rate of charge misidentification, and the fake shapes. The fake shapes are split by flavor, lepton multiplicity, and jet multiplicity. The fake shapes were originally split by source but this introduced many extraneous parameters where heavy flavor and light flavor sources were highly correlated. The fake shapes target systematic effects from the shapes in R_{ISR} or M_\perp and are based on 1σ up and down variations applied to the shape template in Equation 7.4 [81]. The last two tables 7.6 and 7.7 account for systematics from SV efficiency and pseudo-rapidity, as well as, other sources of systematics.

The process normalization hierarchy listed in Table 7.4 is a special parameterization of nuisance parameters organized into a tree of factors. This parameterization is implemented separately for the two dominant backgrounds W+jets and tt+jets. The factor at the top

Table 7.2: The log-normal nuisance parameter mapping for all b-tag counting categories. Includes all combinations of Process \times Category $\times (N_\ell, N_{jet}^S)$ multiplicities. All factors are assigned a prior 20% uncertainty.

Process Mapping per (N_ℓ, N_{jet}^S)	
(Combined/All) or ($tt + jets$) or (not $tt + jets$)	
Category Mapping per (N_ℓ, N_{jet}^S)	
$(N_{b\text{-tag}}^{ISR}, N_{b\text{-tag}}^S) = \{(0, 1), (1, 0), (1, 1), (\text{inclusive}, \geq 2)\}$	
Combined/All Nuisances	
$(N_\ell, N_{jet}^S) = \{(0, 1), (1, 1), (2, 1), (2, 2)\}$	

Table 7.3: Lepton category nuisance parameter mapping. The complete set of nuisance parameters is represented by the product of the $N_\ell \times N_{jet}^S$ with an assigned prior uncertainty or 20%. The category !Gold indicates the combined Silver and Bronze categories.

N_{jet}^S Mapping	Inclusive	N $_\ell$ Mapping		
		1 ℓ	2 ℓ	3 ℓ
	Inclusive		$(ee, \mu\mu, e\mu) \times \text{!Gold}$	$(Z*, noZ*)$
	0J	$(e, \mu) \times (\text{Gold}, \text{!Gold})$	$(\ell\ell) \times (\text{Gold}, \text{!Gold})$	$(OS, SS) \times \text{Gold}$
N_{jet}^S Mapping	1J	$\ell \text{ Gold}$	$(Z*, noZ*) \times \text{Gold}$	
	2J	$\ell \text{ Gold}$	$(Z*, noZ*) \times \text{Gold}$	
	3J	$\ell \text{ Gold}$		
	4J	$\ell \text{ Gold}$		

Table 7.4: The nuisance parameter mapping split by lepton and jet multiplicity for background processes. The dominant backgrounds W+jets and tt+jets are implemented with a hierarchy parameterization of factors. Global factors indicate mapping to every bin and N_{jet}^S implies each possible number of jets for a given lepton multiplicity.

Category Mapping	Process Mapping	Param. Details
per $(N_\ell = 1, 2, 3, N_{jet}^S)$	W+jets	hierarchy
per $(N_\ell = 0, N_{jet}^S)$	$(W + \text{jets}) + (\text{ZDY})$	hierarchy
per (N_ℓ, N_{jet}^S)	tt+jets	hierarchy
per $(N_\ell = 0, 1, 2, N_{jet}^S)$	QCD	0 ℓ floating otherwise 20% prior
per $N_\ell = 1, 2, 3$	$(\text{ZDY}) + (\text{DB})$	20% prior
per $N_\ell = 0, 1, 2$	ST	20% prior
global	TB	20% prior
global	ZDY	free floating
global	DB	free floating

Table 7.5: The nuisance parameters associated to fake leptons. The global or silver or bronze rates are split between MC matched source of either Heavy flavor or Light flavor. The shape systematics are applied per lepton and S-jet combinations but combine HF/LF sources and split by flavor only.

Category Mapping	Process Mapping	Parameter Details
$\ell^\pm \ell^\pm$	Global	Free floating
Global	$(e, \mu) \times (HF, LF)$	Free floating
Silver	$(e, \mu) \times (HF, LF)$	20% prior
Bronze	$(e, \mu) \times (HF, LF)$	20% prior
per (N_ℓ^S, N_{jet}^S)	$(e, \mu) \times (R_{ISR}^{shape}, M_\perp^{shape})$	5% prior

Table 7.6: The set of nuisance parameters associated to the categories that involve tagged SVs. The SV counting rates are mapped globally to every bin and the kinematic η separation is split between SVs associated with tt+jets versus SVs associated with anything else.

Category mapping	process mapping
$N_{SV}^S = 1$	All
$N_{SV}^S \geq 1$	All
$ \eta_{SV}^f $	tt+jets
$ \eta_{SV}^f $	other

Table 7.7: Additional secondary systematics which account for various scale factors or systematic effects of jet reconstruction and clustering. The nuisance parameters with a (*) are not currently implemented but will be added in later in the final model.

Systematic Source and Scale Factors	Parameter Type
Luminosity	log-normal
e, μ Efficiency	log-normal
b-tag efficiency	log-normal
*Factorization, Renormalization, PDF, and Q^2	log-normal
*JES & type-I MET	shape
*Unclustered Energy	shape
MET Trigger Efficiency	shape
Lepton FastSIM SF	log-normal
SV FastSIM SF	log-normal
b-jet FastSim SF	log-normal
*MET FastSim Correction	shape

of the hierarchy is the root factor and is the region with the highest statistical power and purity for that process. This factor, for a particular lepton and S jet multiplicity, informs neighboring jet multiplicity factors and in turn those neighbors then inform their neighbors. This allows for the root parameters for each process to be interpreted as an estimate of a single normalization scale factor for that group of processes, while also allowing for independent factors in different multiplicities to be interpreted and constrained relative to the higher factor.

For example: the root factor for W+jets is 1L 0J, chosen because it is 14% of the total process yield and 93% of the total background for that particular region. 0L 2J, 1L 1J, and 1L 2J have comparable statistics with up to 20% more events but with 20% less purity (the fraction of W+jets to other backgrounds). The $\kappa_{1L,0J}^{W\text{jets}}$ “root” scale factor maps to every analysis bin for the W+jets process and governs the overall rate. This means that the root factor is multiplied by every other scale factor in each lepton multiplicity. An example low level parameter would be $\kappa_{1L,4J}^{W\text{jets}}$, which is multiplied by $\kappa_{1L,0J}^{W\text{jets}}$, $\kappa_{1L,1J}^{W\text{jets}}$, $\kappa_{1L,2J}^{W\text{jets}}$, $\kappa_{1L,3J}^{W\text{jets}}$ and interpreted as relative to each preceding nuisance parameter at a higher level in the hierarchy. A similar hierarchical parameterization is evaluated for tt+jets, and both hierarchy trees are shown in Figure 7.3. The 0L hierarchy for W+jets is special, due to very high correlations with the ZDY process from the similarities between W and $Z(\rightarrow \nu\nu)$ decays. Here, the process mapping combines the ZDY and W+jets backgrounds while the ZDY, DB factor for 0L has been removed.

7.5 Development of Modeling Systematics

The optimization of each group of systematics was conducted primarily on CR fits to 2016 data and then expanded to include multiple years accounting for systematic effects induced from different run conditions in each year. The statistical evaluation of each fit is performed by comparing metrics such as the $\log \mathcal{L}$, χ^2 , z-score, and impacts. The impacts are a series of

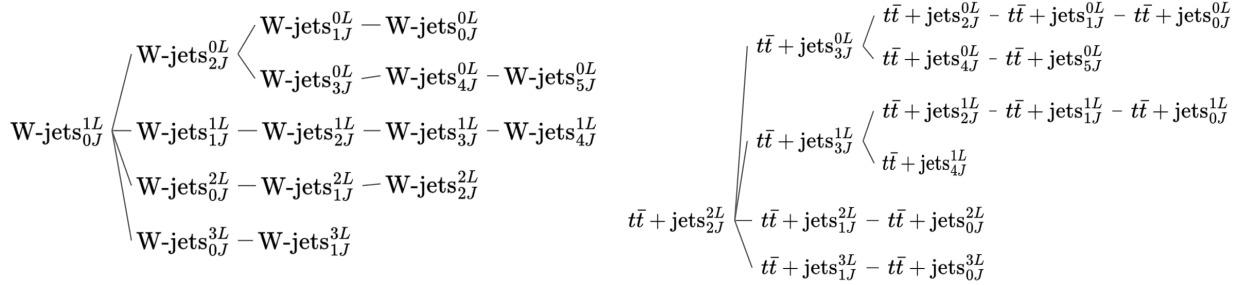


Figure 7.3: Pair of k-nary trees illustrating the hierarchical organization of background rates for $W+jets$ and $t\bar{t}+jets$.

separate fits that independently vary all of the nuisance parameters to assess the impact of each on the POI and is a tool provided by `HiggsCombine`. Multiple definitions of z-scores are used, with the primary one being $(O - E) / \sqrt{(E + \sigma_{\text{post-fit}}^2)}$, where the O is the observed data, E is the expected events post-fit, and the denominator includes the expected post-fit events acting as the Poisson variance. The total error of the denominator is the sum of the Poisson variance, E , and the post-fit variance, $\sigma_{\text{post-fit}}^2$. Similar z-score definitions are used such as the same evaluation without the post-fit variance or evaluated with respect to the pre-fit values. The fit evaluation is performed on all bins and subsets of each individual lepton multiplicity, or gold, silver, or bronze. The statistical errors for each bin are assumed to be Gaussian with sufficient number of events. The cases with bins having very few events are assumed to be Poisson distributed. This distinction is important when combining different bins varying in events by orders of magnitude, into a distribution of z-scores. If a deviation of a few observed events were to occur in a bin with only a few expected events, the z-score would be a significant outlier when it is not. To correct this issue, each bin is given the “Poisson treatment.” A new z-score is calculated from the Poisson probability of the original observation given the expectation. The recipe for calculating the adjusted z-scores is as follows

1. Generate N trials, each with new expectation $E'_i \sim \mathcal{N}(E, \sigma_{\text{post-fit}}^2)$
2. Generate new observations $O'_i \sim \text{Poisson}(E'_i)$

3. Count k successes such that O', E' follow the original observation ($O < E$ or $O > E$)
4. Compute the Poisson probability $P = k/N$
5. Translate P into a z-score with normal distribution quantile
6. Compute error on z-score with up/down variations of binomial error
7. Assign the sign to the new z-score based on $O - E$ convention

The effect of the Poisson treatment is that the z-score significance is reduced in low statistics cases where $O > E$ and increased in cases with $O < E$ due to the asymmetry of the Poisson distribution having a long tail tending to higher values. Comparisons of the final fit model with and without the Poisson treatment are shown Figure 7.4. Example pull distributions that compare the early fit model with the most final model are shown in Figure 7.5. The progression of the fit model's likelihood and nuisance parameter development is summarized Figure 7.6 and accompanied by Table 7.8 with brief descriptions of each milestone in the fit configurations.

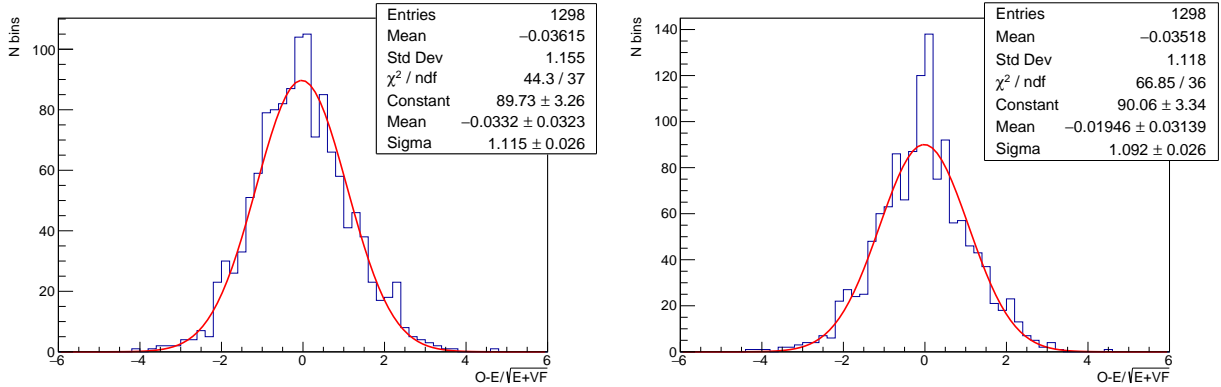


Figure 7.4: Comparison of Run II CR fits with Build 62 of Table 7.8 without Poisson treatment (left) and with Poisson treatment (right). The improvement by implementing the Poisson treatment is shown in the RMS and fitted σ of the right distribution, by reducing the number of large outliers due to bins with low statistics.

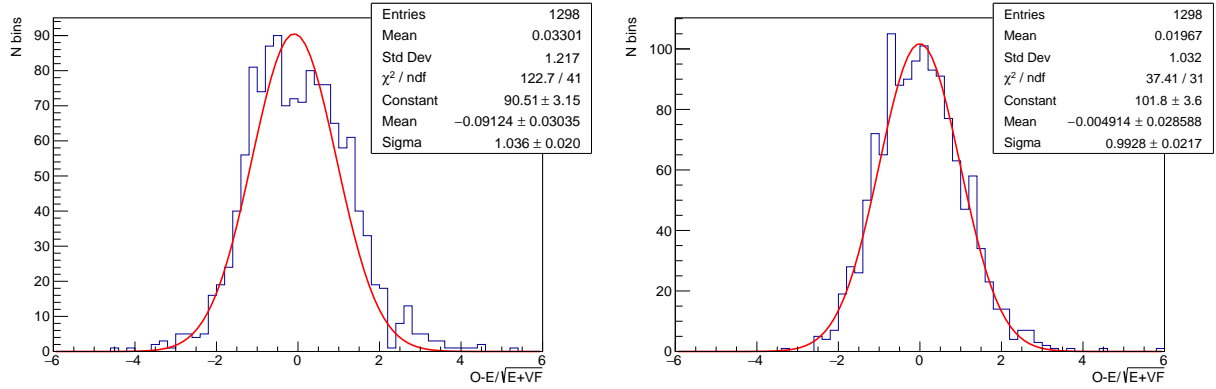


Figure 7.5: A comparison of the Poisson corrected builds from Table 7.8 with the first Build 8 on the left and the final Build 62 on the right. Both distributions use only 2016 data and MC scaled to 138 fb^{-1} .

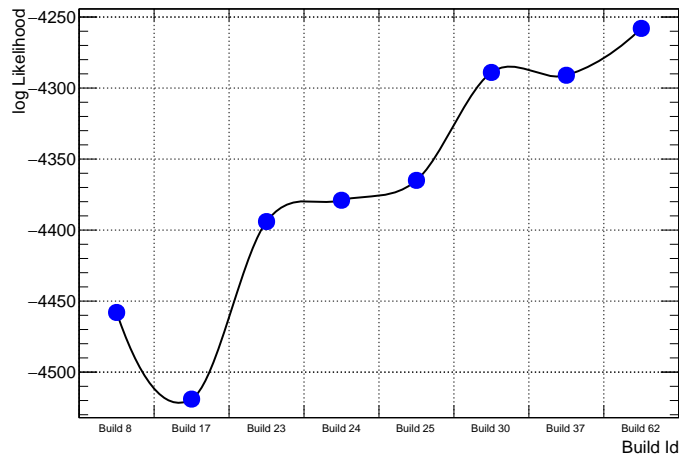


Figure 7.6: The progression of the CR fit log likelihood following the model version milestones listed in the Build Table 7.8.

Table 7.8: Listing of all the model version milestones with a brief description of each build, its Id number and number of nuisance parameters.

Build 8	N Nuisance Parameters = 186
	Used 3 shape systematics for W+jets, QCD, Fakes. All other backgrounds are grouped together under “other” and split by (N_ℓ^S, N_{jet}^S)
Build 17	N Nuisance Parameters = 179
	Removed W+jets and QCD shapes due to over fitting. Added in W+jets hierarchy. Split up “other” into 3 groups {(tt+jets, ST),(ZDY),(DB,TB)} each split by (N_ℓ^S, N_{jet}^S)
Build 23	N Nuisance Parameters = 193
	Added a simplified b-tag configuration with a splitting by ($N_{b\text{-tag}}^S, N_{b\text{-tag}}^{ISR}$) and further split by (N_ℓ^S, N_{jet}^S)
Build 24	N Nuisance Parameters = 194
	Added a nuisance to adjust the rate of same-sign lepton pairs.
Build 25	N Nuisance Parameters = 194
	Added tt+jets hierarchy. Reconfigured background process grouping to {(ZDY, DB),(ST,TB)} with full (N_ℓ^S, N_{jet}^S) splitting
Build 30	N Nuisance Parameters = 229
	Implemented lepton category nuisances from Table 7.3 and the Bronze and Silver global fake rates from Table 7.5
Build 37	N Nuisance Parameters = 209
	Reworked background process grouping to the final configuration in Table 7.4 and consolidated extraneous degrees of freedom. Consolidated Fake shapes to no longer split between HF and LF.
Build 62	N Nuisance Parameters = 227
	Reworked b-tagging parameters to include process splitting from Table 7.2. This build reflects the final configuration of all previously described nuisances and those implemented from Table 7.7.

7.6 Control Region and Validation Region Fit Results

The results of the control region fit and the control region plus validation region fit using the fit model described in the previous section lead to good agreement between data and MC. Distributions summarizing the effects of the various nuisance parameters, with simplified categorization splitting over a targeted category and integrated over sub categories, are shown in Figures 7.7, 7.8, 7.9, 7.10, and 7.11. Figures 7.7 and 7.8 show a summary of the data and MC agreement for each lepton multiplicity. This demonstrates the benefit of the jet multiplicity splitting, and also the effect of kinematic factors in 2L and 3L. Figure 7.9 shows splitting by p_T^{ISR} , γ_\perp , and the region with the W+jets root factor. Figure 7.10 shows the lepton category splitting and a fake dominated bronze category. The final CR summary in Figure 7.11 illustrates the splitting by SV and b-tag counting.

In addition to the control region only fit, a control region combined with the validation region fit was performed. This fit uses the final systematic configuration but excludes the fake shapes. Fake shapes are excluded because their implementation requires consistent numbers of bins across gold, silver, and bronze. This uniform binning requirement disqualifies the validation region because the bronze bins cover the entire R_{ISR} range whereas the gold and silver regions do not. The CR+VR fit result is reasonable, but has apparent systematic mismodeling from the absence of fake shapes. To ensure that the high R_{ISR} modeling is good, a bronze only fit across the full R_{ISR} spectrum is performed. This fit includes only the bronze categories and the complete set of systematics. Results are shown in Figure 7.12 which show reasonable modeling in high R_{ISR} regions with fake shapes.

7.7 Bias tests

One possible danger of having a fit with too many degrees of freedom is that the model would be too flexible and fit away potential signal. In testing for over-fitting, we perform an ensemble of pseudo-experiments with and without signal injection to test if the fit model

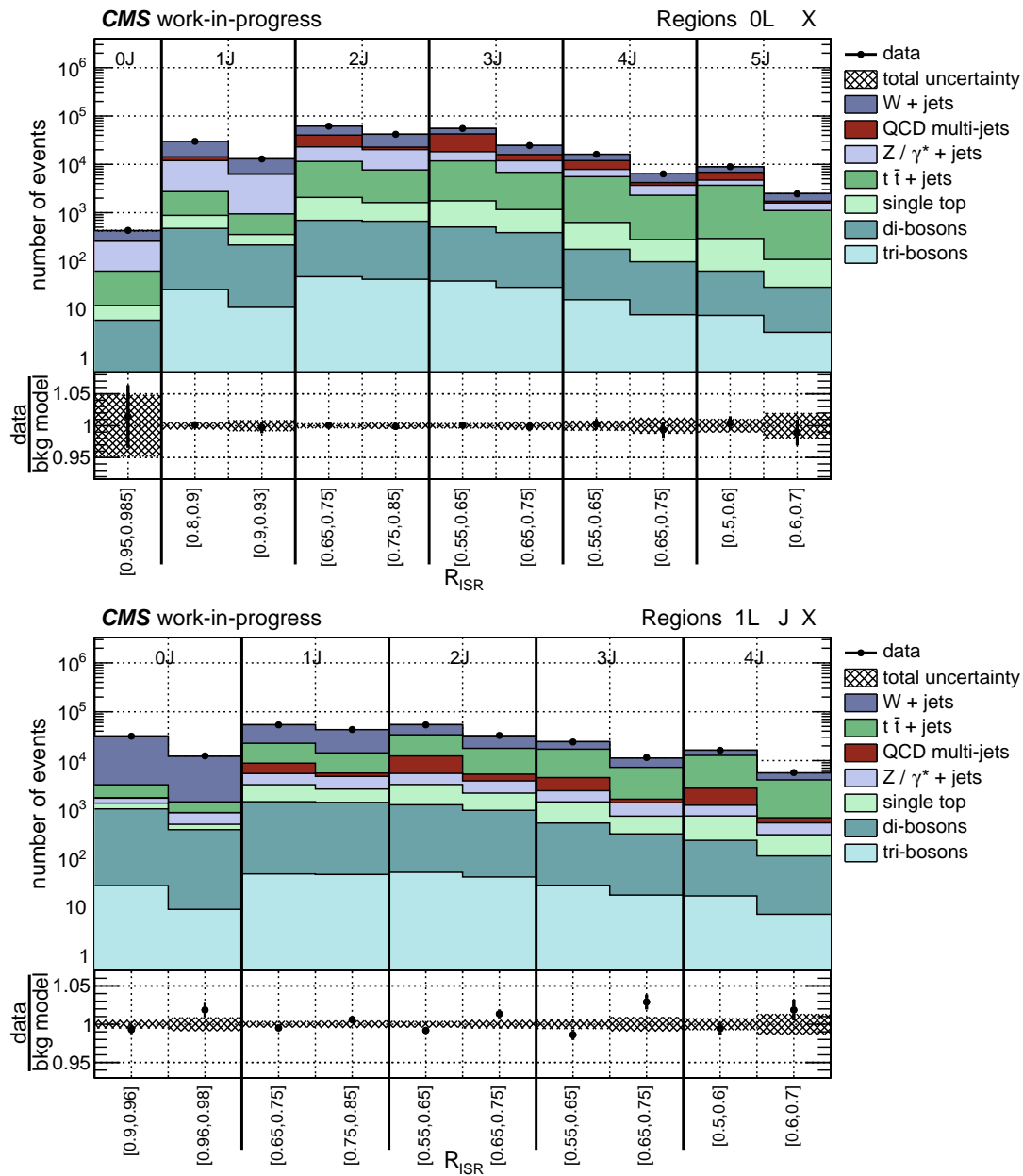


Figure 7.7: CR post-fit summary plots split by number of S-jets for 0 and 1 leptons.

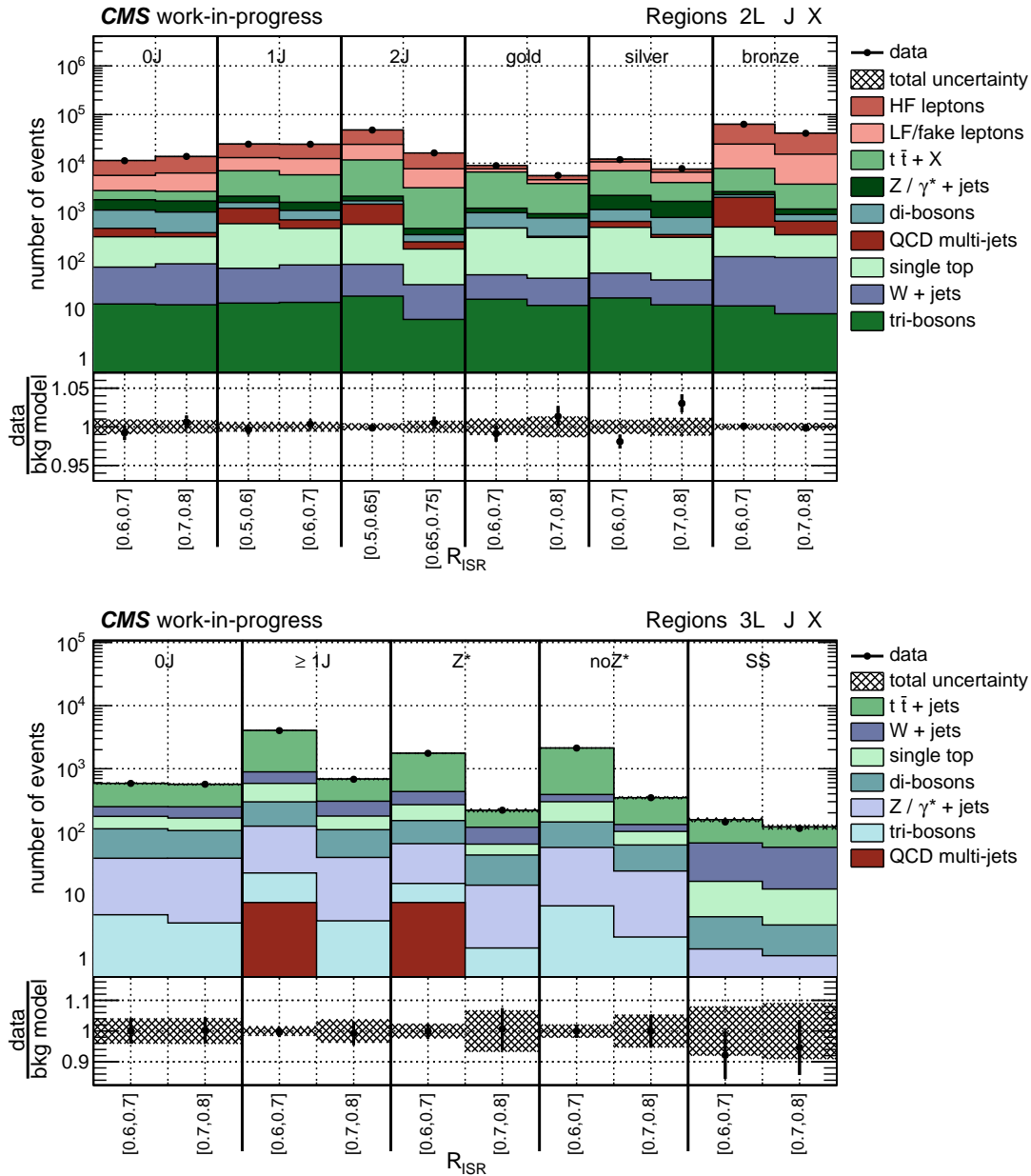


Figure 7.8: CR post-fit summary plots split by number of S-jets or lepton category for 2 and 3 leptons. The two included types of splitting shown are not mutually exclusive.

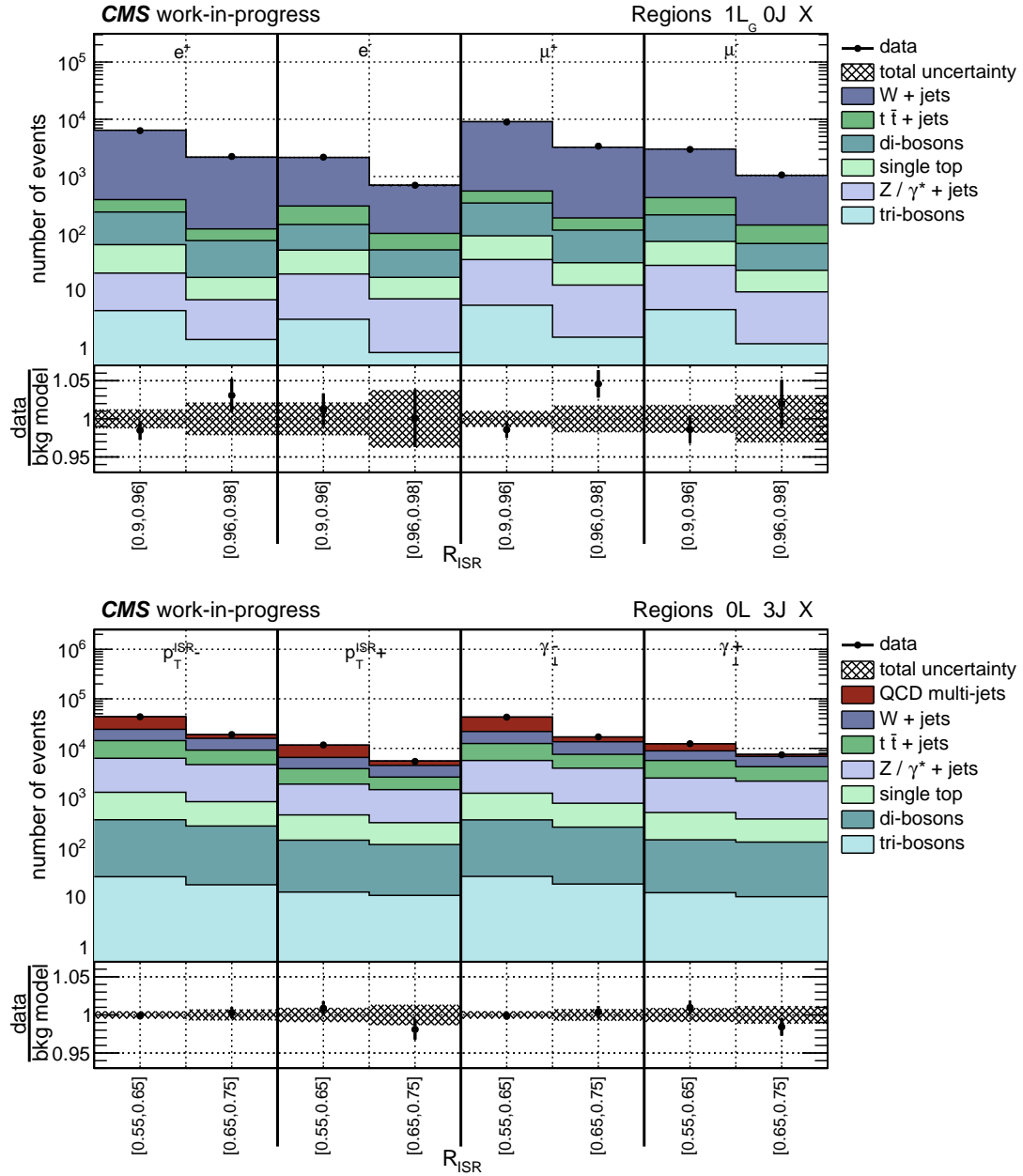


Figure 7.9: CR post-fit summary plots with the category associated with the root factor of W+jets (top) and a 0 lepton selection splitting by kinematic categories p_T^{ISR} and γ_\perp (bottom).

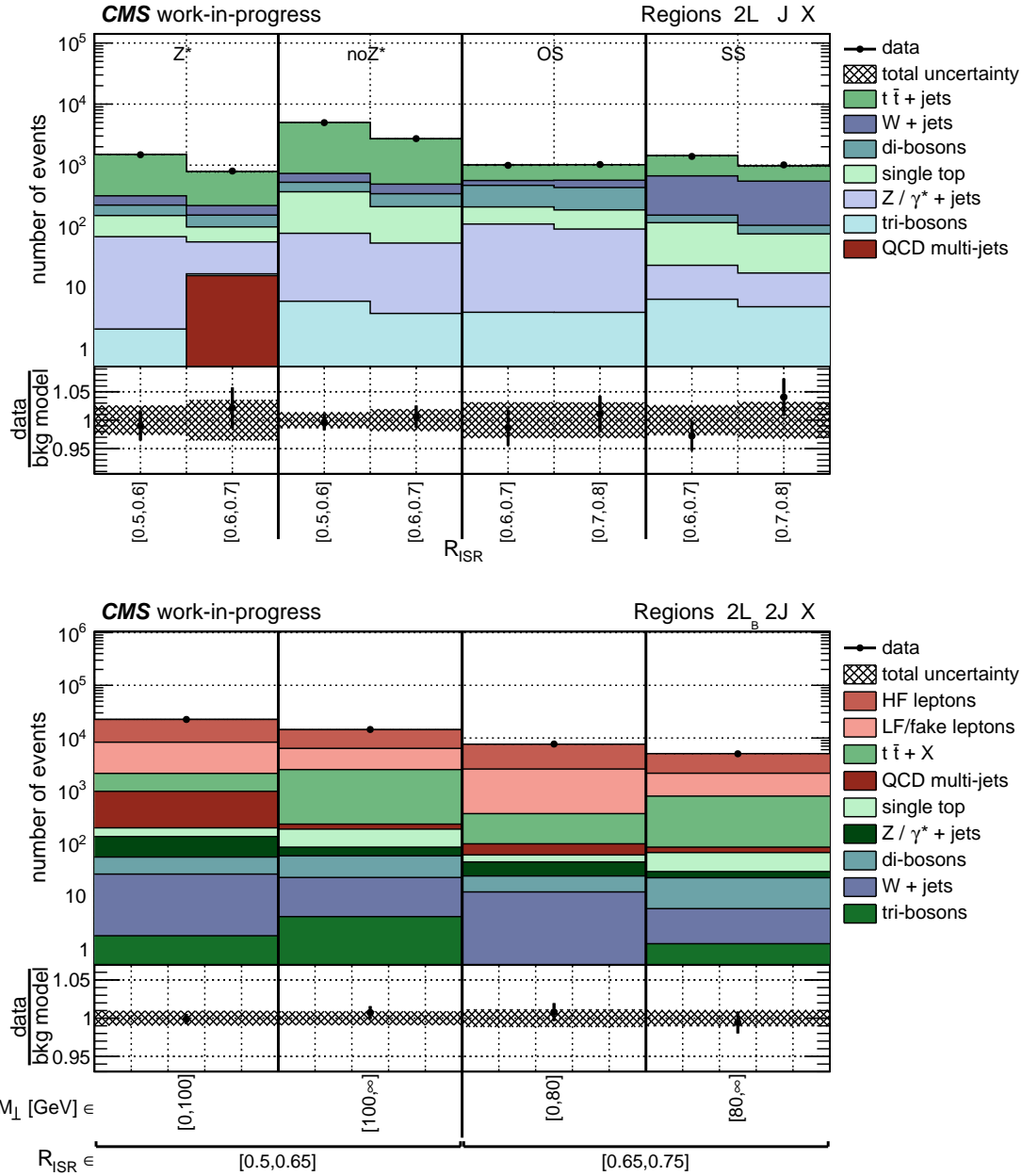


Figure 7.10: CR post-fit summary plots demonstrating the effects on 2 leptons which are split by lepton categories (top) or a bronze only region which is strongly associated with lepton fake factors (bottom).

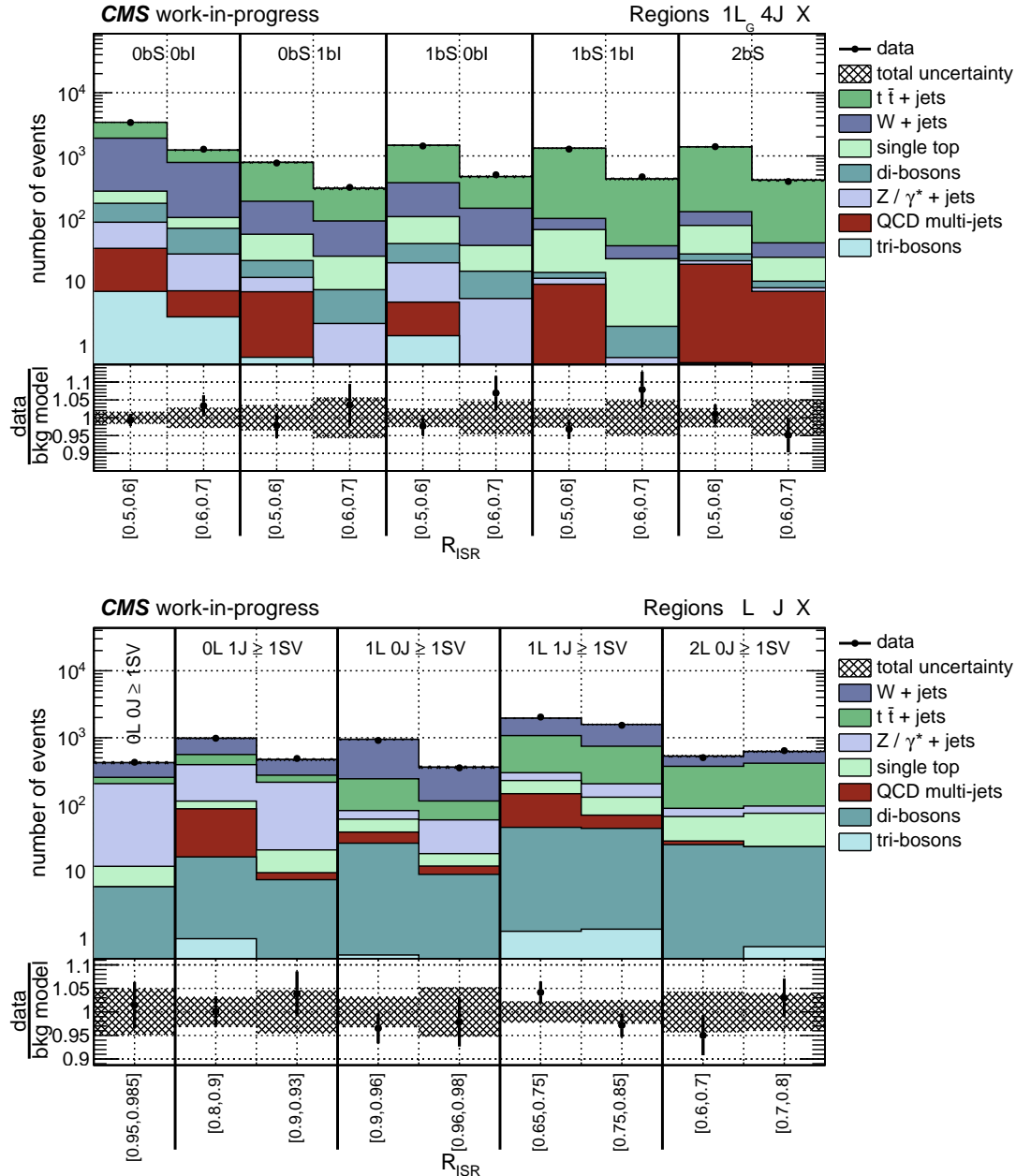


Figure 7.11: CR post-fit summary examples which show the agreement of data to the fitted background model for b-tagging and SV categories.

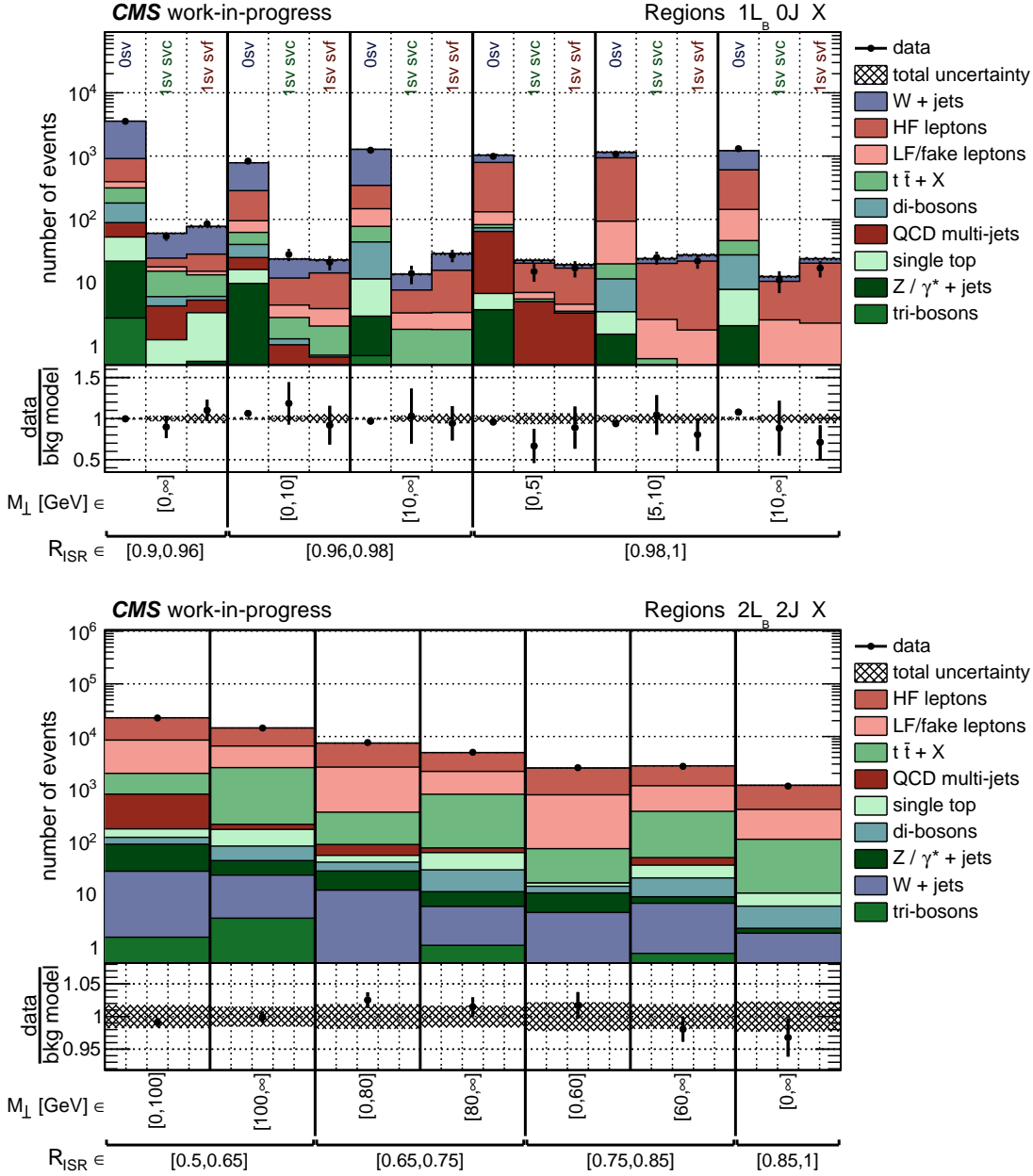


Figure 7.12: The Bronze only category fit with fake dominated 1 lepton and 2 lepton bronze categories.

recovers the correct hypothesis. If the fit is unbiased and sensitive to various signals then the signal strength parameter, r , should be evaluated as $r = 0$ in a background only fit and $r = 1$ when signal is injected. The hypotheses are tested by generating observed data in each bin centered on the MC expectation, fitting all regions simultaneously, and extracting the r value. Each pseudo-experiment is performed with a handful of points around the edge of the expected mass limits for T2tt, TChiWZ, and TSlepSlep. The results are shown in Figure 7.13. These show no fit bias given that the correct hypothesis is recovered. This means that the final set of nuisance parameters is sufficiently small and does not affect the fit's sensitivity to discovery.

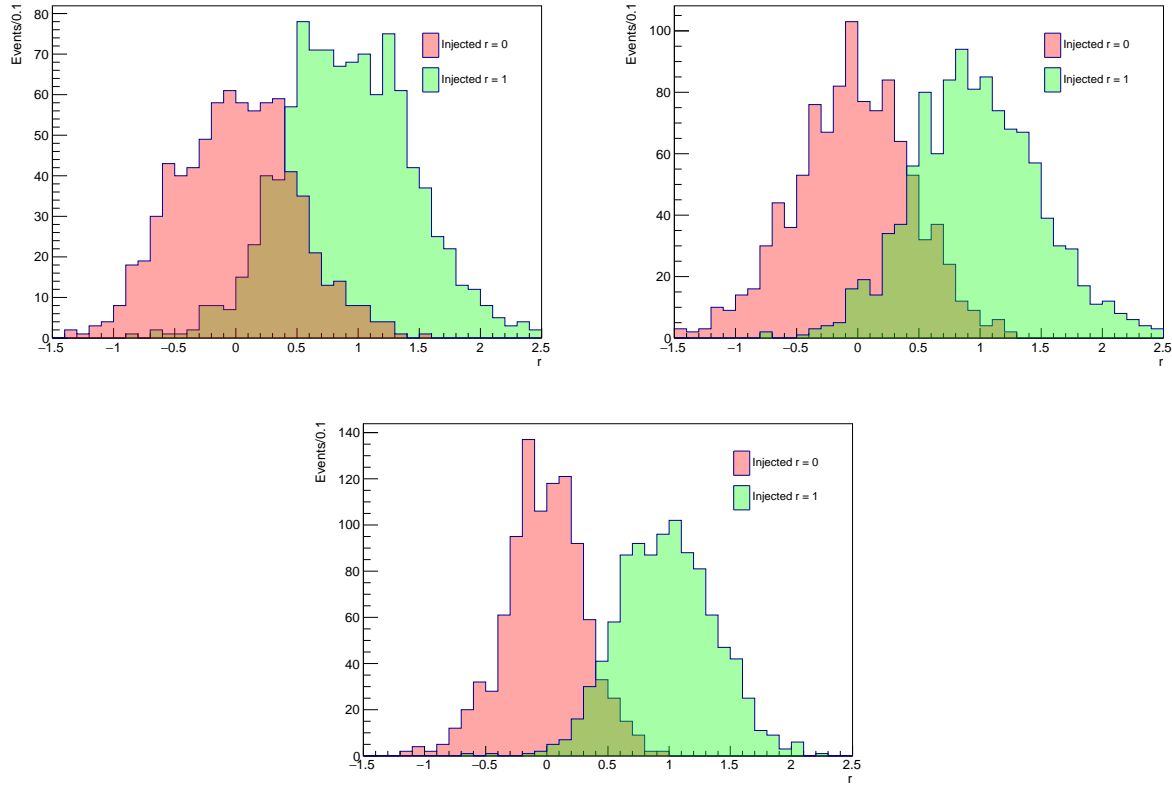


Figure 7.13: Signal injection and bias test for three different signal grid points. The top left is T2tt with $m_{\tilde{t}} = 750$ GeV and $m_{\tilde{\chi}_1^0} = 670$ GeV. The top right is TChiWZ with $m_{\tilde{\chi}_2^0} = 325$ GeV and $m_{\tilde{\chi}_1^0} = 315$ GeV. The bottom figure uses TSlepSlep with $m_{\tilde{t}} = 250$ GeV and $m_{\tilde{\chi}_1^0} = 245$ GeV [1].

Chapter 8

Results

8.1 Asymptotic Limits

This search is designed to be generically sensitive to SUSY with an emphasis on compressed scenarios. The consequence is sensitivity to a wide variety of models and final states, so we present expected upper limits on the cross sections for stop, electroweakino, and slepton processes. The results use the full Run II SM MC background combined with the data driven fit model described in the previous chapter. The limits are calculated using the asymptotic method for profile-likelihood test statistic [61].

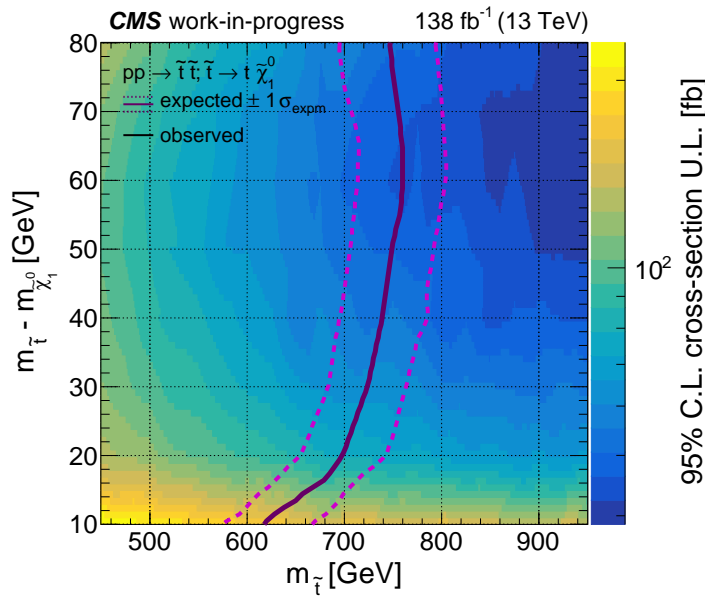


Figure 8.1: Run II expected cross section upper limits for di stop production, T2tt, excluding stop masses to the left of the 95% CL line.

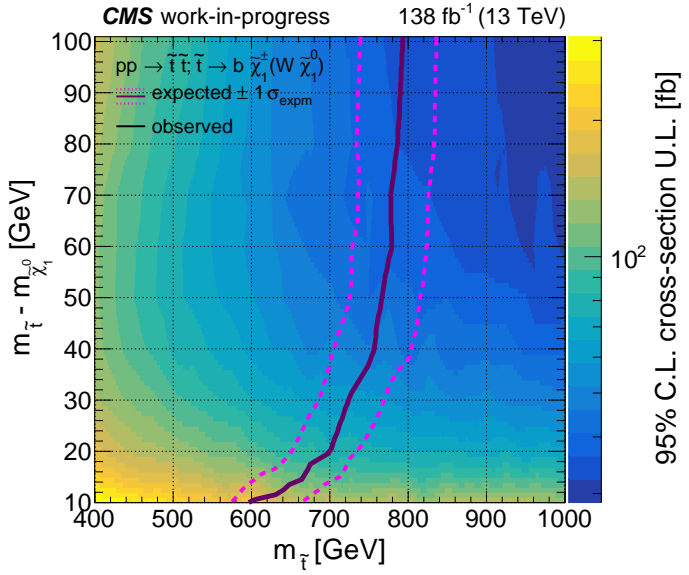


Figure 8.2: Run II equivalent expected cross section upper limits for di stop production with an intermediate chargino, T2bW. The MC uses the 2016 samples with 2016 luminosity and 2017 samples scaled to the combined 2017 and 2018 integrated luminosity. The chargino mass is assumed to be halfway between the LSP and stop mass for each grid point.

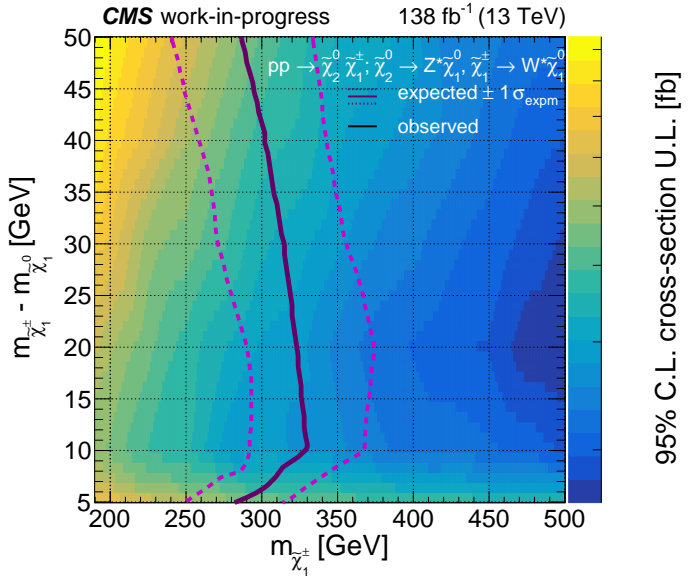


Figure 8.3: Run II expected cross section upper limits for Neutralino and Chargino production, TChiWZ, which excludes chargino masses to the left of the line with 95% CL. Shown as a function of the chargino mass and chargino-LSP mass difference. The simplified model uses the Wino-like cross-section and assumes that the initial sparticle pair are mass degenerate $m_{\tilde{\chi}_2^0} = m_{\tilde{\chi}_1^{\pm}}$.

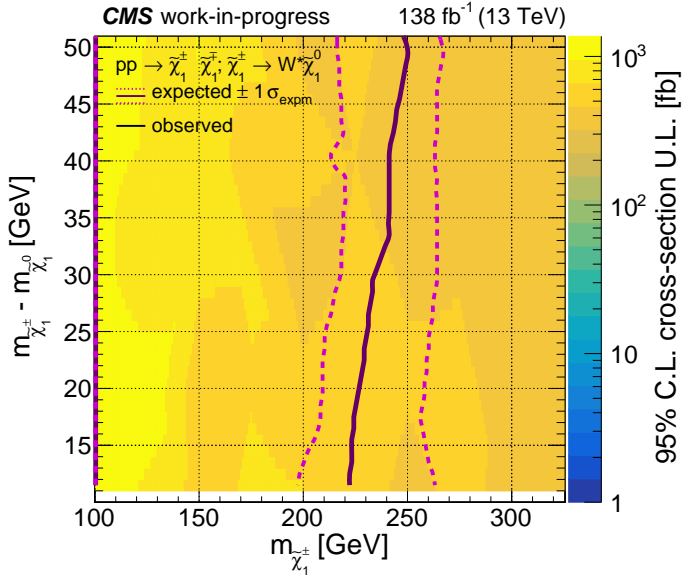


Figure 8.4: 2017 expected cross section upper limits scaled to the full Run II integrated luminosity of 138 fb^{-1} for chargino pairs decaying to an oppositely signed W boson pair. Chargino masses are excluded to the left of the line with 95% CL. Limits are based on wino cross-sections and a sample which is filtered to purely leptonic decays.

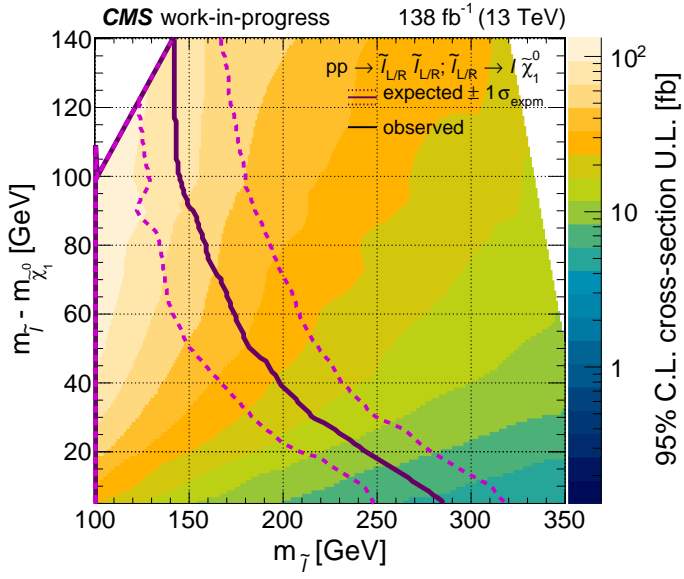


Figure 8.5: Run II expected cross section upper limits that exclude slepton masses to the left of the line at 95% CL. Shown as a function of slepton mass and slepton-LSP mass splitting. The L/R indicates the super partners of the SM left or right handed partner which are assumed to be degenerate in mass.

8.2 Model Dependent Interpretation

The TChiWZ limits from the previous section use a simplified model which is described in Chapter 1. The decay kinematics in this simplified model use a flat matrix element resulting in W and Z boson 3 body uniform phase space decays. However, the 3 body decay phase space depends on the sign of the eigenstates of the neutralino mass matrix. A reweighting of events in the simplified TChiWZ model is performed to assess the difference in kinematics of the Z decay. This model reinterpretation has been done by other analyses in ATLAS and CMS [82][4], but are restricted to $Z(\rightarrow \ell\ell)$. We extend the reweighting strategy to the more general case of di-fermion pairs where neutralino A undergoes a three body decay to a di fermion pair and neutralino B.

$$A \rightarrow f\bar{f}B \quad (8.1)$$

The expression for the matrix element of the process in Equation 8.1 uses a phase space parameterization x, y, z according to [83] which can be used to express the partial width

$$\frac{d^2\Gamma^\pm}{dxdy} \sim \frac{(1-x)(x-r_B^2) + (1-y)(y-r_B^2) \pm 2|r_B|z}{(z-r_z^2)^2} \quad (8.2)$$

x, y, z are represented by mass ratios

$$\begin{aligned} x &= (m_{\bar{f}B}/m_A)^2 \\ y &= (m_{fB}/m_A)^2 \\ z &= (m_{f\bar{f}}/m_A)^2 \end{aligned} \quad (8.3)$$

and the r parameters represent mass ratios of particle B or Z mass with particle A

$$\begin{aligned} r_B &= m_B/m_A \\ r_Z &= m_Z/m_A \end{aligned} \quad (8.4)$$

By sampling the x, y, z space from Equation 8.2 along the allowed boundaries:

$$\begin{aligned} r_B^2 \leq x \leq 1 \\ r_B^2 \leq x \leq 1 \\ z(xy - r_B^2) \geq 0 \end{aligned} \tag{8.5}$$

we can generate the four momentum of all particles in the 3 body decay according to the two eigenstate cases, OS (Γ^-) and SS (Γ^+). Using the model dependent (x, z) distribution a weight can be calculated mapping the original phase space of the simplified model to the OS or SS case. The Dalitz distributions, which fully describe the differences in Z decays in terms of x and z are shown in Figure 8.6 for a TChiWZ grid point with $m_A = 300$ GeV and $m_B = 270$ GeV.

The relative differences in the final state kinematics for each model is shown in Figure 8.7 which uses the same TChiWZ grid point.

The resulting limits for the model dependent cases are shown in Figure 8.8. The exclusion boundary, between the two model dependent cases, are similar but the OS scenario is able to exclude higher masses likely due to the momentum enhancement of A (LSP) which produces a larger missing momentum signature as seen on the red curve in Figure 8.7 right.

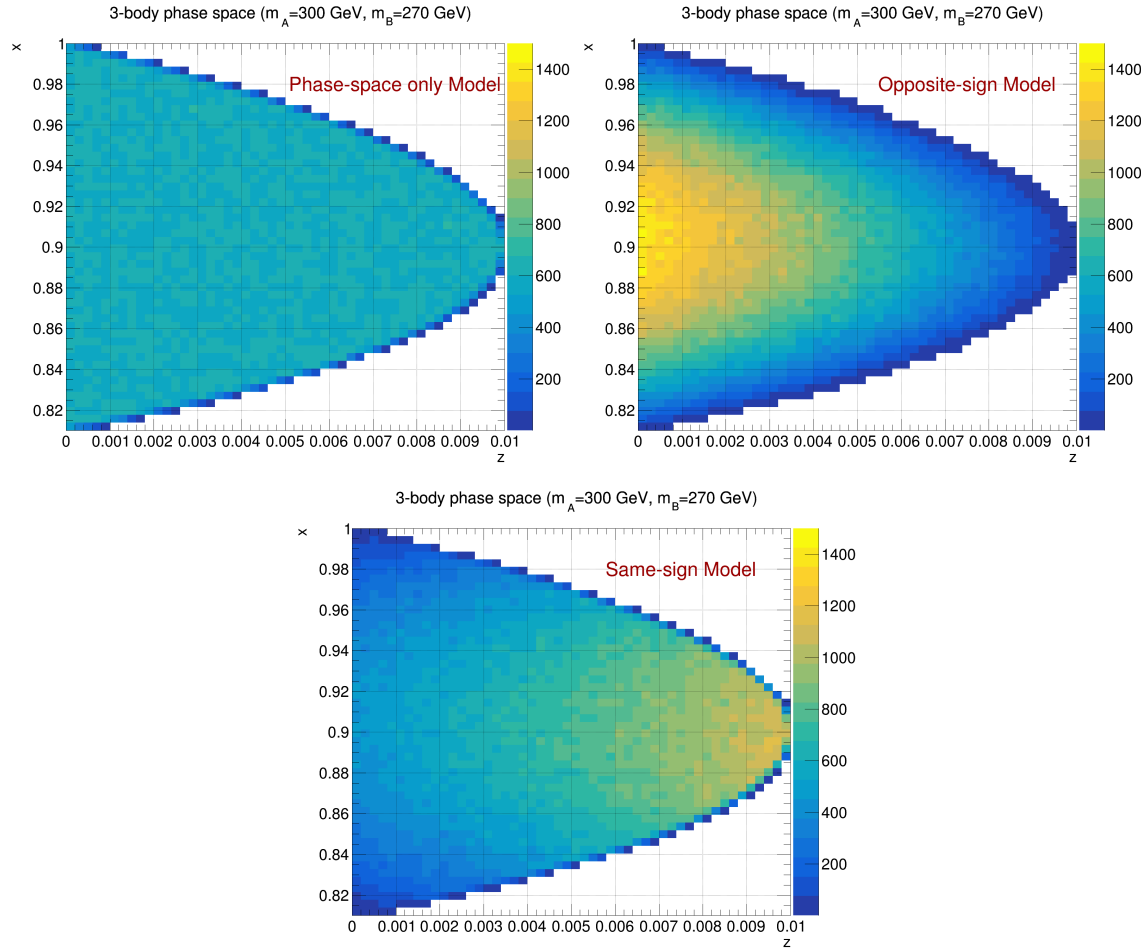


Figure 8.6: Dalitz distributions of the phase space parameters x and z . The heatmap compares the uniform phase space simplified model against the model dependent scenarios OS and SS which distribute the four momenta of the decay components differently.

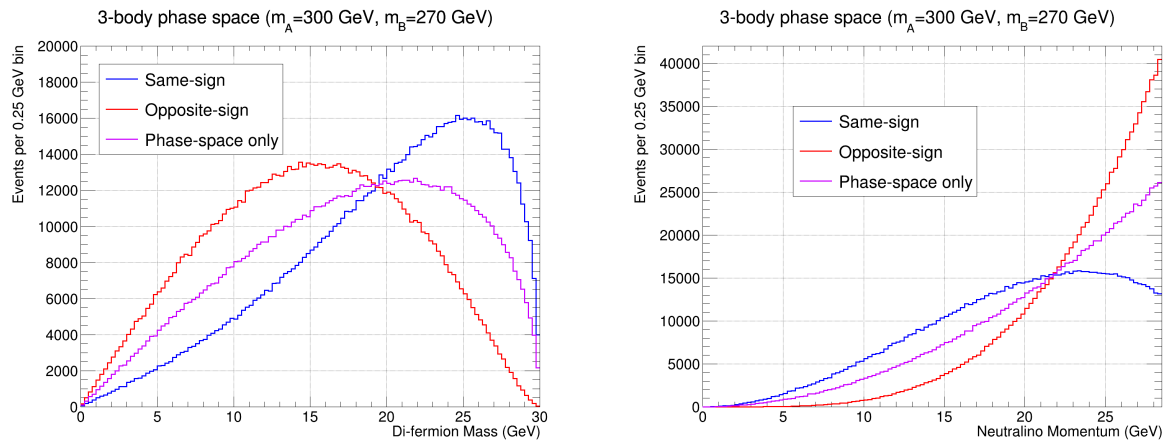


Figure 8.7: The reweighted di-fermion invariant masses (left) and an illustration of the momentum partitioning for each reweighting scenario (right)

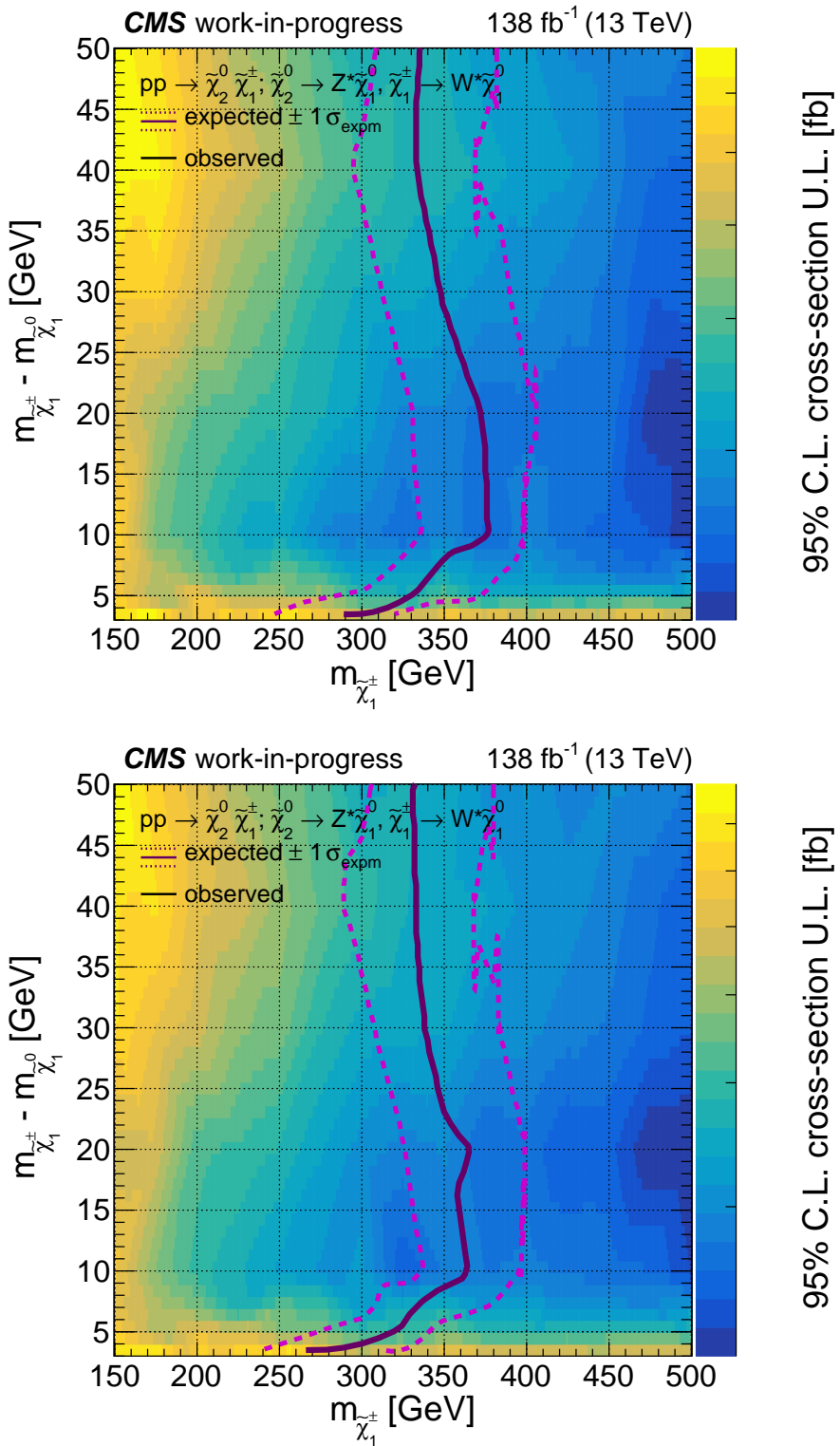


Figure 8.8: The expected cross section upper limits for 2016 MC scaled to 138 fb^{-1} . Compares the OS reweighting (top) and SS reweighting (bottom).

Chapter 9

Summary

This dissertation outlines a general search for supersymmetric particles in compressed scenarios. The search is performed with proton-proton collisions at $\sqrt{s} = 13$ TeV and the CMS detector using the full Run II data-set with integrated luminosity of 138 fb^{-1} . A general compressed SUSY topology is identified as ISR recoiling against an energetic invisible and soft visible system. This topology is organized into a set of decay trees by labeling topological components as either part of the ISR or Sparticle systems. The sparticle system is further subdivided into a di-sparticle system with visible and invisible components partitioned into each. The decay tree reference frames are approximated using a rule set from the Recursive Jigsaw Reconstruction framework that guides the optimal partitioning for each reference frame. Following the construction of each event's decay tree, kinematic mass sensitive variables are derived to discriminate against backgrounds. Each event is then further categorized in bins of the mass sensitive kinematic variables R_{ISR} and M_\perp as well as physics object counts such as lepton multiplicity, jet multiplicity, b-tagging, and other complementary variables. The organization of all categories and the optimization of those categories has been shown to contain complementary regions that act as cross constraints for the fit. The lepton selection is also defined and the efficiencies of that selection are modeled with the Tag-and-Probe method. The Tag-and-Probe measurements are used to model and correct systematic effects through scale factors for each component of the gold, silver, and bronze lepton selections in each year separately. The Tag-and-Probe scale factors and systematics are a minor contribution to the overall fit which is composed of over 200 nuisance param-

eters. The nuisance parameters are derived by studying control region fits and statistical metrics such as the Poisson likelihood, z-score, or chi-squared. The set of nuisances is found to be satisfactory in describing both the control region fit and the validation region fit and does not reject a signal hypothesis in a signal injected fit. From the establishment of this fit, expected limits are shown for processes involving the production of stops, electroweakinos, and sleptons which extend the current exclusion reach significantly.

References

- [1] Chris Rogan, Riccardo Salvatico, Caleb Smith, Graham Wilson Andres Abreu, Justin Anguiano, Phil Baringer, Alice Bean, Zach Flowers, Jack King, Lawrence Lee, Margaret Lazarovits, Scarlet Norberg. General Search for Supersymmetric Particles with Compressed Mass Spectra in proton-proton Collisions at $\sqrt{s} = 13$ TeV. 2023. CMS cadiline SUS-23-003.
- [2] Wikipedia. Particle physics, 2021. Image retrieved April 2, 2023 from https://en.wikipedia.org/wiki/Particle_physics.
- [3] Georges Aad et al. Summary of the ATLAS experiment’s sensitivity to supersymmetry after LHC Run 1 — interpreted in the phenomenological MSSM. *JHEP*, 10:134, 2015.
- [4] Georges Aad et al. Searches for electroweak production of supersymmetric particles with compressed mass spectra in $\sqrt{s} = 13$ TeV pp collisions with the ATLAS detector. *Phys. Rev. D*, 101(5):052005, 2020.
- [5] P. A. Zyla et al. Review of Particle Physics. *PTEP*, 2020(8):083C01, 2020.
- [6] Sven Heinemeyer. The new muon g-2 result and supersymmetry. IDT-WG3-Phys Mini-Symposium on Muon g-2, 2021.
- [7] T. Aaltonen et al. High-precision measurement of the W boson mass with the CDF II detector. *Science*, 376(6589):170–176, 2022.
- [8] Emanuele Bagnaschi, Manimala Chakraborti, Sven Heinemeyer, Ipsita Saha, and Georg Weiglein. Interdependence of the new “MUON G-2” result and the W-boson mass. *Eur. Phys. J. C*, 82(5):474, 2022.

- [9] Cms collaboration, susy summary plots run 2. https://twiki.cern.ch/twiki/bin/view/CMSPublic/PhysicsResultsSUS#Run_2_Summary_plots_13_TeV. Last updated 2022-03-21.
- [10] Atlas collaboration, susy summary plots june 2021. <https://atlas.web.cern.ch/Atlas/GROUPS/PHYSICS/PUBNOTES/ATLPHYS-PUB-2021-019>. Last updated 2021-06-06.
- [11] LHC Machine. *JINST*, 3:S08001, 2008.
- [12] S. Chatrchyan et al. The CMS Experiment at the CERN LHC. *JINST*, 3:S08004, 2008.
- [13] A. M. Sirunyan et al. Particle-flow reconstruction and global event description with the CMS detector. *JINST*, 12(10):P10003, 2017.
- [14] J. J. Thomson. Cathode rays. *Phil. Mag. Ser. 5*, 44:293–316, 1897.
- [15] E. Rutherford. The scattering of alpha and beta particles by matter and the structure of the atom. *Phil. Mag. Ser. 6*, 21:669–688, 1911.
- [16] E. Fermi. An attempt of a theory of beta radiation. 1. *Z. Phys.*, 88:161–177, 1934.
- [17] Frederick Reines and Clyde L. Cowan. The neutrino. *Nature*, 178:446–449, 1956.
- [18] Murray Gell-Mann. A Schematic Model of Baryons and Mesons. *Phys. Lett.*, 8:214–215, 1964.
- [19] Sheldon L. Glashow. Partial-symmetries of weak interactions. *Nuclear Physics*, 22(4):579–588, 1961.
- [20] Abdus Salam. Weak and Electromagnetic Interactions. *Conf. Proc. C*, 680519:367–377, 1968.
- [21] Steven Weinberg. A Model of Leptons. *Phys. Rev. Lett.*, 19:1264–1266, 1967.

- [22] G. Arnison et al. Experimental observation of lepton pairs of invariant mass around 95 gev/c^2 at the cern sps collider. *Physics Letters B*, 122(1-2):103–116, 1983.
- [23] Sheldon L. Glashow. The future of elementary particle physics. *Reviews of Modern Physics*, 56(3):161–174, 1984.
- [24] Serguei Chatrchyan et al. Observation of a New Boson at a Mass of 125 GeV with the CMS Experiment at the LHC. *Phys. Lett. B*, 716:30–61, 2012.
- [25] Georges Aad et al. Observation of a new particle in the search for the Standard Model Higgs boson with the ATLAS detector at the LHC. *Phys. Lett. B*, 716:1–29, 2012.
- [26] Mark Thomson. *Modern particle physics*. Cambridge University Press, New York, 2013.
- [27] Michael E. Peskin and Daniel V. Schroeder. *An Introduction to quantum field theory*. Addison-Wesley, Reading, USA, 1995.
- [28] Peter W. Higgs. Spontaneous Symmetry Breakdown without Massless Bosons. *Phys. Rev.*, 145:1156–1163, 1966.
- [29] G. Bernardi, M. Carena, and T. Junk. Higgs Bosons, theory and searches. 2008.
- [30] Howard Baer and Xerxes Tata. *Weak Scale Supersymmetry : From Superfields to Scattering Events*. Oxford University Press, 2007.
- [31] A DJOUADI. The anatomy of electroweak symmetry breaking tome II: The higgs bosons in the minimal supersymmetric model. *Physics Reports*, 459(1-6):1–241, apr 2008.
- [32] Wolfgang Adam and Iacopo Vivarelli. Status of searches for electroweak-scale supersymmetry after LHC Run 2. *Int. J. Mod. Phys. A*, 37(02):2130022, 2022.

- [33] Glennys R. Farrar and Pierre Fayet. Phenomenology of the Production, Decay, and Detection of New Hadronic States Associated with Supersymmetry. *Phys. Lett. B*, 76:575–579, 1978.
- [34] A. Djouadi et al. The Minimal supersymmetric standard model: Group summary report. In *GDR (Groupement De Recherche) - Supersymetrie*, 12 1998.
- [35] Benjamin Fuks, Michael Klasen, Saskia Schmiemann, and Marthijn Sunder. Realistic simplified gaugino-higgsino models in the MSSM. *The European Physical Journal C*, 78(3), mar 2018.
- [36] Katherine Garrett and Gintaras Duda. Dark Matter: A Primer. *Adv. Astron.*, 2011:968283, 2011.
- [37] F. Zwicky. Die Rotverschiebung von extragalaktischen Nebeln. *Helv. Phys. Acta*, 6:110–127, 1933.
- [38] Richard Massey, Jason Rhodes, Richard Ellis, N. Scoville, Alexie Leauthaud, A. Finoguenov, Peter Capak, David Bacon, Herve Aussel, Jean-Paul Kneib, Anton Koekemoer, Henry McCracken, Bahram Mobasher, S. Pires, Alexandre Refregier, Shunji Sasaki, Jean-Luc Starck, Yoshi Taniguchi, Andy Taylor, and James Taylor. Dark matter maps reveal cosmic scaffolding. *Nature*, 445:286–90, 02 2007.
- [39] Volker Springel, SDM White, Adrian Jenkins, Carlos Frenk, Naoki Yoshida, Liang Gao, Julio Navarro, R. Thacker, Darren Croton, John Helly, Joe Peacock, Shaun Cole, Peter Thomas, H. Couchman, August Evrard, Joerg Colberg, and Frazer Pearce. Simulations of the formation, evolution and clustering of galaxies and quasars. *Nature*, 435, 06 2005.
- [40] N. Aghanim et al. Planck 2018 results. VI. Cosmological parameters. *Astron. Astrophys.*, 641:A6, 2020. [Erratum: *Astron. Astrophys.* 652, C4 (2021)].

- [41] B. Abi et al. Measurement of the Positive Muon Anomalous Magnetic Moment to 0.46 ppm. *Phys. Rev. Lett.*, 126(14):141801, 2021.
- [42] Riccardo Barbieri and G. F. Giudice. Upper Bounds on Supersymmetric Particle Masses. *Nucl. Phys. B*, 306:63–76, 1988.
- [43] M. Awramik, M. Czakon, A. Freitas, and G. Weiglein. Precise prediction for the W boson mass in the standard model. *Phys. Rev. D*, 69:053006, 2004.
- [44] Armen Tumasyan et al. The Phase-2 Upgrade of the CMS Tracker. 6 2017.
- [45] Albert M Sirunyan et al. Precision luminosity measurement in proton-proton collisions at $\sqrt{s} = 13$ TeV in 2015 and 2016 at CMS. *Eur. Phys. J. C*, 81(9):800, 2021.
- [46] CMS luminosity measurement for the 2017 data-taking period at $\sqrt{s} = 13$ TeV. 2018.
- [47] CMS luminosity measurement for the 2018 data-taking period at $\sqrt{s} = 13$ TeV. 2019.
- [48] Johan Alwall, Michel Herquet, Fabio Maltoni, Olivier Mattelaer, and Tim Stelzer. MadGraph 5 : Going Beyond. *JHEP*, 06:128, 2011.
- [49] Simone Alioli, Paolo Nason, Carlo Oleari, and Emanuele Re. A general framework for implementing NLO calculations in shower Monte Carlo programs: the POWHEG BOX. *JHEP*, 06:043, 2010.
- [50] Torbjörn Sjöstrand, Stefan Ask, Jesper R. Christiansen, Richard Corke, Nishita Desai, Philip Ilten, Stephen Mrenna, Stefan Prestel, Christine O. Rasmussen, and Peter Z. Skands. An introduction to PYTHIA 8.2. *Comput. Phys. Commun.*, 191:159–177, 2015.
- [51] Vardan Khachatryan et al. Event generator tunes obtained from underlying event and multiparton scattering measurements. *Eur. Phys. J. C*, 76(3):155, 2016.

- [52] Albert M Sirunyan et al. Extraction and validation of a new set of CMS PYTHIA8 tunes from underlying-event measurements. *Eur. Phys. J. C*, 80(1):4, 2020.
- [53] S. Agostinelli et al. GEANT4—a simulation toolkit. *Nucl. Instrum. Meth. A*, 506:250–303, 2003.
- [54] Paul Jackson and Christopher Rogan. Recursive jigsaw reconstruction: Hep event analysis in the presence of kinematic and combinatoric ambiguities. *Phys. Rev. D*, 96:112007, Dec 2017.
- [55] Matteo Cacciari, Gavin P. Salam, and Gregory Soyez. The anti- k_t jet clustering algorithm. *JHEP*, 04:063, 2008.
- [56] Jet Performance in pp Collisions at 7 TeV. 2010.
- [57] Markus Stoye. Deep learning in jet reconstruction at CMS. *J. Phys. Conf. Ser.*, 1085(4):042029, 2018.
- [58] Vardan Khachatryan et al. Measurement of $B\bar{B}$ Angular Correlations based on Secondary Vertex Reconstruction at $\sqrt{s} = 7$ TeV. *JHEP*, 03:136, 2011.
- [59] Erich Schmitz. *Search for Production of Supersymmetric Top Quarks in Hadronic and Multi-Leptonic Final States, Using a Deep Neural Network Based Soft B-Tagger for Compressed Mass Scenarios*. PhD thesis, 2021. Copyright - Database copyright ProQuest LLC; ProQuest does not claim copyright in the individual underlying works; Last updated - 2023-03-08.
- [60] Robert D. Cousins, James T. Linnemann, and Jordan Tucker. Evaluation of three methods for calculating statistical significance when incorporating a systematic uncertainty into a test of the background-only hypothesis for a poisson process. *Nuclear Instruments and Methods in Physics Research Section A: Accelerators, Spectrometers, Detectors and Associated Equipment*, 595(2):480–501, oct 2008.

- [61] Glen Cowan, Kyle Cranmer, Eilam Gross, and Ofer Vitells. Asymptotic formulae for likelihood-based tests of new physics. *Eur. Phys. J. C*, 71:1554, 2011. [Erratum: Eur.Phys.J.C 73, 2501 (2013)].
- [62] Cuts/equations for mva. https://twiki.cern.ch/twiki/pub/CMS/SUSLeptonSF/Run2_SUSYwp_EleCB_MVA_8Jan19.pdf. Created 2019-01-19.
- [63] Proposal of a new “medium” muon id. <https://indico.cern.ch/event/357213/contributions/1769745/attachments/710701/975626/muonid-pog081214.pdf>. Presented 2014-08-12.
- [64] Electron identification based on simple cuts. <https://twiki.cern.ch/twiki/bin/view/CMSPublic/EgammaPublicData>. Late updated 2016-04-22.
- [65] Baseline muon selections for run 2. https://twiki.cern.ch/twiki/bin/view/CMS/SWGuideMuonIdRun2#Particle_Flow_isolation. Late updated 2022-01-19.
- [66] Alternatives to standard isolation for 13 tev. https://indico.cern.ch/event/368826/contributions/871862/attachments/733500/1006397/20150127_ald_susy_iso.pdf. Presented 2015-01-27.
- [67] V. Halyo A. Hunt K. Mishra N. Adam, J. Berryhill. Generic tag and probe tool for measuring efficiency at cms with early data. June 2009.
- [68] Jeffrey Berryhill, Georgios Daskalakis, Valerie Halyo, Jeremy Werner, and Si Xie. Electron efficiency measurements with 2.88 pb^{-1} of pp collision data at $\sqrt{s} = 7 \text{ tev}$. Nov 2010.
- [69] Giovanni Petrucciani, Andrea Rizzi, and Carl Vuosalo. Mini-AOD: A New Analysis Data Format for CMS. *J. Phys. Conf. Ser.*, 664(7):7, 2015.
- [70] Electron tag-and-probe producer git repository. <https://github.com/cms-egamma/EgammaAnalysis-TnPTreeProducer>. Last updated 2022-06-27.

- [71] Electron tag-and-probe analyzer git repository. https://github.com/cms-egamma/egm_tnp_analysis. Last updated 2022-09-01.
- [72] Muon tag-and-probe producer. <https://twiki.cern.ch/twiki/bin/viewauth/CMS/MuonTagAndProbe>. Last updated 2012-02-11.
- [73] Tag-and-probe analyzer. <https://twiki.cern.ch/twiki/bin/view/CMSPublic/SWGuideTagProbeFitTreeAnalyzer>. Last updated 2010-06-03.
- [74] Muon tag-and-probe instructions for run 2. <https://twiki.cern.ch/twiki/bin/viewauth/CMS/MuonTagAndProbeTreesRun2>. Last updated 2020-05-18.
- [75] J. P. Lansberg. J/ψ , ψ' and Υ production at hadron colliders: A Review. *Int. J. Mod. Phys. A*, 21:3857–3916, 2006.
- [76] R Aaij et al. Production of J/ψ and Upsilon mesons in pp collisions at $\sqrt{s} = 8$ TeV. *JHEP*, 06:064, 2013.
- [77] F. Abe et al. A Measurement of the ratio $\sigma \times B(p\bar{p} \rightarrow W \rightarrow e\nu) / \sigma \times B(p\bar{p} \rightarrow Z^0 \rightarrow ee)$ in $p\bar{p}$ collisions at $\sqrt{s} = 1800$ GeV. *Phys. Rev. D*, 52:2624–2655, 1995.
- [78] I. Antcheva et al. ROOT: A C++ framework for petabyte data storage, statistical analysis and visualization. *Comput. Phys. Commun.*, 180:2499–2512, 2009.
- [79] Lorenzo Moneta, Kevin Belasco, Kyle Cranmer, Sven Kreiss, Alfio Lazzaro, Danilo Piparo, Gregory Schott, Wouter Verkerke, and Matthias Wolf. The roostats project, 2011.
- [80] J. S. Conway. Incorporating Nuisance Parameters in Likelihoods for Multisource Spectra. In *PHYSTAT 2011*, pages 115–120, 2011.
- [81] Margaret Lazarovits. *A General Search for Supersymmetry in Compressed Scenarios Featuring a Novel Fake Lepton Estimation Method*. PhD thesis, 2022. Copyright -

Database copyright ProQuest LLC; ProQuest does not claim copyright in the individual underlying works; Last updated - 2023-03-08.

- [82] Armen Tumasyan et al. Search for supersymmetry in final states with two or three soft leptons and missing transverse momentum in proton-proton collisions at $\sqrt{s} = 13$ TeV. *JHEP*, 04:091, 2022.
- [83] Mihoko M. Nojiri and Youichi Yamada. Neutralino decays at the CERN LHC. *Phys. Rev. D*, 60:015006, 1999.